May 2014

Numerical Simulation of Flow in Ozonation Process

Jie Zhang
University of South Florida, jiezhang.cfd@gmail.com

Numerical Simulation of Flow in Ozonation Process

by

Jie Zhang

A dissertation submitted in partial fulfillment
of the requirements for the degree of
Doctor of Philosophy
Department of Civil and Environmental Engineering
College of Engineering
University of South Florida

Co-Major Professor: Andrés E. Tejada-Martínez, Ph.D.
Co-Major Professor: Qiong Zhang, Ph.D.
James R. Mihelcic, Ph.D.
Muhammad M. Rahman, Ph.D.
Hongxia Lei, Ph.D.

Date of Approval:
January 17, 2014

Keywords: Water treatment, ozone disinfection, reaction kinetics, turbulent flow, computational fluid dynamics

DEDICATION

This dissertation is dedicated to my family and friends. I would like to express a special feeling of gratitude to my loving wife, Kai Liao. Thank you for the support, the fun, and the love you have given in this process. I would like to express my most sincere gratitude to my parents, Lirui Zhang and Lijuan Long, for their unconditional encouragement, inspiration and support. It is their encouragement and support from the very beginning of my life that made it possible for me to reach this stage.

I would like to offer special thanks to my friends, Wenge Wei and Qiong Zhang, for their help and concern in daily life. I am also grateful to Jun Cheng, Bingxiong Lin, Junyi Tu, Weiwei Mo, and Simona Platukyte who have been my close friends throughout my doctorate program.

Finally, I would like to thank these who have helped me, especially in the first few months when I came to United States.

ACKNOWLEDGMENTS

First and foremost I want to thank my advisors Dr. Andrés E. Tejada-Martínez and Dr. Qiong Zhang. It has been my honor to be their student for years. Dr. Andrés E. Tejada-Martínez is a kind and friendly man. He was always patient to me. Throughout my doctorate program, he provided encouragement, sound advice, good teaching, and lots of good ideas. Dr. Qiong Zhang's creativity, inquisitive nature and incredible passion to her work are all qualities to which I aspire. I greatly appreciate her strong support and guidance in research. I also thank her for teaching me not only knowledge but also the skills in producing and presenting a quality work. In every sense, none of this work would have been possible without them.

I would also like to express my special and great thanks to Dr. Hongxia Lei for her valuable advice and help in collecting measured data in the ozone contactor operated by City of Tampa Water Department. My sincere thanks are extended to the other members of my advisory committee: Dr. James R. Mihelcic and Dr. Muhammad M. Rahman for their time, interest, helpful comments and insightful questions during this research.

My great thanks also go to all of the Graduate students in Computational Environmental Fluid Dynamics group and Dr. Qiong Zhang's research group for their help, the laughs, and the memories.

I gratefully acknowledge financial support through research funds provided by Dr. Tejada-Martinez in addition to teaching assistantships provided by the Civil and Environmental Engineering Department and a research fellowship provided by the College of Engineering.

TABLE OF CONTENTS

LIST OF TABLES

LIST OF FIGURES

ABSTRACT

In the last two decades, Computational Fluid Dynamics (CFD) has shown great potential as a powerful and cost-efficient tool to troubleshoot existing disinfection contactors and improve future designs for the water and wastewater treatment utilities.

In the first part of this dissertation two CFD simulation methodologies or strategies for computing turbulent flow are evaluated in terms of the predicted hydraulic performance of contactors. In the LES (large eddy simulation) methodology, the more energetic, larger scales of the turbulence are explicitly computed or resolved by the grid. In the less computationally intensive RANS (Reynolds-averaged Navier-Stokes) methodology, only the mean component of the flow is resolved and the effect of the unresolved turbulent scales is accounted for through a turbulence model. For baffled contactors, RANS performs on par with the LES in predicting hydraulic performance indices. In this type of contactors, hydraulic performance is primarily determined by quasi-steady recirculating (dead) zones within the contactor chambers which are well-resolved in both RANS and LES. Testing of the RANS methodology is also performed for a wastewater stabilization pond leading to prediction of hydraulic performance indices in good agreement with field measurements. However, for column contactors, LES performs better than RANS due to the ability of the LES to resolve unsteady or unstable flow structure associated with spatial transition to turbulence which is important in the determination of the hydraulic performance of the contactor.

In the second part of this dissertation the RANS methodology is adapted in order to develop a novel modeling framework for ozone disinfection of drinking water. This framework is unique as it combines CFD with kinetics-based reaction modeling to predict disinfection performance and bromate formation for the first time. Bromate, a human health hazard, is an undesired by-product of the disinfection of drinking water via ozonation. The modeling framework is validated via application to a full-scale ozone contactor. Predictions of ozone and bromate concentrations are consistent with data from physical experiments.

CHAPTER 1: INTRODUCTION

1.1 Background and Motivations

Disinfection process is an essential technology for human health, providing a degree of protection for potable water and wastewater from contact with pathogens by inactivating them. The primary methods used for the disinfection of water and wastewater are chlorine, ozone, and ultraviolet irradiation (UV). The use of ozone is becoming increasingly common in disinfection process for water and wastewater treatment, in part because of its stronger disinfecting properties and in part because it controls taste and odor compounds (Crittenden et al. 2005). Globally, more than 3,000 ozone contactors are being used for water disinfection (Wols et al. 2010a). A common approach to ozone disinfection is to pass the water through an ozone contactor tank consisting of a series of chambers as depicted in Figure 1.1. Ozone gas is released into the chambers from the bottom of one or multiple chambers via bubble diffusers pictured in Figure 1.1. Upon release the ozone dissolves in the water and begins the disinfection process.

A primary task for ozone contactor designers is to increase the disinfection efficiency thereby reducing the operating cost of the ozone contactor. Information for designing an ozone contactor is usually obtained from experimental data. However, due to equipment limits and high expense of physical experiments, an accurate computational or mathematical model may be the better solution. Early research towards this end focused on developing ideal hydraulic models for reactors, i.e. Completely Mixed Flow Reactor (CMFR) or Plug Flow reactor (PFR) (Froment and Bischoff 1979). However, ideal models simplify the ozonation process in reactors assuming ideal

hydraulic and mixing conditions. An overly simplistic model may result in an over-dosage of ozone leading to an increase in undesired disinfection by-products such as bromate requiring additional treatment. Such negative outcomes also increase design capital costs and continuous operation costs.

The next generation of models included non-ideal models developed through the combination of ideal models. For example, the Tank in Series (TIS) model was developed by assuming a reactor consists of a series of CMFRs. However, all non-ideal models rely on tracer studies to understand the flow behavior. Such tracer studies require physical experiments.

Computational fluid dynamics (CFD), which had been successfully applied to aerospace engineering, automotive engineering, architecture designs and other industrial engineering applications for years, has been proven recently to be a successful alternative for modeling the ozone disinfection process. The first applications of CFD to the ozonation process were made in the 1990s (Cockx et al. 1999; Huang et al. 2002). The cost of CFD is much cheaper than that of a physical experiment and keeps consistently dropping due to rapid development in computer technology. Furthermore, CFD allows for more detailed flow analysis of full-scale ozone contactors before its construction. CFD has also been shown to be a useful tool for comparing the performances of different design options. CFD is able to provide a more accurate representation/description of the ozonation process because it solves mass, momentum and energy equations directly without requiring assumptions made by the earlier models. Several studies have reported on the applicability and reliability of CFD for ozonation process simulation (Zhang 2006; Bolaños et al. 2008). Continued advances in computational power have enabled highly resolved CFD analysis of the hydrodynamics in ozone reactors leading to a detailed description of the flow behavior. For example, CFD solutions are able to identify localized flow

phenomena such as short-circuiting and dead zones, shown in Figure 1.2, which reduce hinder disinfection efficiency.

However, the question of how to apply CFD properly to simulation of ozone disinfection process is still under exploration. Generally, the simulation of ozone disinfection process is divided into two components, hydraulics modeling and reaction process modeling. Most of the previous studies have focused on hydraulics modeling (Henry and Freeman 1995; Murrer et al. 1995; Peltier et al. 2001; and Huang et al. 2002). Several problems and issues discovered in these studies motivate further research. For example, the difference in residence time distributions may be small even when the flow fields are totally different. This indicates that differences in prescribed inflow conditions may have a small effect on an integrated property like the residence time distribution (Wols et al. 2010a). A second issue is related to the fact that flow simulations often require an estimate of the turbulence intensity at the inflow boundary and predictions of tracer residence time distribution (RTD) density can be strongly dependent on this prescribed inlet turbulence intensity. As shown by Huang et al. (2004), an extremely high (unphysical) inlet turbulence intensity was needed to obtain good agreement with RTD physical experimental data. More research is needed to understand the dependence of simulation results on inlet turbulence intensity. The current dissertation addresses other important issues associated with hydraulic modeling. These will be described in section 1.2.

Attempts have been made at modeling ozonation processes under simplifications, such as steady flow assumption. However, there are still more developments needed for CFD models to reach the point of fully simulating the complicated interrelationships between physical, chemical and biological process in the disinfection process. For example, it is still unclear how turbulence affects the effective rates of chemical reactions. Several factors may be involved, such as (1)

whether reactants are premixed or non-premixed (2) the rate of chemical reactions relative to the rate of scalar mixing by the turbulence and (3) the turbulence length scales relative to the size of a reaction region. Adding to the modeling complexity is that chemical reactions may also affect turbulence by modifying the fluid properties locally (Ranade 2002).

1.2 Objectives and Organization of the Dissertation

The overarching objective of this dissertation is to develop and validate a modeling framework for the ozone disinfection process by combining CFD with kinetics-based reaction modeling for the first time for the prediction of disinfection performance and bromate formation. In order to achieve this goal, the sub-processes or components of ozone disinfection, such as flow, tracer transport, reactions, and inactivation, need to be investigated. Along the way several applications of the framework to water and wastewater treatment processes will be presented.

The rest of this dissertation is organized as follows:

- Chapter 2 presents a literature review on developments in CFD-based modeling for disinfection technologies over the last two decades. How the developments proposed/implemented in this dissertation fit within prior developments made by others is discussed.
- Chapter 3 presents the modeling framework developed in this dissertation, in particular the computational approaches taken for each of the ozone disinfection sub-processes mentioned above. This framework is unique as it combines CFD with kinetics-based reaction modeling for the first time for bromate prediction.
- In Chapter 4 turbulent flow computational approaches, Reynolds-averaged Navier-Stokes Simulation and Large Eddy Simulation, are evaluated in terms of prediction of hydraulic performance of contactors.

- In Chapter 5 the modeling framework developed in Chapter 3 is validated via application to a full-scale ozone contactor. The predictions in terms of ozone and bromate concentrations are consistent with physical measurements.
- Chapter 6 presents extended applications of the modeling framework developed in this dissertation, such as an investigation of the hydraulic efficiency and its impact on energy consumption of ozone contactors, and a study of the hydraulics of a water stabilization pond.
- Finally, Chapter 7 presents the conclusions reached by the current research together with recommendations for future work.

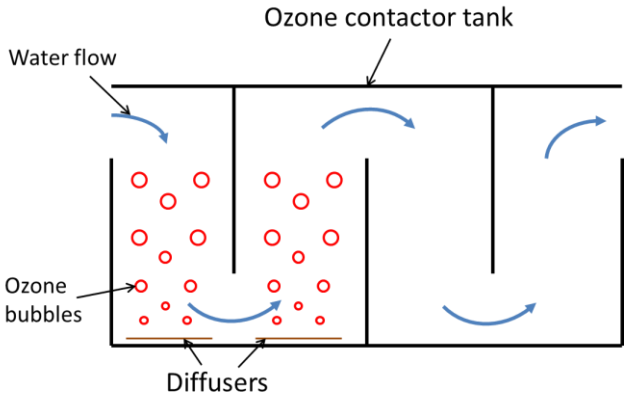

Figure 1.1: Illustration of ozone disinfection in a typical ozone contactor tank.

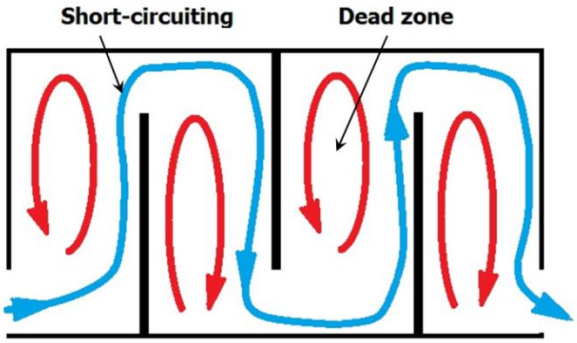

Figure 1.2: Short-circuiting and dead zones in a typical ozone contactor.

CHAPTER 2: DEVELOPMENTS IN COMPUTATIONAL FLUID DYNAMICS-BASED MODELING FOR DISINFECTION

2.1 Introduction

The disinfection process is a critical safety step in drinking water treatment that inactivates bacteria, viruses, and other pathogens. The most common disinfection approaches for water treatment include chlorine disinfection (including chlorination, chlorine dioxide, and chloramines), ozone disinfection, and ultraviolet (UV) light disinfection. The history of chlorine disinfection can be traced back to the late 1800s (U.S. EPA 1986) and is still one of the most widely used technologies in the U.S. (Solomon et al. 1998). Ozone disinfection is becoming increasingly important because of its effective disinfection and odor control (Crittenden et al. 2005). Both chlorine disinfection and ozone disinfection inactivate pathogens primarily by oxidation. In UV disinfection, UV radiation penetrates the genetic material of pathogens and retards their ability to reproduce. Thus, it is a physical process rather than a chemical process, eliminating chemical residual issues associated with other disinfection approaches.

The goal of optimizing contactor configuration to improve disinfection efficiency has driven engineers towards disinfection modeling in addition to physical experiments. The early models for disinfection, such as plug flow reactor (PFR) and completely mixed flow reactor (CMFR) were developed based on ideal flow conditions. Further details on the early models can be found in introductory textbooks on chemical reaction engineering (e.g., Hill 1977; Levenspiel 1998; Fogler 1999). Successes have been reported on modeling ozone disinfection in column

contactors using the axial dispersion reactor (ADR) model combined with reaction and inactivation kinetics (Kim et al. 2002, 2007; Chen 1998). However, due to the lack of consideration of the effects of turbulence and complex flow conditions, such as dead zones and short-circuiting, it is impossible to apply this kind of model to a contactor with complex geometry.

With rapid advances in computing technology, CFD has been used by rising numbers of water and wastewater treatment researchers for troubleshooting or optimizing reactor design and operation. Early work has proven the applicability of CFD to disinfection processes (Do-Quang et al. 1997; Janex et al. 1998). It has been applied in not only evaluating the hydraulic efficiency (excluding reaction and inactivation) of existing reactors (including contactors for disinfection), but also in optimizing future reactor designs (Kim et al. 2010a; Amini et al. 2011; Wols et al. 2008b; Evans 2003; Melissa 2010; Cockx et al. 1999; Stamou 2008). However, it is still a great challenge to conduct a complete CFD simulation of disinfection processes involving flow, reaction, and inactivation.

The primary goal of this chapter is to identify the challenges in disinfection process simulation. In this chapter, the steps of a complete disinfection process simulation are first introduced. Then, the state of current research is reviewed by categorizing it into three groups: development of simulation method or framework for disinfection process, the impact of operation, configuration, and modeling parameters on disinfection efficiency, and optimization of the configuration of contactors. Then, the challenges in a CFD simulation of flow, tracer transport, reaction and inactivation are examined. Potential solutions to overcome these challenges are discussed.

2.2 Stages of CFD Applied to Disinfection Process

CFD technology has been used to model the flow in water treatment since the late 1990s (Do-Quang et al. 1997; Janex et al. 1998), including water intake infrastructures, flocculation tanks, sedimentation basins, and disinfection reactors (Craig et al. 2002). The early success of CFD in water treatment flow simulation led to an increased interest in applying CFD to disinfection processes as shown by the increase in related publications in Figure 2.1.

The increasing interest in CFD applied to disinfection process is partly due to the rapid advancement of computer technology making intensive computing affordable; and partly due to the demand for modeling of the disinfection process. The primary goals in the modeling of disinfection processes are to increase disinfection efficiency and reduce cost, or to optimize reactor design to comply with regulations or both.

Modeling of disinfection process can be divided into four stages: flow simulation, tracer transport simulation, reaction process simulation, and inactivation simulation. The latter three stages are heavily dependent on the first one, flow simulation. Thus, the accuracy of flow simulation is the most important one among the four. Note that, inactivation simulation also needs important input from the reaction process simulation.

2.2.1 Flow Simulation

The most basic governing equations of incompressible fluid flow are the continuity equation and momentum equations (or Navier-Stokes equations). The continuity equation is

$$\frac{\partial u_i}{\partial x_i} = 0 \tag{2.1}$$

where u_i and x_i are velocity and position in i-th direction.

The momentum equations are derived from Newton's second law. A general form of the momentum equations is

$$\frac{\partial u_i}{\partial t} + u_j \frac{\partial u_i}{\partial x_j} = -\frac{1}{\rho}\frac{\partial p}{\partial x_i} + \nu \frac{\partial^2 u_i}{\partial x_j \partial x_j} + f_i \tag{2.2}$$

where t is time, ρ is fluid density, p is pressure, ν is the kinematic viscosity, and f_i represents a body force (the force per unit of mass) in the i^{th} direction.

An important issue in flow simulation is how to treat the turbulence. Turbulent flows contain a large range of spatial scales, from the smallest turbulent eddies on the order of millimeters, to bulk flow features comparable with the size of the geometry. The range of motions in a turbulent flow grows with the Reynolds number (*Re*) generally defined as $Re = LU/\nu$ where U and L are a characteristic velocity and length scale of the flow.

Three primary strategies for the treatment of turbulence are well known (Pope 2000): Reynolds-Averaged Navier-Stokes equations (RANS) simulation, Large Eddy Simulation (LES), and Direct Numerical Simulation (DNS).

DNS resolves the governing Navier-Stokes equations numerically over the entire range of turbulent scales. However, the requirements on mesh resolution and time-step put high demands on computational resources, rendering it unsuitable for most engineering applications. More specifically, the grid for DNS should contain approximately $Re^{9/4}$ points. Typical Reynolds numbers are $O(1x10^6)$ giving rise to the need for large numbers of grid points that make DNS computationally prohibitive.

RANS is a statistical approach for the simulation of turbulent flow. RANS involves the application of Reynolds averaging to decompose Navier-Stokes equation solution variables into their means and the turbulent fluctuations around these means. The primary advantage of RANS is the relative low requirement on computer resource. Therefore, RANS has been successfully applied to simulation of high Reynolds number flows, such as flow simulation around a full-scale airplane. However, RANS has two main drawbacks: 1) it only resolves the mean flow and

all of the unresolved turbulent scales must be modeled through an added stress term to the momentum equation, thus rendering the turbulence model crucial for the accurate representation of the mean flow; 2) no universal RANS turbulence model exists, thus a specific model may be needed for the particular flow problem.

LES also aims to reduce the requirements on mesh resolution imposed by DNS. The idea of LES is to use a spatial filter to separate the turbulent flow field into two components. The larger scale, more energetic structures that can be resolved by the numerical method on a given mesh are referred to as the resolved scales. The smaller structures that cannot be captured by the mesh are called sub-grid scales. The influence of sub-grid scales on resolved scales must be modeled through an added stress term to the momentum equation. The principle of LES lies on the fact that the small (unresolved) scales of the turbulence are homogeneous and isotropic and therefore easier to model relative to the larger scales. Furthermore, these small (unresolved) scales are universal and thus the sub-grid scale (SGS) model can be applicable to different flow problems. Results of LES would be closer to those of DNS under mesh refinement as the size of scales that require modeling become smaller and less energetic. LES is in between DNS and RANS in terms of accuracy and computational cost. Due to the physics of turbulence in the vicinity of an impermeable no-slip wall boundary being considerably different from the other parts of flow, typical SGS models such as the Smagorinsky model (Smagorinsky 1963) are not suitable for representing near-wall sub-grid scales. A common solution is to refine the mesh near the wall to the resolution of DNS. Thus, LES still has a high computational cost that cannot be afforded for engineering applications. LES is sometimes performed in conjunction with a near-wall model in order to avoid DNS-like resolution of the near-wall region (Pope, 2000).

2.2.2 Tracer Transport Simulation

Non-reactive tracer transport is often incorporated into a flow simulation in order to investigate hydraulic efficiency of the water treatment system, for example, in terms of mean residence time and other quantities of interest derived from residence time distributions. The tracer is a conservative element, typically a dye or salt. In CFD simulation, the tracer is usually treated as a passive scalar which has no impact on hydraulic characteristics. The basic technique used to conduct a tracer study is to introduce the tracer at the reactor inlet and measure the response at the outlet in order to obtain residence time statistics.

Two main approaches for the simulation of tracer transport are based on Lagrangian particle motion modeling (particle tracking) and solving a transport equation for tracer concentration, respectively. Particle tracking modeling has been applied successfully (Stropky et al. 2007; Thyn et al. 1998; Wols et al. 2008a). However, the Lagrangian-based approach is less popular than solving a transport equation for tracer concentration because common CFD codes are based on an Eulerian system.

For simulation of the tracer transport in fluid flow, an advection-diffusion equation is used:

$$\frac{\partial C}{\partial t} + u_j \frac{\partial C}{\partial x_j} - \frac{\partial}{\partial x_j}\left(D \frac{\partial C}{\partial x_j}\right) = 0 \tag{2.3}$$

where u_i is the flow velocity, C is the tracer concentration, and D is the molecular diffusivity for the scalar.

To solve the above advection-diffusion equation needs the input of the flow velocity field. There are two strategies to input the velocity field, namely frozen flow and dynamical flow:

1. Frozen flow: Based on the assumptions of 1) steady mean flow and 2) that tracer transport does not affect the flow hydraulics, the mean flow is solved first. The

advection-diffusion equation for scalar concentration in eqn. (2.3) is then solved using the frozen velocity field.

2. Dynamical flow: This strategy consists of solving the flow equations and the advection-diffusion equation for tracer concentration simultaneously at each time step.

The first strategy fits within the RANS methodology described earlier and has been commonly used due to its relatively low computational cost (Kim et al. 2010a; Hofman et al. 2007a; Huang et al. 2004). Note that LES is only compatible with the second strategy of tracer transport simulation because LES resolves smaller scales of the flow which are inherently unsteady.

2.2.3 Reaction Process Simulation

The main goal of reaction process simulation is to predict disinfectant dose distribution, requiring solutions of a series of chemical reactions. For example, in ozone disinfection, commonly considered chemical reactions include: reaction between ozone and natural organic matter (NOM) or total organic carbon (TOC); self-decomposition of dissolved ozone; and formation of by-products, such as bromate (Crittenden et al. 2005). Similar reactions and by-products occur in chlorine disinfection.

To model the transport of chemical species in a fluid flow, a general advection-diffusion equation similar to equation (2.3) is used:

$$\frac{\partial C_i}{\partial t} + u_j \frac{\partial C_i}{\partial x_j} - \frac{\partial}{\partial x_j}\left(D_i \frac{\partial C_i}{\partial x_j}\right) = S_i \tag{2.4}$$

where u_i is the flow velocity, C_i is the species concentration, D_i is the molecular diffusivity for the chemical species, and S_i is the external volumetric source term including generation, consumption and transfer to another phase. Typical species are listed in Table 2.1.

The external volumetric source term, S_i, on the right side of equation (2.4), makes the simulation of a reaction process much more complicated than tracer transport in equation (2.3). For example, the commonly used source terms existing in the ozone disinfection are listed in Table 2.1. In this table, k_d is the ozone decay constant, C_l is the concentration of dissolved ozone, k_{NOM} is the reaction rate constant for the reaction between dissolved ozone and NOM, $[NOM]$ is the concentration of NOM, and k_B is the bromate formation rate constant. For dissolved ozone, the source term usually consists of the rate of dissolved ozone decay and the consumption rates by bromate formation, NOM, and pathogens. In the equation for NOM, a second-order model is commonly used. Note that the popular source term in the equation for bromate listed in Table 2.1 is empirical and not kinetics-based due to the complexity of the bromate formation sub-processes. A kinetics-based source term for bromate will be introduced in Chapter 3 of this dissertation. Finally, note that the source term for the tracer is null. The reason why the simulation of reaction processes is challenging and possible solutions to overcome these challenges will be discussed in Section 2.4.

In UV disinfection, the disinfectant is not a chemical but rather the energy of UV incident radiation. Thus the primary goal of this stage of UV disinfection is to predict the incident radiation over space. Furthermore, the radiation modeling in UV disinfection is independent from the flow. More details about radiation modeling are described in section 2.3.1.

2.2.4 Inactivation Simulation

Additional reactions between microorganisms and disinfectant are included in the inactivation stage. Wols et al. (2010a) has summarized and compared the existing approaches to estimate micro-organisms survival ratio. An overview of inactivation or disinfection calculation methods is shown in Table 2.2. According to the study of Wols et al. (2010a), inactivation should

be modeled via a particle tracking method or an Eulerian approach (that solves the scalar transport equation for the number of microorganisms directly) and either method should incorporate flow characteristics such as dead zones and short-circuiting, in order to predict disinfection more accurately. However, particle tracking methods are relatively difficult to be implemented in traditional CFD codes because the latter are usually written in an Eulerian system. Thus, only Eulerian inactivation will be described in this review.

In Eulerian inactivation, a transport equation for the concentration of microorganism is commonly considered to be the governing equation of the inactivation of microorganisms (Greene et al. 2006; Huang et al. 2004; Wols et al. 2010a):

$$\frac{\partial N_m}{\partial t} + u_j \frac{\partial N_m}{\partial x_j} - \frac{\partial}{\partial x_j}\left(D_i \frac{\partial N_m}{\partial x_j}\right) = S_{N_m} \tag{2.5}$$

where N_m is the concentration of microorganism m and S_{N_m} is the external volumetric source term for microorganism m.

Various models have been developed for the source term of microorganisms. Details of these models are provided in section 2.3.1.

Using the frozen flow simulation strategy (i.e. RANS), solution of the inactivation equations based on RANS is typically performed after the first three components or stages outlined earlier (flow solution, passive tracer solution and reaction process solution) have been successfully computed. An overview of the four stages of disinfection process modeling by CFD is listed in Table 2.3. Note that in the RANS simulation strategy, computation of these stages is performed sequentially. In LES, all stages would be computed simultaneously. All components or stages comprising the outlined framework remain under active research. For example, up to date including this dissertation, LES has only been applied to stages 1 and 2. Challenges in application of LES to stages 3 and 4 will be described in upcoming sections. Overall,

improvement of this framework involving LES and RANS and related technologies, such as computer power and solution algorithms should improve the applicability and reliability of disinfection process simulations.

2.3 State of Current Research in Disinfection Simulation Using CFD

The primary interests of reported studies on modeling of disinfection process can be categorized into the following three groups:

- Development of simulation method or framework for disinfection process.
- The impacts of parameters (to be described below) on disinfection efficiency.
- Optimization of the configuration of contactors.

2.3.1 Development of Simulation Methods for Disinfection Process

Framework and simulation methodology development have always been at the frontier of disinfection simulation research. Before CFD technology was applied to the area of disinfection process, early research developed several simplified models for the flow in disinfection contactors, such as the axis dispersion reactor (ADR) model (Chen 1998; Kim et al. 2002; Kim et al. 2007) and the back flow cell model (BFCM) (Nguyen-Tien et al. 1985). However, these models cannot meet the demand of industry any longer due to limited applicability (usually the simplified models are only for contactors with simple geometries) and insufficient accuracy.

At the end of 1990s, researchers recognized the potential of CFD technology for improving disinfection modeling. Cockx et al. (1999) conducted simulations of the flow in two ozone disinfection towers using a two-phase flow CFD code. In their model (Cockx et al. 1999), a source term which represents mass transfer was introduced to achieve the dissolved gas concentration held in the reactor. Greene et al. (2002) developed a CFD-based framework to predict flow structure, mass transport and chlorine decay in a continuous flow pilot scale reactor.

This framework was verified by a test case comparison with physical experimental measurements. Greene et al. (2004) developed a CFD-based framework that incorporates experimentally derived terms for chlorine decomposition and microbial inactivation based on the work of Haas et al (1995). The results from this model (Greene et al. 2004) showed good agreement with the physical experimental data set over a wide range of microbial inactivation rates.

In order to reduce the high computational cost of CFD, researchers have developed a compartmental hybrid model of the completely mixed flow reactor (CMFR) and the plug flow reactor (PFR) (Gresch et al. 2009; Mandel et al. 2012) models. Although this kind of model is computationally-effective and easy to use, it has a relative low spatial resolution of the flow, which may cause serious accuracy problems. Additionally, compartmental models are unable to respond to varying flow conditions, thereby rendering them not practical for prediction. For example, a change in flow rate could potentially affect the size of dead zone regions or strength of short-circuiting. However, the compartmental model would not be able to detect this. Thus, the compartmental model is helpful for rapid analysis but not practical for prediction.

Bolaños et al. (2008) discussed the applicability of CFD to simulate ozonation processes in ozone disinfection. This research proposed the set of Navier-Stokes equations with effective density and effective viscosity applied to two-phase flows if the dispersed phase elements are small. Their simulation predicted ozone decay but did not represent bromate formation. Results from the study of Bolaños et al. (2008) demonstrated that CFD is an efficient tool to study mixing flow characteristics and inactivation processes in existing water treatment plants and for predicting process performance of new designs.

Besides simulations of flow in lab-scale contactors, attempts at applying CFD to full-scale contactors in water treatment plants have been conducted (Huang et al. 2004; Hofman et al. 2007a; Zhang et al. 2007; Talvy et al. 2011). Hofman et al. (2007a) applied CFD to the Leiduin water treatment plant, in the Netherlands. The disinfection performance of the ozone treatment at the plant was predicted and compared with experimental data. Talvy et al. (2011) used CFD to assess the ozone disinfection in the Tailfer plant in Brussels, Belgium. Zhang et al. (2007) developed a multiphase CFD framework to address all the major components of ozone disinfection processes at the Charles DesBaillets Water Treatment Plant in Montréal, Canada. The previously described simulations have predicted ozone decay but most of them have not predicted bromate formation. Zhang et al. (2007) used an empirical based model, rather than a kinetic-based model, to predict bromate formation. This will be described in more detail further below.

Kim et al. (2009) was the first to apply LES for analysis of flow in reactors as prior studies had been based on RANS. Kim et al. (2010a) concluded that the inability of RANS to capture turbulent flow structures in a baffled ozone contactor may lead to a poor prediction of tracer transport statistics such as t_{10} (i.e. the time it takes for 10 percent of the tracer injected at the inflow to reach the outflow). These statistics are often used for evaluating hydraulic efficiency. LES was proposed as a more accurate alternative to RANS due to its improved prediction of tracer transport statistics. The current dissertation work described in Chapter 4 revisited the numerical and experimental studies of Kim et al. (2010b) and found that the poor performance of RANS compared to LES observed by Kim et al. (2009) may have been due to inappropriate use of the turbulence model. It was found that for the near-wall resolving grid used by Kim et al. (2009), RANS with a low-Reynolds number turbulence model such as the Lauder-

Sharma *k-ε* model (Wilcox, 1994) leads to more accurate tracer transport statistics than RANS with the standard *k-ε* model (Wilcox, 1994). Application of the standard *k-ε* turbulence model on coarser grids led to better results. The reason for this is that the standard *k-ε* turbulence model is designed for coarse meshes that do not resolve viscous, near-wall dynamics. These results have been recently published in Zhang et al. (2013a).

Equations governing flow and tracer transport solutions (excluding the turbulence model) are general to disinfection simulation frameworks. Differences appear when modeling the reactions. For modeling chlorine disinfection, the commonly used reaction system consists of chlorine decay only (Greene 2002; Greene et al. 2006). For modeling ozone disinfection, the commonly considered reactions include ozone decomposition, reaction between ozone and instantaneous ozone demand (IOD) or natural organic matter (NOM) or total organic carbon (TOC), and bromate formation. A summary of the reaction systems used in CFD simulations of ozone disinfection is given in Table 2.4.

In the studies that considered bromate formation, an empirical model under the assumption that bromate concentration changes linearly with ozone exposure was used to represent the process (Zhang 2006; Bartrand 2006; Zhang et al. 2007). Although Zhang (2006) and Zhang et al. (2007) have a bromate formation module in their framework, these authors deemed not practical to predict bromate formation due to the sensitivity of the process of bromate formation to water quality. Bartrand (2006) showed prediction of bromate formation in the Alameda County Water District ozone contactor in Fremont, CA. However, the predictions were not compared with physical experimental data. Instead of empirical modeling, Mandel et al. (2012) used a quasi-mechanistic chemical model or kinetics-based model to represent the process of bromate formation. However, a systematic network was used by Mandel et al. (2012) to

represent the flow (rather than CFD), thereby reducing the accuracy of the flow solution and consequently reducing the fidelity of ozone and bromate concentration predictions.

This dissertation develops a novel CFD-based framework comprised of a kinetics-based model for ozonation process in ozone contactors. This modeling framework has been validated via application to a full-scale ozone contactor operated by the City of Tampa Water Department. Predictions of ozone and bromate concentrations from the model have shown good agreements with physical measured data. The contribution of this dissertation relative to previous studies is highlighted in Figure 2.2.

For modeling of UV disinfection, the primary focus in this stage is the radiation modeling. In turn, the radiation model appears as part of the source term in the advection-diffusion transport equations for inactivation of microorganisms. A summary of the radiation models used in the modeling of UV disinfection process up to date is listed in Table 2.5.

Although various inactivation models have been developed for the source terms of advection-diffusion equations governing the concentration of microorganisms (Gyurek and Finch 1998), only the Hom-Haas model and the Chick-Watson model have been put to practice in CFD codes. The Hom-Haas model can represent the inactivation kinetics more accurately than the Chick-Watson model (Haas and Karra 1984a, b; Zhang 2006). The source term expression given by the Hom-Haas model is

$$S_{N_m} = \frac{dN_m}{dt} = -xN_m\left(k_{\mu,m}C_l^y\right)^{\frac{1}{x}}\left[-\ln\left(\frac{N_m}{N_0}\right)\right]^{\left(1-\frac{1}{x}\right)} \tag{2.6}$$

where N_0 is the initial concentration of the microorganism m, $k_{\mu,m}$ is the inactivation rate constant for the microorganism m, C_l the disinfectant (i.e. ozone or chlorine) concentration, and x and y are constants. Table 2.6 lists literature-reported constants for various pathogens.

Inactivation rate constants depend on the target species and temperature. For the case when $x = y = 1$ the Hom-Haas model reduces to the Chick-Watson model:

$$S_{N_m} = \frac{dN_m}{dt} = -k_{\mu,m} C_l N_m \tag{2.7}$$

Although the Chick-Watson model does not consider the effect of initial microorganism concentration and has a limited applicability, it has been more popular in practical modeling than the Hom-Haas model due to its simplicity (Wols et al. 2010a; Bolaños et al. 2008; Bartrand 2006; Huang et al. 2004). However, as affordable computational power is becoming available, more accurate and complicated kinetics models have been employed, such as the Hom-Haas model (Zhang et al. 2007; Zhang 2006) or other application-specific models (Talvy et al. 2011).

The inactivation models used in UV disinfection are similar to those used in ozone and chlorine disinfections except that the disinfectant concentration in equations (2.6) and (2.7) needs to be replaced with incident radiation, *G*. (Models for *G* were summarized in Table 2.5.) For example, in the Chick-Watson model, which has been widely used in modeling of UV disinfection (Chiu et al. 1999; Ducoste et al. 2005; Lyn et al. 1999), the source term can be written as

$$S_{N_m} = -k_{UV,m} G N_m \tag{2.8}$$

where $k_{UV,m}$ (unit: $m^2/(Ws)$) is the intrinsic rate constant of the microorganism *m*.

2.3.2 Parameter Studies of Modeling Disinfection Process

Several parameters related to disinfection efficiency have been studied via CFD. These parameters can be divided into the following three categories:

- Operation parameters
- Configuration parameters

- Parameters in modeling

The operation parameters studied by CFD include: pH (Kim 2005), temperature (Kim 2005; Talvy et al. 2011), bubble size variation (Talvy et al. 2011), ozone-consuming substances (OCS) variation (Huang et al. 2004), dead zone volume percentage (Lee et al. 2011) and kinetics and mixing state among others. The studied configuration parameters include: inlet configurations (Greene 2002; Greene et al. 2002), the direction and magnitude of the inlet flow (Ta and Hague 2004), the method of tracer injection (Zhang et al. 2008), sampling locations (Zhang et al. 2008), the ratio of length of flow to width of flow (Peplinski et al. 2004) and wall reflection of light (Chen et al. 2011). The parameters in modeling are the parameters involved in development of the CFD analysis, such as the effect of turbulence model, time step (Peplinski et al. 2004), turbulent intensity of inflow conditions (Huang et al. 2002), turbulent Schmidt number (Kim et al. 2013) and so on. The impacts of studied parameters on disinfection efficiency or predicting disinfection efficiency are summarized in Table 2.7.

A better understanding of the relationships between disinfection efficiency and operation parameters is helpful for troubleshooting existing facilities in water treatment plants. For example, the CFD simulation of the flow in the Tailfer plant, in Belgium (Talvy et al. 2011), helped to identify problematic issues caused by the low operating temperature. Another example is that sampling location has been observed to have a significant influence on tracer RTD prediction (Zhang et al. 2008), suggesting that multiple sampling points should be employed during physical measurements.

2.3.3 Optimization of the Configuration of Contactors

Contactor configuration optimization which aims to obtain the maximum disinfection efficiency is an important research direction in water and wastewater treatment industry. Note

that here hydraulic efficiency is considered an index of disinfection efficiency in accordance with the majority of the literature.

It is well-known that reduction of dead zones and short-circuiting leads to improved disinfection efficiency (Wols et al. 2008a; Bolaños et al. 2008; Kim et al. 2010a; Amini et al. 2011; Zhang et al. 2013b). Increasing the number of baffles is a commonly used approach to reduce dead zones and diminish short-circuiting. Several studies have concluded that an increase of the number of baffles usually leads the fluid flow to approach plug-flow conditions characteristic of a plug-flow reactor (Kim et al. 2010a; Amini et al. 2011; Wols et al. 2008a). Essential for achieving plug-flow conditions is the use of spatial separation of the flow to limit diffusion between chambers. However, a minor side effect caused by the increment of baffles is that more energy needs to be spent on driving the flow through the contactor as will be seen in Chapter 6 of this document as well as in a recently published article (Zhang et al. 2013b).

Instead of increasing the number of baffles, proper rearrangement of chambers may have the same effect of reducing dead zones and diminishing short-circuiting. In the study of Amini et al. (2011), it is shown that the hydraulic efficiency of a six-baffle wall contactor with a proper rearrangement can be higher than that of a contactor with nine baffle walls.

Proper adjustment of the locations of inlet, outlet and diffusers may also improve hydraulic conditions. The hydraulic efficiencies of nine configurations of a disinfection tank with different inlet and outlet locations were compared by Stamou (2008). The one with the best hydraulic efficiency was proposed for construction. Cockx et al. (1999) conducted two-phase flow simulations of an initial disinfection tank and a refurbished disinfection tank with an adjustment of the locations of ozone diffusers. Their numerical results found that the refurbished disinfection tank could achieve a higher inactivation level for *Cryptosporidium* at the same

operation costs. Modifying the shape of the baffle (such as adding a turning vane at the baffle end) to make the flow turn smoothly, is another way to reduce dead zones (Wols et al. 2010a). Tafilaku et al. (2010) conducted a numerical study on three designs of a disinfection clearwell with concentric baffles, conventional serpentine baffles and modified serpentine baffles. Results showed the configuration with conventional serpentine baffles had the highest hydraulic efficiency among these three configurations.

Minor modifications of existing contactors to improve disinfection efficiency have been made based on troubleshooting existing contactors via CFD. Such modifications include adding chambers, increasing end gap and so on (Phares et al. 2009). Attempts at optimizing the configuration of contactors with the aid of CFD simulations are summarized in Table 2.8.

2.4 Challenges in Disinfection Process Simulation

Most reported studies have focused on flow and tracer transport simulation, and few studies have involved the simulation of chemical reaction process as well (Cockx et al. 1999; Greene 2002; Huang et al. 2004; Zhang 2006; Bartrand 2006; Zhang et al. 2007; Bolaños et al. 2008; Wols et al. 2010a; Talvy et al. 2011). Studies that have incorporated inactivation kinetics modeling into CFD are even fewer (Huang et al. 2004; Zhang 2006; Zhang et al. 2007; Bolaños et al. 2008; Wols et al. 2010a; Talvy et al. 2011). The present review study found that the challenges existing in the disinfection process simulation include: 1) unsteady flow effects, 2) multiphase flow effect, 3) complexity of reaction system, 4) uncertainty of inactivation kinetics, and 5) closure problem for chemical source terms.

2.4.1 Unsteady Flow Structure Effect

As mentioned earlier, the accuracy of flow simulation is critical to disinfection process modeling. The majority of studies have successfully employed RANS for flow and tracer

transport simulation. As will be seen in the upcoming chapter 4, the primary reason why RANS has been successful for baffled contactors is because steady or quasi-steady short-circuiting exists in most baffled contactors and the unsteady (intermittent) small-scale eddies have negligible impact on tracer transport (Zhang et al. 2013a). However, since RANS resolves the mean flow only, a significant error may appear once energetic unsteady flow structures develop in the flow. Recent reports as well as the study in Chapter 4 have pointed out that under such conditions LES is a more suitable approach than RANS due to its capability of capturing unsteady flow features (Wols et al. 2010c; Kim et al. 2010a).

In a UV disinfection application, Wols et al. (2010c) found that RANS wrongly predicts local flow features around a UV lamp. This phenomenon was mainly caused by Kármán Vortex Street which is a typical unsteady flow structure in a flow around a blunt body. LES was employed and matched the experimentally measured velocity profile better than RANS. The author in this dissertation (see Chapter 4) investigated a baffled contactor and a column contactor which are typically used for ozone and chlorine disinfection. Results showed that LES is a more reliable strategy than RANS in simulating tracer transport in column contactors due to its ability to better predict the spatial transition to turbulence characterizing the flow. However, in baffled contactors where such transition does not occur and the flow is characterized by a quasi-steady short circuiting jet and dead zones, RANS performs on par with LES.

Besides the significant impact on tracer transport, unsteady flow structures are expected to have considerable impact on reaction and inactivation processes. Further exploration of this issue using higher resolution approaches such as LES, detached LES (Spalart et al. 1997; Strelets 2001) or even DNS should be explored in the future as computational power becomes more affordable. Detached LES or DES is a hybrid between LES and RANS. In regions where

unsteady features are important the DES behaves as LES and in regions where the mean component is the primary feature DES behaves as RANS.

2.4.2 Multi-phase Flow Effect

For ozone disinfection process simulation, a multi-phase flow simulation should be more accurate than a single-phase flow simulation since it is closer to reality. However, the majority of previous studies tended to neglect the effect of gas phase in the disinfection process for two reasons: 1) unknown parameters, such as bubble size distribution, mass transfer coefficients, models for closure of the two-phases, etc.; 2) a single-phase flow simulation is algorithmically simpler and less computationally expensive. Only a small portion of studies have conducted multi-phase flow simulations (Cockx et al. 1999; Bartrand et al. 2009; Ta and Hague 2004; Bolaños et al. 2008; Talvy et al. 2011).

Bartrand et al. (2009) found that for water flow down a vertical column contactor with a counter (upward) gas flow, an increment of gas flow rate would promote stronger short-circuiting in both physical experiments and numerical simulations. Based on the simulation results, the explanation for this was that the upward flow of the liquid phase within the bubble plume and reduction of the effective column cross sectional area through which downward-flowing liquid passes result in stronger short-circuiting. However, for a baffled contactor, especially a full-scale baffled contactor, the impact of gas flow on water flow may be less significant due to a lower ratio of gas flow rate to liquid flow rate. For example, the ratio of gas flow rate to liquid flow rate for a typical full-scale baffled contactor in a water treatment plant is 1.6%~3.3% (Talvy et al. 2011) while that for a column contactor the ratio is 7.6%~45% (Bartrand et al. 2009; Bolaños et al. 2008). Furthermore, in a column contactor, the gas flows in opposite direction to the bulk water flow and thus can significantly affect the overall flow,

whereas in a baffled contactor, the gas flow can potentially influence the water flow only in the chambers where the gas diffusers are located, thereby making the effect of the gas flow on the overall flow less significant. In order to better understand the role of gas flow in the disinfection processes for both column and baffled contactors, further exploration via simulations and physical experiments is required.

2.4.3 Complexity of Reaction System

The overall complexity of the reaction system is mainly caused by the variety of species present in the system and the complexity of kinetics for each elementary reaction. Usually, the reaction system in a disinfection process consists of an excessively high number of elementary reactions to be covered by modeling. Thus, it is necessary to develop a truncated or reduced reaction mechanism. The reduced reaction mechanism should contain a minimum number of species while preserving the characteristics of the reaction system.

An approach to simplify a reaction system is time-scale analysis (Okino and Mavrovouniotis 1999). The basic steps behind time-scale analysis are

- Identify regions exhibiting different time scale behavior;
- Identify species having a fast reaction rate or fast time scale within each region and lump them into a smaller set of pseudo species;
- Simulate the dynamics of the reaction system by a smaller set of variables characteristic of each region.

Another approach is to consider only the global reaction of the species of interest. This is commonly used in chlorine and ozone disinfection process simulation.

Besides the number of reactions, the complexity of reaction kinetics serves to increase the difficulty of modeling as well. Typically, first-order reaction kinetics is sufficient to describe the

reaction system. However, in reality, the reaction rate could be higher or lower than first order, or in other complicated forms. For example, the kinetics of ozone decomposition used in reported studies is of first-order reaction rate (Cockx et al. 1999; Huang et al. 2004; Zhang 2006; Bartrand 2006; Zhang et al. 2007; Bolaños et al. 2008; Wols et al. 2010a, b; Talvy et al. 2011); however, as reported by Gurol and Singer (1982), ozone decomposes by a second-order reaction. The uncertainty of the reaction rate constants also has a significant impact on the accuracy of predictions as will be seen in Chapter 5. Since reaction rate constants depend on environmental parameters, such as pH and temperature, it is critical to use appropriate reaction rate constants in modeling.

In this dissertation, the reaction system in ozone disinfection process has been simplified as a 6-species-6-reaction system. The kinetics of bromate formation is represented by a series of reactions which have not been employed in previous CFD studies. Details of this reaction system are provided in Chapter 3.

2.4.4 Uncertainty of Inactivation Kinetics

For chemical disinfection (e.g. ozone disinfection, chlorine disinfection), the specific mechanisms of microorganism inactivation are not well understood (Crittenden et al. 2005). Inactivation kinetics could be of either first-order reaction or second-order reaction or even higher-order. And the inactivation rate depends on the properties of each microorganism, the disinfectant and the environmental parameter, such as temperature and pH. Furthermore, the inactivation rate can vary by as much as six orders of magnitude from one organism to another, even for the same disinfectant (Crittenden et al. 2005). How to overcome the uncertainties in inactivation kinetics and rate constants remains a challenge in the modeling of disinfection process, especially with various pathogens.

Several inactivation kinetic models have been developed. Gyurek and Finch (1998) have written a summary of the inactivation kinetic models. In experiments of ozone disinfection for HPC bacteria (Gyurek and Finch 1998), the Incomplete gamma Hom (I.g.H.) model showed the best performance in describing the HPC bacteria survival curve. However, the most commonly employed inactivation kinetic model in CFD has been the Chick-Watson model which has the simplest formula, as described earlier.

Although inactivation kinetics models have been developed, there is still important information missing for conducting a CFD simulation involving inactivation. For instance, up to date, the appropriate amounts of ozone needed to inactivate *Cryptosporidium* oocysts in water at various temperatures and pHs have not been clearly defined (Juranek 1995). As a result, previous disinfection modeling studies (Zhang 2006; Zhang et al. 2007; Wols et al. 2010a, b; Bolaños et al. 2008; Talvy et al. 2011; Huang et al. 2004) have not considered the consumption of disinfectant by pathogens. Note that the existing inactivation models such as the Hom-Haas model and the Chick-Watson model are only for calculating the pathogen decay rate without considering the corresponding consumption of disinfectant. Fortunately, in practice the consumption by microorganisms is usually low. Thus it is acceptable to neglect the consumption by microorganisms in modeling.

2.4.5 Turbulence-chemistry Interaction

Closure for chemical source terms is important in the modeling of finite rate reactions. Usually the reactions in disinfection process can be categorized into finite-rate chemistry or slow chemistry. For slow chemistry (as is the case for the ozonation process reactions considered in the present study) the turbulence-chemistry interaction is simple since mixing by turbulence is fast enough that the mixing is complete before the reaction occurs. A first-order moment closure

method has been commonly used to treat the turbulence-chemistry interaction in slow chemistry. However, it is much more challenging to treat the turbulence-chemistry interaction in finite rate chemistry. Ranade (2002) and Fox (2003) have explained the closure problem encountered in the modeling of reactive flow with finite rate chemistry. In this section, a brief introduction of this closure problem and potential solutions are discussed.

2.4.5.1 Turbulence-chemistry Interaction in Disinfection Process Modeling

Closure of chemical source terms is required for RANS or LES, but not for DNS. In RANS, the governing equation of species transport phenomena is Reynolds-averaged. In the case of Eqn. (2.4), Reynolds-averaging leads to:

$$\frac{\partial \langle C_i \rangle}{\partial t} + \langle u_j \rangle \frac{\partial \langle C_i \rangle}{\partial x_j} + \frac{\partial \langle C_i' u_j' \rangle}{\partial x_j} - \frac{\partial}{\partial x_j}\left(D_i \frac{\partial \langle C_i \rangle}{\partial x_j} \right) = \langle S_{C_i} \rangle \tag{2.9}$$

where $\langle\ \rangle$ denotes the Reynolds-averaging operation. The Reynolds average of a quantity corresponds to the mean of that quantity. The primes in Eqn. (2.9) correspond to turbulent fluctuations about their corresponding means. In a RANS simulation these fluctuations are not accessible (computed), thus the term $\langle C_i' u_j' \rangle$ in Eqn. 2.9 (arising from Reynolds-averaging) needs to be closed or modeled. This closure problem is similar to the classical Reynolds stress closure problem in the momentum (Navier-Stokes) equations requiring the use of a turbulence model such as the well-known *k*-ε turbulence model (Wilcox 1994). Note that LES is characterized by a similar closure problem arising due to the spatial filtering of the equations (in similar fashion to the Reynolds-averaging operation in RANS). These closure problems in RANS and LES will be described in more detail in the upcoming chapter. The most difficult term to close or model in Eqn. (2.9) is the Reynolds-averaged chemical source term $\langle S_{C_i} \rangle$. The nonlinearity of the chemical source term gives rise to the need for a closure. Take natural organic matter in ozone disinfection

(NOM) for example. Recall the source term for NOM in Table 2.1; thus, the Reynolds-averaged source term for concentration of NOM would be

$$\langle S_{[NOM]} \rangle = -k_{NOM}\{\langle [NOM] \rangle \langle C_l \rangle + \langle [NOM]' C_l' \rangle\} \tag{2.10}$$

where k_{NOM} is a second-order rate constant; $\langle C_l \rangle$ and C_l' are mean and fluctuation of the concentration of dissolved ozone respectively; $\langle [NOM] \rangle$ and $[NOM]'$ are mean and fluctuation of the concentration of fast reacting NOM respectively.

The covariance term in Eqn. (2.10), i.e. $\langle [NOM]' C_l' \rangle$, must be closed or modeled since $[NOM]'$ and C_l' are fluctuations that are not accessible in RANS.

If the reaction rate is much slower or much faster than the turbulent mixing rate, the source term in (2.10) can be modeled by a first-order closure method (i.e. $\langle [NOM]' C_l' \rangle = 0$ in Eqn. (2.10)) (Fox 2003). This will be the closure adapted in this dissertation. If the reaction rate is comparable to the mixing rate, the covariance term in (2.10) cannot be neglected. The covariance term could be a complicated function of the reaction rates and flow condition making it difficult to find a general method for obtaining a closure model over a wide range of chemical time scales.

2.4.5.2 Potential Models for Finite-Rate Reaction in Disinfection Process

The physical significance of covariance terms such as $\langle [NOM]' C_l' \rangle$ is the interaction between reaction and turbulence mixing or turbulence chemistry interaction. To model the turbulence-chemistry interaction could be even more challenging than to develop a pure turbulence model (i.e. a Reynolds stress model) due to the complexity of the interactions and the number of species in a reaction system (Georgiadis et al. 2009).

The existing models for finite-rate chemistry can be categorized into two groups: PDF (probability distribution function) models and non-PDF models.

The PDF models, especially the transport PDF models (Ranade 2002), can provide a complete description of the reaction process. However, to solve the PDF model is a challenge for CFD codes which are based on Eulerian system. Usually, the PDF models are suitable for Lagrangian CFD approaches such as Monte-Carlo methods. These models are computational-intensive and difficult to be implemented into Eulerian CFD codes. A solution to this drawback is to use a presumed or pre-determined PDF model rather than solving for it. But, the presumed PDF model can be unreliable and inaccurate if the statistical data of the underlying physical experiment is not available as is the common situation. Thus currently, PDF models are usually not practical for modeling chemical disinfection processes.

Early attempts at using non-PDF models were simple, focusing on simulating the interaction of micro-mixing and chemical reactions. Examples include the engulfment model (Baldyga and Bourne 1989) and the Interaction by Exchange with the Mean (IEM) model (David and Villermaux 1975). However, the effects of large scale (or macro) flow structures, such as short-circuiting and dead zones occurring in disinfection contactors, were not considered in these models (Ranade 2002). However, the simplicity of the IEM model makes it useful for verifying sensitivity to micro-mixing effects (Fox and Villermaux 1990; Fox 1991; Fox et al. 1994). The IEM model is a simple age-based model. The more complicated age-based models are based on residence time distribution (RTD) obtained from tracer tests. Since RTD is usually generated by the data measured at the exit of a reactor, the aged-based models cannot be used to predict the concentration distribution inside a reactor. Note that the age-based models are based on a Lagrangian system.

The linear eddy model (Kerstein 1988, 1990, 1992) is another kind of model which aims to model the turbulent mixing and reaction of a scalar quantity (e.g. a chemical species). The

basic idea of the linear eddy model is to treat convection and diffusion separately as two different mechanisms acting on the evolution of chemical species. This provides a useful and insightful way to look into the turbulent mixing of the reacting species. Monte-Carlo simulation is required for the time evolution of chemical species thus making the linear eddy model generally inaccessible to the more popular Eulerian-based CFD codes.

Next the discussion turns focus on models which are more suitable to be implemented into Eulerian-based CFD codes. These models are moment closures, including both first-order and higher-order moment closures, and multi-environment models with and without presumed PDF models.

In the situation that the chemical time scales are all large compared with the mixing time scale, i.e. the slow-chemistry limit, a simple first-order moment closure can be adequate. The 'default' closure in most commercial CFD codes is to assume that all scalar co-variances are zero (Fox 2003), which is the simplest first-order moment closure. This will also be the case in this work. However, if any chemical reaction is faster than the turbulent mixing, this approximation would result in a poor prediction. Thus, first-order moment closures should be used cautiously when applied to reactive flow with finite chemistry.

Several attempts have made at developing higher-order moment closures (Dutta and Taebell 1989; Heeb and Brodkey 1990; Shenoy and Toor 1990). The simplest closure approach is to relate the covariances of reactive scalars to the variance of mixture fraction which can be computed by solving inert-scalar-variance transport equations along with the transport equation for the mean mixture fraction (Fox 2003). Although this approach has the ability to be applied to one-step chemistry, the extension of this approach to multi-step chemistry has proven to be unreliable (Fox 2003). A more general higher-order moment closure strategy consists of solving

the transport equations for the scalar covariances directly. However, as shown by Fox (2003), this strategy would generate higher order moments (e.g. triple correlations) that need extra models which have not been developed yet.

Multi-environment models are another category of Lagrangian models. In these models, the well macro-mixed reactor is broken up into sub-grid-scale environments with uniform concentrations. For example, in a four-environment model (Villermaux and Falk 1994), environment 1 contains fluid entering the system through the first feed stream; environments 2 and 3 contain partially mixed fluid; and environment 4 contains fluid entering the system through the second feed stream. Chemical reactions can only occur in environments 2 and 3. Such a model has been used to represent mixing in semi-batch reactors of different sizes studied by a novel parallel-competing test reaction and mixing of a stream of initiator in a recycle tubular reactor packed with static mixers for the polymerization of styrene (Villermaux and Falk 1994). Multi-environment models have provided a flexible yet simple framework for modeling turbulent reactive flow. And it has been demonstrated that multi-environment models have the ability to simulate not only slow and fast reactions (Ranade and Bourne 1991), but also finite-rate reactions (Ranade 2002). However, since the relative volume of each environment and exchange rates between environments must be specified, it is a challenge to fit the parameters in the model when applied to general problems, especially problems with complex geometries.

As demonstrated by Fox (1998; 2003), it is possible to reformulate multi-environment models in terms of a multi-peak presumed joint PDF leading to a closed form of the chemical source term. Fox (1998) successfully applied a four-environment presumed PDF model to fully-developed turbulent flow with a two-step reaction in a one-dimensional tubular reactor. Comparing to a full PDF model, the primary advantage of multi-environment presumed PDF

models is the fact that it is not necessary to integrate with respect to the joint composition PDF in order to evaluate the chemical source term since the latter has been closed. However, it requires particular attention to the definition of the micro-mixing terms when the model is extended to inhomogeneous flow (Fox 1998), or to homogeneous flows with uniform mean scalar gradients (Fox 2003).

There are a few other non-PDF models for simulation of reactive flow, for example, laminar diffusion flamelets (Peters 1984, 2000) and the conditional-moment closures (Tsai and Fox 1995). These models are not discussed here as they have been primarily designed for combustion. A summary of the closures for the potential chemical source term in disinfection process simulation is shown in Table 2.9.

The above models have been mainly developed for RANS simulation. In LES, a similar closure problem exists requiring modeling of the covariance of spatially filtered chemical source terms, which are to take into account the sub-grid turbulence-chemistry interaction. Closures based on LES have been developed for combustion (Fureby 2008; Pitsch et al. 2008). However, to the authors' knowledge, no LES-based closure has been developed for water flows with finite-rate chemistry which are commonly seen in water and wastewater treatment plants. Nevertheless, semi-empirical methods, such as the Partially Stirred Reactor (Correa 1993), the Eddy Dissipation Concept (EDC) (Berglund et al. 2008; Fureby 2007) and Thickened Flame Model (TFM) (Colin et al. 2000) developed for LES simulation of combustion are valuable references for developing a closure method suitable for disinfection process simulation. With the growing popularity of LES due to the advancement of computational power, attempts have been made to develop closures for LES in the last decade. For example, an attempt to model the covariance of filtered chemical source terms in LES was made by Fox (2003). According to Fox (2003), in

theory the multi-environment presumed PDF models initially developed for RANS can be extended to LES. And all the procedures in the RANS-based multi-environment presumed PDF models can be re-used in developing an LES-based multi-environment presumed PDF model with a few minor modifications.

2.5 Chapter Summary

CFD applied to disinfection studies has become more prominent due to advancement of computing power. Studies reviewed here concentrated on the development of a simulation method or framework for the disinfection process, the impacts of parameters on modeling disinfection, and optimization of the configuration of disinfection contactors. Relationships between parameters, such as operation parameters (e.g. pH and temperature), configuration parameters (e.g. flow length to width ratios), modeling parameters, and disinfection efficiency were summarized. Ways that can increase disinfection efficiency by optimizing contactor configuration were summarized as well. Challenges in simulation of disinfection process were identified and discussed. For example, challenges in resolving unsteady flow features may be overcome by advanced turbulence resolving approaches such as LES. This is one of the major topics of this dissertation and will be explored further in the next chapter. Turbulence-chemistry interaction is the most challenging issue. Although several closures were discussed for turbulence-chemistry interaction in this review, it is difficult to assess the accuracy of such closure models for turbulence-chemistry interaction unless the errors caused by poorly resolved or unresolved unsteady flow features, multi-phase flow, and uncertainty of reaction system have been sufficiently reduced. Thus, this dissertation focuses on the following two topics: 1) evaluation of computational methodologies for turbulent flow in ozone contactors with emphasis on hydraulic performance; 2) the development of a reaction modeling framework with a kinetics-

based sub-model for bromate formation. Prior models of bromate formation in CFD simulations have been empirically based. In these previous models, tuning of the reaction rate constant based on physical experimental data from the disinfection system being modeled is required. Thus the kinetics-based model developed and tested here represents a move towards reaction modeling independent of disinfection system-specific experimental data.

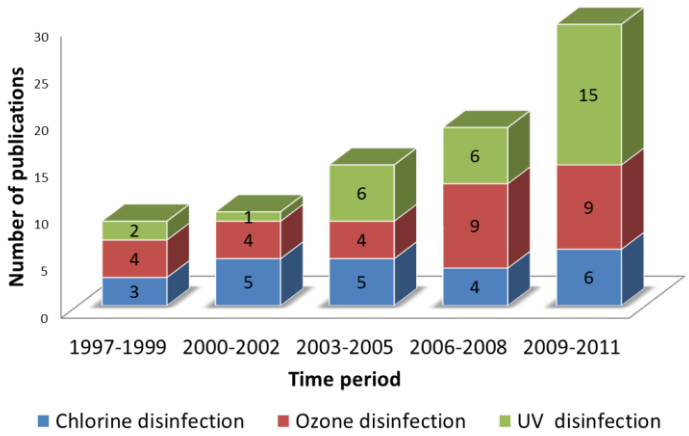

Figure 2.1: Statistics of publications on CFD applied to disinfection (searched with Engineering Village and Web of Knowledge).

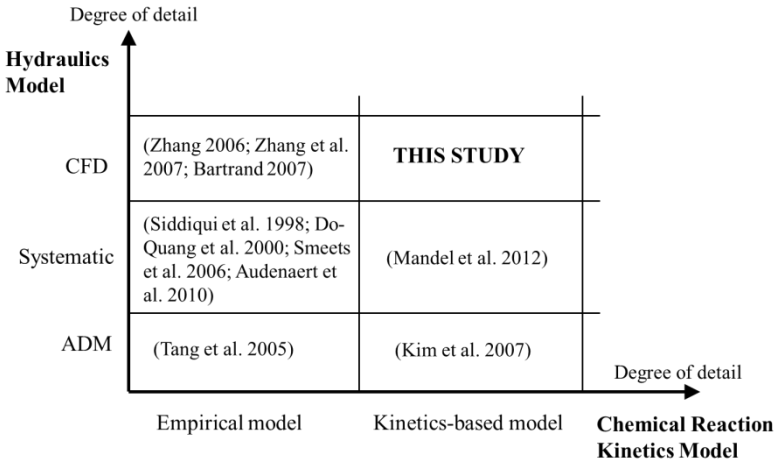

Figure 2.2: Modeling frameworks of previous full-scale contactor tank studies (adapted from Mandel et al. 2012).

Table 2.1: Commonly used source terms of transport equations for modeling ozone disinfection process.

Species	Source terms for transport equations	References
Dissolved ozone, C_l	$S_{C_l} = -k_d C_l$	Sotelo et al. (1987); Beltrán (1995); Muroyama et al. (1999); Huang et al. (2004)
NOM	$S_{[NOM]} = -k_{NOM}[NOM]C_l$	Lev and Regli (1992); Chen (1998); Kim et al. (2002)
Bromate, C_B	$S_{C_B} = k_B C_l$	von Gunten (1994); Tang et al. (2005); Kim (2002)
Tracer	$S_{C_T} = 0$	Zhang (2006); Zhang et al. (2007)

Table 2.2: An overview of disinfection calculation methods (adapted from Wols et al. (2010a)).

Method	Required information
CT10-method	RTD (residence time distribution)
CSTR-method	Number of compartments
Segregated Flow Analysis	RTD
Micro-mixing analysis	RTD
Eulerian mean CT (concentration-contact time) value	CFD (flow velocities, turbulent diffusivities, disinfectant concentrations, etc.)
Eulerian direct inactivation	CFD (flow velocities, turbulent diffusivities, disinfectant concentrations, etc.)
Particle tracking	particle trajectory, CFD (disinfectant concentrations)

Table 2.3: An overview of the four stages of disinfection process modeling by CFD (adapted from Wols et al. (2010b)). Note that the flow simulation stage underlies the entire framework.

Stages	Methodologies and models	Physical quantities
Stage 1: Flow Simulation	RANS or LES based on Navier-Stokes Equations; Turbulence modeling for RANS or SGS modeling for LES.	Flow fields (e.g. velocity, pressure); Turbulent properties
Stage 2: Tracer Transport Simulation	Advection-diffusion equation for passive scalar	Tracer concentrations; Residence time distribution
Stage 3: Reaction Process Simulation	Species transport equations; Modeling for chemical source terms	Chemical concentrations (e.g. dissolved ozone); Incident radiation for UV disinfection; disinfection contact times
Stage 4: Inactivation Simulation	Species transport equations; Inactivation kinetic modeling	Concentrations of microorganisms; Microorganisms survival ratio

Table 2.4: A summary of the reaction systems used in CFD simulation of ozone disinfection.

Studies	Ozone decay	Reaction between ozone and IOD or NOM or TOC	Bromate formation
Cockx et al. (1999)	√	√	
Huang et al. (2004)	√	√	
Zhang (2006)	√	√	√
Bartrand (2006)	√	√	√
Zhang et al. (2007)	√	√	√
Bolaños et al. (2008)	√		
Wols et al. (2010a)	√		
Talvy et al. (2011)	√		
This dissertation	√	√	√

Table 2.5: A summary of the radiation models used in the modeling of UV disinfection process.

Radiation models	Expressions	Sources
Non-attenuate model	Algebraic equation for incident radiation G is $G = I = I_{max}\left(\frac{r_s}{r}\right)$ where r is the radial distance from the lamp, I_{max} and r_s are the light intensity and radius at lamp surface.	Wright and Hargreaves (2001)
Modified P-1 radiation model	Transport equation for the incident radiation G is $\nabla \cdot (\Gamma \nabla G) - aG = 0$ $\Gamma = \frac{1}{3a}$ where a is the absorption coefficient $a = -100\ln(\mathrm{UVT})$ UVT is UV radiation transmission. Alternatively, $\Gamma = \frac{1}{3(a+\sigma_s) - C_1\sigma_s}$ where a is the absorption coefficient, σ_s is the scattering coefficient, and C_1 is the linear-anisotropic phase function coefficient	(1) Chen et al. (2011); Yu et al. (2008) (2) Li et al. (2011); FLUENT 6.3 User's Guide.
Finite Line Source or Multiple Point Source Summation (MPSS) Model	$G(r,z) = \sum_{i=1}^{n} \frac{\frac{P}{n}}{4\pi l_i^2} exp\left[-\sigma_w (r - r_L)\frac{l_i}{r}\right]$ where z [cm] represents the axial distance and l_i is the distance from the current location [cm] to the point source number n_i out of a total of n sources. Results were found to be independent of the number of sources with n > 100.	Sozzi and Taghipour (2006); Hofman et al. (2007b); Bolton (2000); Lyn et al. (1999); Younis and Yang (2010)
Multiple segment source summation (MSSS)	Available in Liu et al. (2004)	Liu et al. (2004); Wols et al. (2012); Wols et al. (2010b, c); Liu et al. (2007)
Modified line source integration (LSI) model	Available in Liu et al. (2004)	Zhao et al. (2009); Liu et al. (2004)

Table 2.5 (Continued).

Radiation models	Expressions	Sources
Infinite-line source model or radical model	$I(r) = \frac{I_0 T^{\alpha(r-R_i)}}{2\pi r}$ where r is the radial distance from the lamp, I_0 is the UV lamp output (energy rate per unit length), T is the UV transmittance of the fluid, R_i is the radius of the UV lamp sleeve, and α is the extinction coefficient multiplied by the concentration of the absorbing species. For this model, the radiation fluence rate and irradiance become identical.	Taghipour and Sozzi (2005); Sozzi and Taghipour (2006)
Presumed dose distribution or exponential probability density function (PDF)	$f(D_{UV}) = \lambda \cdot \exp\left(-\lambda(D_{UV} - D_{\min})\right)$ where D_{UV} represents the UV dose, $D_{\min}$ is the shift in dose distribution and λ is a distribution factor.	Wols et al. (2011)

Table 2.6: Reported constants in the Hom-Haas model for ozone inactivation (adapted from Zhang (2006)).

Microorganism	$k_{\mu,m}$	x	y	Source
Cryptosporidium Parvum oocysts	$0.68 \times 1.08^{T-22}$	0.71	0.73	Gyurek et al. (1999) Li and Gyurek (2001)
Giardia	$2.35 \times e^{0.0723 \times T}$	1	1	Carlson et al. (2001)
Viruses	$4.90 \times e^{0.07 \times T}$	1	1	Carlson et al. (2001)

Note that, the T used in the expressions of calculating $k_{\mu,m}$ means water temperature (℃)

Table 2.7: The impacts of studied parameters on disinfection efficiency or predicting disinfection efficiency.

Category	Item	Relationship	Source
Operation parameters	pH	pH is favorable for achieving high inactivation efficiency.	Kim (2005)
	temperature	As temperature decreases, predicted inactivation efficiency decreases.	Kim (2005); Talvy et al. (2011)
	bubble size variation	Bubble size variation causes lower ozone gas-liquid transfer rate and consequently causes lower concentration of dissolved ozone and lower pathogen removal efficiency.	Talvy et al. (2011)
	ozone-consuming substances (OCS) variation	The increase in OCS loading significantly increases *C. parvum* survival ratios.	Huang et al. (2004)
	method of tracer injection	Method of tracer injection slightly affects tracer RTD results.	Zhang et al. (2008)
	kinetics and mixing state	Disinfection efficiency is affected by both mixing and kinetics (and their interaction).	Greene (2002); Greene et al. (2006)
	dead zone volume percentage	Higher dead zone volume percentage leads to lower disinfection efficiency.	Lee et al. (2011)
Configuration parameter	inlet configuration	Inlet configurations, such as inlet baffle and inlet pipe, can significantly impact reactor hydrodynamics.	Greene (2002); Greene et al. (2002) Greene et al. (2006)
	the direction and magnitude of the inlet flow	For a single-column contactor with side entry, the flow pattern was found to be crucially dependent on both the direction and magnitude of the entry velocity from the inlet pipe.	Ta and Hague (2004)

Table 2.7 (Continued)

Configuration parameter	sampling locations	Sampling location has a significant influence on tracer RTD prediction or measurement.	Zhang et al. (2008)
	flow length to flow width ratio	High flow length-to-width ratio results in a high level of disinfection credit (per EPA standards) for a given concentration of disinfectant.	Peplinski et al. (2004)
	wall reflection of light	At higher inactivation levels, the effect of wall reflection is more influential.	Chen et al. (2011)
Parameters in modeling	time step interval	Larger time step serves to erroneously increase the amount of tracer dispersion.	Peplinski et al. (2004)
	turbulent intensity of inflow	Tracer RTD prediction can be strongly dependent on turbulent intensity of inflow boundary condition.	Huang et al. (2002)
	turbulent Schmidt number	Turbulent Schmidt number requires calibration since it is found to depend on geometry of disinfection tank.	Kim et al. (2013a)

Table 2.8: The methods of optimizing the configuration of contactors.

Optimizing modifications	**Objective**	**Examples**
Increasing the number of baffles	Separate flow spatially to hinder diffusion in order to approach plug flow	Kim et al. (2010a); Amini et al. (2011); Zhang et al. (2013b); Wols et al. (2008b); Evans (2003)
Rearrangement of chambers	To diminish dead zone regions	Melissa (2010); Amini et al. (2011)
Proper adjustment of the locations of inlet, outlet and diffusers	To diminish dead zone regions	Stamou (2008) ; Wright and Hargreaves (2001); Cockx et al. (1999)
Modifying the shape of baffle	To diminish dead zone regions	Wols et al. (2010a)
Troubleshooting with minor modification: adding chamfers, increase end gap	Weaken short-circuiting	Phares et al. (2009)

Table 2.9: Summary of the closures for the chemical source term in disinfection process simulation

Closure approach		Strengths	Limitations	Sources
Moment closures	First-order moment closures	Simple	Only suitable for slow chemistry	Fox (2003)
	Higher-order moment closures using the covariance of mixture fraction	Have the ability to model one-step chemistry	Poor prediction for multi-step chemistry	Fox (2003)
Lagrangian models	The IEM model	Simple and can be applied to check for sensitivity to micro-mixing effects	Does not consider flow effect	David and Villermaux (1975); Fox and Villermaux (1990); Fox (1991); Fox et al. (1994)
	Age-based model	Simple and can predict concentration at exit (outflow) of a reactor	Cannot be used to predict the concentration distribution inside a reactor	Fox (2003)
	Multi-environmental models	Have the ability to model slow, fast and finite-rate reaction	Empirical parameters existing in the model need to be fitted	Ritchie and Togby (1979); Mehta ad Tarbell (1983); Ranade and Bourne (1991); Ranade (1993); Kolhapure and Fox (1999)
	Multi-environment presumed PDF models	Have the ability to model slow, fast and finite-rate reaction	The presumed PDF needs to be well selected for each situation	Fox (1998); Fox (2003)
Linear eddy model		Have been applied to a wide variety of applications	Computationally-intensive	Kerstein (1988, 1990 and 1992); Cremer and McMurtry (1998)

CHAPTER 3: COMPUTATIONAL FRAMEWORK

This chapter presents the governing momentum and scalar advection diffusion equations comprising the computational framework developed for ozone disinfection of water. These equations are presented within the context of the methodology for computing the turbulent flows of interest (either RANS or LES).

Firstly, RANS and LES methodologies for computing turbulent flows are introduced. In RANS, only the mean component of the flow is computed explicitly (or resolved) while the effect of the unresolved turbulent scales on the mean component is modeled via a turbulent stress or turbulent flux appearing in the governing equations for the mean component. In LES the largest, more energetic scales of the turbulence are explicitly computed (resolved).

In addition to the governing flow equations, this chapter introduces the governing transport equation for a passive, non-reactive dye tracer as well as the residence time statistics evaluated from solutions of this transport equation. These statistics are useful for determining the hydraulic performance of a water disinfection system.

The governing transport equations for the ozonation process are introduced in the latter part of this chapter. Reaction kinetics and turbulence-chemistry interaction are important aspects of these equations. Thus, models or closures for reaction kinetics and turbulence-chemistry interaction are discussed as well. Inactivation of microorganisms is an important part of the disinfection process and two strategies for its simulation are described.

In the simulation of ozone disinfection process, the most commonly considered reactions are ozone decomposition and reaction between ozone and instantaneous ozone demand (IOD) or natural organic matter (NOM). Only a few CFD studies have incorporated bromate formation (Zhang 2006; Bartrand 2006; Zhang et al. 2007). In these studies, an empirical model under the assumption that bromate concentration changes linearly with ozone exposure was used to represent the process (Zhang 2006; Bartrand 2006; Zhang et al. 2007). Although Zhang (2006) and Zhang et al. (2007) have a bromate formation module in their framework, those authors deemed not practical to predict bromate formation due to the sensitivity of the process of bromate formation to water quality. Bartrand (2006) showed prediction of bromate formation in the Alameda County Water District ozone contactor in Fremont, CA. However, the predictions were not compared with physical experimental data.

The present study is the first one to extend beyond empirical modeling and introduce kinetics-based modeling for the formation of bromate within CFD analysis and the first one to compare predicted bromate formation with physical experimental data, the latter comparison to be given in Chapter 5.

The chapter concludes with a description of the numerical method and computer code use to solve the time-dependent, nonlinear partial differential equations of the framework.

3.1 Flow Simulation

The most basic governing equations of incompressible fluid flow are the continuity (conservation of mass) equation and momentum equations. The continuity equation is

$$\frac{\partial u_i}{\partial x_i} = 0 \tag{3.1}$$

where u_i and x_i are velocity and position in i-th direction.

The momentum equations are derived from Newton's second law as

$$\frac{\partial u_i}{\partial t} + u_j \frac{\partial u_i}{\partial x_j} = -\frac{1}{\rho}\frac{\partial p}{\partial x_i} + \nu \frac{\partial^2 u_i}{\partial x_j \partial x_j} + f_i \tag{3.2}$$

where t is time, ρ is fluid density, p is pressure, ν is the kinematic viscosity, and f_i represents a body force (force per unit of mass) in the i-th direction.

A primary issue of flow simulation is how to treat the turbulent scales of the flow. Turbulent flows contain a large range of spatial scales, from the smallest turbulent eddies (i.e. the Kolmogorov micro-scales (Pope, 2000)) where mechanical energy is dissipated into heat, to bulk flow features comparable with the size of the geometry. Three primary strategies or methodologies for dealing with turbulent flows are well-known: Reynolds-averaged Navier-Stokes equations (RANS) simulation, Large Eddy Simulation (LES), and Direct Numerical Simulation (DNS).

3.1.1 Direct Numerical Simulation (DNS)

DNS (Pope 2000) resolves the governing Navier-Stokes equations numerically over the range of all turbulent scales. The range of motions in a turbulent flow grows with the Reynolds number (*Re*). DNS is the most natural approach to simulate turbulent flow. However, the requirements on mesh resolution and time-step put high demands on computational resources, rendering DNS unsuitable for engineering applications. More specifically, the grid for DNS should contain approximately $Re^{9/4}$ points. Such large numbers of grid points make DNS computationally prohibitive. As a result, in this dissertation, DNS is only employed to simulate turbulent channel flow at a modest Reynolds number in order to validate the reliability and accuracy of the numerical method used via comparison with existing DNS results available in the literature obtained with different numerical methods (see appendix B).

3.1.2 Large Eddy Simulation (LES)

LES aims to reduce the requirements on mesh resolution imposed by DNS. The idea of LES is to use a low-pass spatial filter to separate the turbulent flow into resolved (large) scales and unresolved (small) scales. The large flow structures or scales that can be resolved by the numerical method on a given mesh are called resolved scales. The small structures that cannot be captured by the mesh are called sub-grid scales. The influence of sub-grid scales (SGS) on resolved scales is modeled via a SGS stress term included in the momentum equation. The principle of LES lies on the fact that the small unresolved (SGS) scales of the turbulence away from no-slip boundaries are universally homogeneous and isotropic and therefore can be modeled with the same SGS stress for all turbulent flows. Due to the physics of turbulence in the vicinity of an impermeable no-slip wall boundary being considerably different from the other parts of flow, typical SGS models such as the Smagorinsky model (Smagorinsky 1963) are not suitable for representing near-wall sub-grid scales. A common solution is to refine the mesh near no-slip walls to the resolution of DNS. Thus, LES still has a high computational cost that cannot be afforded for engineering applications. LES is sometimes performed with a near-wall model in order to avoid DNS-like resolution of the near-wall region (Pope 2000).

In LES, variable fields (e.g. velocity field $u_i(x_i, t)$) are filtered by a low pass filtering operation in order to be adequately resolved on a relatively coarse grid. The filtering operation (Leonard 1974) is generally defined as

$$\bar{u}_i(x_i, t) = \int_{\Omega} G(r, x_i) u_i(x_i - r, t) dr \tag{3.3}$$

where Ω is the entire flow domain, and $G(r, x_i)$ is a filter function of compact support (i.e. G is non-zero only in a small neighborhood around the point x_i) which satisfies the normalization condition

$$\int_{\Omega} G(r, x_i)dr = 1 \tag{3.4}$$

The filtering operation in (3.3) conducted with a filter function of small compact support is essentially a local averaging of the original variable.

Defining the sub-grid or residual field $u_i''(x_i, t)$ as

$$u_i''(x_i, t) \equiv u_i(x_i, t) - \bar{u}_i(x_i, t) \tag{3.5}$$

The original velocity field can be decomposed into resolved and unresolved (SGS) components:

$$u_i(x_i, t) = \bar{u}_i(x_i, t) + u_i''(x_i, t) \tag{3.6}$$

Application of the spatial filtering operation in (3.3) to the governing flow equations in (3.1) and (3.2) leads to the filtered continuity equation and Navier-Stokes equations, expressed as

$$\frac{\partial \bar{u}_i}{\partial x_i} = 0 \tag{3.7}$$

$$\frac{\partial \bar{u}_i}{\partial t} + \bar{u}_j \frac{\partial \bar{u}_i}{\partial x_j} = -\frac{1}{\rho}\frac{\partial \bar{p}}{\partial x_i} + 2\nu \frac{\partial \bar{S}_{ij}}{\partial x_j} - \frac{1}{\rho}\frac{\partial \tau_{ij}}{\partial x_j} \tag{3.8}$$

governing the larger (more energetic), resolved components of the flow. In these equations an overline denotes LES spatial filtering, vector $\bar{u}_i$ is the filtered velocity, vector x_i is position, t is time, $\bar{p}$ is the filtered pressure, ρ is density, and ν is kinematic viscosity. $\bar{S}_{ij}$ is the filtered strain-rate tensor calculated as

$$\bar{S}_{ij} = \frac{1}{2}\left(\frac{\partial \bar{u}_i}{\partial x_j} + \frac{\partial \bar{u}_j}{\partial x_i}\right) \tag{3.9}$$

The subgrid-scale (SGS) stress in (3.8) is defined as $\tau_{ij} = \overline{u_i u_j} - \bar{u}_i \bar{u}_j$ and represents the effect of the unresolved subgrid-scales on the resolved scales. In LES, the unfiltered velocity u_i is not accessible (or computed) and thus the SGS stress is closed via what is commonly referred

to as an SGS stress model. In this study, the dynamic Smagorinsky SGS model (Smagorinsky 1963; Germano et al. 1991) is employed. Here the SGS stress is decomposed into deviatoric and isotropic components with the latter component being absorbed into the pressure and the former component modeled as

$$\tau_{ij}{}^{\alpha} = -2\nu_t \bar{S}_{ij} \tag{3.10}$$

$$\nu_t = (C_s\Delta)^2|\bar{S}| \tag{3.11}$$

$$\Delta = (\Delta x \Delta y \Delta z)^{1/3} \tag{3.12}$$

$$|\bar{S}| = \left(2\bar{S}_{ij}\bar{S}_{ij}\right)^{1/2} \tag{3.13}$$

where ν_t is the SGS eddy viscosity and $\Delta x,\ \Delta y,$ and Δz are the local mesh spacings in the x_1, x_2 and x_3 directions, respectively. Smagorinsky coefficient C_s is computed dynamically thus varying in space and time (Lilly, 1991). Note that in the LES methodology described here, application of the filtering operation in (3.3) is implicit as the filter function *G* does not appear explicitly in the filtered equations in (3.7) and (3.8). In practice, the computational grid and the numerical method used for solving the equations implicitly act as the filter.

3.1.3 Reynolds-averaged Navier-Stokes Equations (RANS) Simulation

RANS involves the application of Reynolds averaging technique to decompose variables into their means and the fluctuations around these means. Reynolds averaging is an operation that averages a variable or an equation in time. Taking velocity field $u_i(x_i, t)$ for example, Reynolds averaging decomposes the velocity field $u_i(x_i, t)$ into a mean (time-averaged) component $\langle u_i \rangle$ and a fluctuating or turbulent component u_i' in the following way

$$\langle u_i \rangle \equiv \frac{1}{T}\int_T u_i dt \tag{3.14}$$

$$u_i' \equiv u_i - \langle u_i \rangle \tag{3.15}$$

where, for the statistically steady flows considered here, T is a long enough time to ensure satisfaction of the condition

$$\langle u_i' \rangle = 0 \tag{3.16}$$

By applying the Reynolds decomposition, governing equations (3.1) and (3.2) become the Reynolds-averaged continuity equation and Navier-Stokes equations, respectively:

$$\frac{\partial \langle u_i \rangle}{\partial x_i} = 0 \tag{3.17}$$

$$\frac{\partial \langle u_i \rangle}{\partial t} + \langle u_j \rangle \frac{\partial \langle u_i \rangle}{\partial x_j} = -\frac{1}{\rho}\frac{\partial \langle p \rangle}{\partial x_i} + \nu \frac{\partial^2 \langle u_i \rangle}{\partial x_j^2} - \frac{1}{\rho}\frac{\partial \langle u_i' u_j' \rangle}{\partial x_j} \tag{3.18}$$

where a bracket denotes Reynolds-averaging, vector $\langle u_i \rangle$ is the Reynolds-averaged or mean velocity, vector x_i is position, t is time, $\langle p \rangle$ is Reynolds-averaged or mean pressure, ρ is density, and ν is kinematic viscosity. Note that these equations govern the dynamics of the mean component of the flow.

The Reynolds stress tensor $-\langle u_i' u_j' \rangle$ in Eqn. (3.18) (defined in terms of velocity fluctuation u_i') denotes the effect of the unresolved turbulent scales on the resolved mean component. Given that velocity fluctuations are not accessible in RANS (i.e. are not computed explicitly), the Reynolds stress is modeled or closed using an eddy viscosity model as

$$-\langle u_i' u_j' \rangle = \mu_t \frac{\partial \langle u_i \rangle}{\partial x_j} \tag{3.19}$$

In this study the eddy viscosity is taken as

$$\mu_t = C_\mu \frac{k^2}{\varepsilon} \tag{3.20}$$

where k is the turbulent kinetic energy and ε is the turbulent kinetic energy dissipation rate. Transport equations for k and ε are specified via the classical k-ε model equipped with standard wall functions (Wilcox 1994).

The primary advantage of RANS is the relative low requirement on computer resources relative to DNS and LES given that RANS resolves the mean component of the flow only. Therefore, RANS has been successfully applied to simulation of high Reynolds number flow, such as flow around a full-scale airplane. However, RANS has two fatal drawbacks: 1) it only resolves the mean flow and thus results can be highly dependent on the turbulence (Reynolds stress) model; 2) no universal RANS turbulence model exists and thus a specific model may be needed for the particular flow problem.

3.2 Passive Tracer Transport

The basic technique used to conduct a tracer study is to introduce the tracer at the reactor inlet and measure the response at the outlet in terms of tracer concentration. A tracer is a conservative element, typically a dye or salt. The tracer is treated as a passive scalar which has no impact on hydraulic characteristics.

Two main approaches for the simulation of tracer transport are Lagrangian-based approach and Eulerian-based approach. The Lagrangian-based approach involving particle tracking has had successful applications (Stropky et al. 2007; Thyn et al. 1998; Wols et al. 2008a). However, it is less popular than the Eulerian-based approach of solving transport equation since common CFD codes are mainly based on Eulerian system. The Eulerian-based approach is used in the present dissertation.

3.2.1 Governing Equation for Passive Tracer Transport

For simulation of tracer transport in fluid flow, an advection-diffusion equation is used:

$$\frac{\partial C}{\partial t} + u_j \frac{\partial C}{\partial x_j} - \frac{\partial}{\partial x_j}\left(D_i \frac{\partial C}{\partial x_j}\right) = 0 \tag{3.21}$$

where u_i is the flow velocity, C is the tracer concentration, and D_i is the molecular diffusivity for the scalar.

Note that, solving the above advection-diffusion equation needs input of a known velocity field. There are two strategies to input the velocity field, namely frozen flow and dynamical flow:

- Frozen flow: Based on the assumptions of 1) steady flow and that 2) the tracer does not affect hydraulics, the flow is solved first; then the steady or 'frozen' flow is used to solve the advection-diffusion equation for tracer concentration.
- Dynamical flow: In this approach the flow equations and the advection-diffusion equation for scalar concentration are solved simultaneously at each time step of the discretization.

As noted in Chapter 2, the first strategy fits within the RANS methodology as RANS can solve for the mean (steady state) component of the flow field (Kim et al. 2010a; Hofman et al. 2007a; Huang et al. 2004). LES is only compatible with the second strategy because it resolves (solves for) the more energetic, larger turbulent scales in the flow which are all inherently unsteady.

3.2.2 RANS Methodology for Passive Tracer Transport

In the frozen flow strategy, the first step is to obtain a steady-state flow solution from the RANS Eqns. in (3.17) and (3.18); the next step is to use this flow solution to advect the passive

scalar (tracer) following the Reynolds-averaged advection-diffusion equation for tracer concentration:

$$\frac{\partial\langle C\rangle}{\partial t}+\langle u_j\rangle\frac{\partial\langle C\rangle}{\partial x_j}=-\frac{\partial\langle u_i'C'\rangle}{\partial x_j} \tag{3.22}$$

where $\langle C\rangle$ is the Reynolds-averaged or mean tracer concentration, C' denotes concentration fluctuation and turbulent scalar flux $-\langle u_j'C'\rangle$ is modeled as

$$-\langle u_i'C'\rangle=D_t\frac{\partial\langle C\rangle}{\partial x_j} \tag{3.23}$$

Note that $\langle C\rangle$ is time-dependent due to its transient boundary conditions described further below. The eddy (turbulent) diffusivity is taken as $D_t=\nu_t/Sc_t$ where eddy viscosity ν_t is computed via the *k*-ε model and the turbulent Schmidt number, Sc_t, is taken as 0.7 (Launder, 1978). In equation (3.22), molecular diffusion has been neglected as it is much less than turbulent diffusion throughout the flow domain.

3.2.3 LES Methodology for Passive Tracer Transport

The LES requires simultaneous solutions of the momentum and continuity equations for the flow and the advection-diffusion equation for tracer concentration at each time step, thereby capturing the impact of transient flow phenomenon on tracer transport, unlike in the previously described RANS.

In LES, transport of the tracer is simulated by solving the following advection-diffusion equation for the filtered tracer concentration, $\bar{C}$

$$\frac{\partial\bar{C}}{\partial t}+\bar{u}_j\frac{\partial\bar{C}}{\partial x_j}=\frac{\partial}{\partial x_j}\left(D_t'\frac{\partial\bar{C}}{\partial {x_j}^2}\right) \tag{3.24}$$

where D_t' is the SGS diffusivity, calculated as the ratio of SGS eddy viscosity (obtained from the dynamic Smagorinsky model in Eqn. (3.11)) to the LES turbulent Schmidt number. The LES

turbulent Schmidt number is set to 1,000 to keep the same ratio of molecular viscosity of water to the molecular diffusivity of the tracer used in the experiments by Kim et al. (2010a). The molecular diffusivity in Eqn. (3.24) has been neglected with respect to the SGS diffusivity D_t'.

3.2.4 Tracer Statistics

Tracer simulations (LES or RANS) are conducted by initially releasing a tracer pulse at the contactor inlet over roughly the first 2.5 second of the simulations. Tracer concentration at the contactor outlet is recorded in order to determine various diagnostics of the hydraulic efficiency (performance) of the contactor.

To characterize the results from numerical tracer transport simulations, the following quantities are defined.

1. Theoretical mean residence time τ:

$$\tau = \frac{volume\ of contactor}{flow\ rate} \tag{3.25}$$

2. Normalized time θ:

$$\theta = t/\tau \tag{3.26}$$

3. Normalized tracer concentration or residence time distribution (RTD) function:

$$E(\theta) = \frac{C}{\frac{C_{init} T_{release}}{\tau}} \tag{3.27}$$

where $T_{release}$ is the total time over which the tracer is released and τ is theoretical mean residence time and C is the simulated tracer concentration at the contactor outlet.

4. Cumulative residence time distribution function

$$F(\theta) = \int_0^{\theta} E(\theta)\, d\theta \tag{3.28}$$

5. The Morrill dispersion index (MDI) (Crittenden et al. 2005):

$$\text{MDI} = t_{90}/t_{10} \tag{3.29}$$

where, for example, t_{10} denotes the time it takes for 10% of the tracer to exit the contact. The MDI reflects the level of mixing in the contactors as well as the relative spread between t_{10} and t_{90}. In the case of ideal plug flow, the MDI has a value of 1.0.

6. A short-circuiting index (Persson, 2010) quantifying the intensity of short-circuiting is defined as

$$S = t_{16}/\tau \tag{3.30}$$

where t_{16} is the time it takes for 16% of the tracer to exit the contact. Note that the larger the S-value, the less intensive the short-circuiting. When S is 1.0, no short-circuiting exists and conditions correspond to an ideal plug flow reactor (PFR).

3.3 RANS Methodology for Ozonation Process

The simulation strategy for ozonation process (this section) and inactivation process (next section) considered in this work is based on RANS only and not LES. The reason for this is that the ozonation process considered here corresponds to the full-scale ozone contactor managed by the City of Tampa Water Department for which LES is not possible given the computational demands of LES.

3.3.1 Governing Equations for Ozonation Process

The governing equations for the chemical species transport and reaction in ozonation are the Reynolds-averaged species transport equations

$$\frac{\partial\langle C_i\rangle}{\partial t} + \langle u_j\rangle\frac{\partial\langle C_i\rangle}{\partial x_j} - \frac{\partial}{\partial x_j}\left(D_t\frac{\partial\langle C_i\rangle}{\partial x_j}\right) = \langle S_{C_i}\rangle \tag{3.31}$$

where $\langle C_i\rangle$ is the Reynolds-averaged (mean) concentration of chemical species *i*. $\langle S_{C_i}\rangle$ is the Reynolds-averaged chemical reaction source term for chemical species *i*. Here chemical reactions are taken to be second order where in general the nonlinearity of the reaction increases the difficulty of evaluating the chemical reaction source term. For example, take the following elementary reaction between species *A* and *B* yielding species *D*:

$$A + B \overset{k}{\rightarrow} D \tag{3.32}$$

The Reynolds-averaged chemical reaction source term for chemical species *D* would be (Fox, 2003)

$$\langle S_{C_D}\rangle = -k\{\langle A\rangle\langle B\rangle + \langle A'B'\rangle\} \tag{3.33}$$

where k is a second-order rate constant; $\langle A\rangle$ and A' are mean and fluctuation of the concentration of chemical species *A* respectively.

The term $\langle A'B'\rangle$ in Eq. (3.33) must be modeled or closed since A' and B' are fluctuations that are not accessible in RANS. The approach for modeling the term $\langle A'B'\rangle$ will be described in section 3.3.3.

To model the reactions in the City of Tampa Water Department ozone contactor (Chapter 5), a reduced reaction system is firstly selected to determine the reaction source terms of the form (3.33) for the species transport equations. Then, chemical time scales of this reaction system are analyzed so that the closure method for terms of the form $\langle A'B'\rangle$ in Eqn. (3.33) can be selected. The reduced reaction system is described next followed by the chemical time scales.

3.3.2 Modeling of Chemical Reactions

3.3.2.1 Components of the Reaction System and Individual Reaction Kinetics

Bromate formation, a by-product of the ozonation process, may involve numerous reactions. However, some reactions are not likely to occur due to relative low kinetics or weak possibility of reactant formation. A commonly used simplified reaction system for bromate formation (Mandel et al. 2012; Mandel 2010) includes two pathways: the molecular and radical pathways, outlined in Figure 3.1. As seen in Figure 3.1, only the molecular pathway is considered here for reasons stated next. Alkalinity, pH and natural organic matter (NOM) or total organic carbon (TOC) are the main factors that affect bromate formation in the present study. It has been reported that when pH is lower than 7, as it is in the current case (pH = 6.4), the dissolved ozone does not react with water and exists in molecular ozone form only (Zhang 2006). And decreasing pH would decrease the rate of hydroxyl radical formation and consequently depress the radical pathway of bromate formation (von Gunten and Pinkernll 2000). Alkalinity species, such as carbonate and bicarbonate ions present in the current system can scavenge hydroxyl radicals and consequently inhibit the radical pathway of bromate formation (Fabian 1995). Natural organic matter or NOM which is also present in the current system is another scavenger of hydroxyl radicals. The presence of NOM inhibits bromate formation especially during the initial period of ozonation (Song 1996).

Thus, in this dissertation, the reaction system includes ozone self-decomposition, the reaction between ozone and total organic carbon or TOC, and bromate formation. The bromate formation pathway used in this study is the molecular pathway, shown in Figure 3.1. The reaction system employed in the present study based on this molecular pathway includes 6 species and 6 reactions. The 6 species are dissolved ozone (O_3), TOC, bromide (B_r^-),

hypobromite (B_rO^-), bromite ($B_rO_2^-$), and bromate ($B_rO_3^-$). The 6 reactions are listed in Table 3.1 (Note that, '[ ]' means concentration of species). Based on this table, the source terms for each chemical species can be written as

$$\langle S_{O_3} \rangle = -k_d \langle [O_3] \rangle - k_{[TOC]} \langle [TOC][O_3] \rangle - k_1 \langle [B_r^-][O_3] \rangle - k_2 \langle [B_rO^-][O_3] \rangle$$
$$- k_3 \langle [B_rO^-][O_3] \rangle - k_4 \langle [B_rO_2^-][O_3] \rangle$$
$$\langle S_{[TOC]} \rangle = -k_{[TOC]} \langle [TOC][O_3] \rangle$$
$$\langle S_{B_r^-} \rangle = -k_1 \langle [B_r^-][O_3] \rangle + k_2 \langle [B_rO^-][O_3] \rangle \quad (3.34)$$
$$\langle S_{B_rO^-} \rangle = k_1 \langle [B_r^-][O_3] \rangle - k_2 \langle [B_rO^-][O_3] \rangle - k_3 \langle [B_rO^-][O_3] \rangle$$
$$\langle S_{B_rO_2^-} \rangle = k_3 \langle [B_rO^-][O_3] \rangle - k_4 \langle [B_rO_2^-][O_3] \rangle$$
$$\langle S_{B_rO_3^-} \rangle = k_4 \langle [B_rO_2^-][O_3] \rangle$$

The reaction rate constants are obtained from the literature and are listed in Table 3.2.

Note that this is the first time a reaction model as in (3.34) (involving kinetics-based modeling for bromate formation) has been used in CFD and validated using physical experimental data.

3.3.2.2 Effective Reaction Rate Constants

As found by Haag and Holgne (1983), the observed rate of B_r^- loss in its reaction with O_3 (see Table 3.2) is 1.5 to 3 times lower than that given by $-k_1 \langle [B_r^-][O_3] \rangle$ in Eq. (3.34). The explanation given for this is that the transfer of O_3 from gas phase to aqueous phase is the limiting step in bromate formation (Haag and Holgne 1983). To incorporate the limiting of the inter-phase transfer of O_3 into the present framework, effective reaction rate constants are employed. A general expression for effective reaction rate constants, k_i^{eff}, is

$$k_i{}^{eff} = \begin{cases} \dfrac{k_L a}{\langle [O_3] \rangle}, & \text{If } k_i \langle [O_3] \rangle > k_L a \\ k_i, & \text{If } k_i \langle [O_3] \rangle \leq k_L a \end{cases} \quad i = 1,2,3,4, TOC \tag{3.35}$$

where $k_L a$ is the overall mass transfer constant.

The value of $k_L a$ used in the present study is 3.92×10^{-4} s^{-1} (Talvy et al. 2011; Bartrand 2006). Although hypobromous acid (HOB_r) formation was not considered in the reaction model since it is not a concern of the present study, it is necessary to consider the competition between HOB_r and bromate ($B_r O_3^-$) for available hypobromite ($B_r O^-$). Thus the amount of $B_r O^-$ available for $B_r O_3^-$ formation is uncertain. In the present study, due to lack of data, the equilibrium concentration of $B_r O^-$ in a HOB_r solution at pH 6.5 (Haag and Holgne 1983) was used to estimate the percentage of $B_r O^-$ for bromate formation, $p_{B_r O^-}$, as 14%.

By applying the effective reaction rate constants and the $B_r O^-$ percentage assumption, the source terms can be re-written as:

$$\begin{aligned}
\langle S_{O_3} \rangle &= -k_d \langle [O_3] \rangle - k_{[TOC]}^{eff} \langle [TOC][O_3] \rangle - k_1^{eff} \langle [B_r^-][O_3] \rangle - k_2^{eff} \langle [B_r O^-][O_3] \rangle \\
&\quad - k_3^{eff} \langle [B_r O^-][O_3] \rangle - k_4^{eff} \langle [B_r O_2^-][O_3] \rangle \\
\langle S_{[TOC]} \rangle &= -k_{[TOC]}^{eff} \langle [TOC][O_3] \rangle \\
\langle S_{B_r^-} \rangle &= -k_1^{eff} \langle [B_r^-][O_3] \rangle + k_2^{eff} \langle [B_r O^-][O_3] \rangle \\
\langle S_{B_r O^-} \rangle &= k_1^{eff} \langle [B_r^-][O_3] \rangle - k_2^{eff} \langle [B_r O^-][O_3] \rangle - k_3^{eff} \langle \left(p_{B_r O^-} [B_r O^-]\right)[O_3] \rangle \\
\langle S_{B_r O_2^-} \rangle &= k_3^{eff} \langle \left(p_{B_r O^-} [B_r O^-]\right)[O_3] \rangle - k_4^{eff} \langle [B_r O_2^-][O_3] \rangle \\
\langle S_{B_r O_3^-} \rangle &= k_4^{eff} \langle [B_r O_2^-][O_3] \rangle
\end{aligned} \tag{3.36}$$

3.3.3 Chemical Time Scale Analysis and Closure for Source Terms

According to Fox (2003), the chemical time scales are defined in terms of the eigenvalues of the *Jacobian matrix* of the chemical source terms. In the present study, the *Jacobian matrix* of the chemical source terms is

$$\mathbf{J} = \frac{d\langle S_i \rangle}{d\langle C_j \rangle} \tag{3.37}$$

$$= \begin{bmatrix} -k_d - k_{[TOC]}\langle[TOC]\rangle - k_1\langle[B_r^-]\rangle - k_2\langle[B_rO^-]\rangle - k_3\langle[B_rO^-]\rangle - k_4\langle[B_rO_2^-]\rangle & -k_{[TOC]}\langle[O_3]\rangle & -k_1\langle[O_3]\rangle & -k_2\langle[O_3]\rangle - k_3\langle[O_3]\rangle & -k_4\langle[O_3]\rangle & 0 \\ -k_{[TOC]}\langle[TOC]\rangle & -k_{[TOC]}\langle[O_3]\rangle & 0 & 0 & 0 & 0 \\ -k_1\langle[B_r^-]\rangle + k_2\langle[B_rO^-]\rangle & 0 & -k_1\langle[O_3]\rangle & k_2\langle[O_3]\rangle & 0 & 0 \\ k_1\langle[B_r^-]\rangle - k_2\langle[B_rO^-]\rangle - k_3\langle[B_rO^-]\rangle & 0 & k_1\langle[O_3]\rangle & -k_2\langle[O_3]\rangle - k_3\langle[O_3]\rangle & 0 & 0 \\ k_3\langle[B_rO^-]\rangle - k_4\langle[B_rO_2^-]\rangle & 0 & 0 & k_3\langle[O_3]\rangle & -k_4\langle[O_3]\rangle & 0 \\ k_4\langle[B_rO_2^-]\rangle & 0 & 0 & 0 & k_4\langle[O_3]\rangle & 0 \end{bmatrix}$$

The chemical time scales, τ_α, are defined as

$$\tau_\alpha \equiv \frac{1}{|\mu_\alpha|} \tag{3.38}$$

where μ_α are the eigenvalues of the *Jacobian matrix*. A fast reaction corresponds to large eigenvalues and small chemical time scales while slow reaction corresponds to small eigenvalues and large chemical time scales. In a complex reaction system, the chemical time scales can range over multiple orders of magnitude.

The micro-mixing time scale determines the category of reaction system. According to Baldyga and Pohorecki (1995) micro-mixing "consists of the viscous-convective deformation of fluid elements, followed by molecular diffusion." Thus in this dissertation, the Kolmogorov time scale is employed to represent the micro-mixing time scale. As noted in Chapter 3, the Kolmogorov micro-scales (Pope, 2000) correspond to the smallest scales of the turbulence spectrum and is where mechanical energy is dissipated into heat. The Kolmogorov time scale t_K (Pope, 2000) is calculated as

$$t_K \equiv \left(\frac{\nu}{\varepsilon}\right)^{1/2} \tag{3.39}$$

where ν is kinematic viscosity and ε is the rate of dissipation of turbulent energy. Based on the ratio of micro-mixing time scale to chemical time scale, a reaction system can be categorized into three groups: slow chemistry (for which chemical time scales are larger than the micro-mixing time scale), fast chemistry (for which chemical time scales are smaller than the micro-mixing time scale), and finite-rate chemistry (see Figure 3.2). A closure method for the co-variance in equation (3.33) term, $\langle A'B' \rangle$, or turbulence-chemistry interaction needs to be properly based on the category of the reaction system. The reaction system studied in this dissertation will be taken to be slow chemistry, as will be discussed in section 5.3. Thus, the mixing is considered fast enough that the composition of variables, $\langle AB \rangle$, can be approximated by their mean values $\langle A \rangle \langle B \rangle$, and thus $\langle A'B' \rangle = 0$ in (3.33). In other words, the means of products between concentration species in Eq. (3.36) may be replaced with products between mean concentrations.

3.4 Governing Equations for Inactivation Process

The governing equations for inactivation are described here within the context of RANS, for the same reason explained earlier in the case of the ozonation process.

3.4.1 Kinetics-based Inactivation

In kinetics-based inactivation, the governing equation for the inactivation of microorganisms m is a transport equation for the concentration of microorganisms, N_m, expressed as

$$\frac{\partial N_m}{\partial t} + u_j \frac{\partial N_m}{\partial x_j} - \frac{\partial}{\partial x_j}\left(D_i \frac{\partial N_m}{\partial x_j} \right) = S_{N_m} \tag{3.40}$$

where N_m is the concentration of microorganism m and S_{N_m} is an external volumetric source term for microorganism m. The Hom-Haas model and Chick-Watson model which have been introduced in section 2.2.4 can be used to estimate this source term. However, kinetics-based inactivation is not possible in the present study due to lack of experimental physical data needed,

for example, to set initial conditions for Eqn. (3.40). Thus, kinetics-based inactivation is not used in the present study.

3.4.2 CT-based Inactivation

The concentration-contact time (CT) concept has been commonly employed to evaluate disinfection effectiveness (U.S. EPA 2003; Zhang 2006; Wols et al. 2010a).

The CT concept is expressed as a product of the average concentration of disinfectant (i.e. ozone) multiplied by the time over which an organism is exposed to the disinfectant (U.S. EPA 2003). This product is referred to as CT and typically has the unit min-mg/liter. A large CT value means the possibility of an organism being inactivated or the portion of organisms being inactivated is high. The mean CT can be obtained by solving the following Reynolds-averaged transport equation (Zhang, 2006):

$$\frac{\partial\langle CT\rangle}{\partial t}+\langle u_j\rangle\frac{\partial\langle CT\rangle}{\partial x_j}-D_t\frac{\partial}{\partial x_j}\left(\frac{\partial\langle CT\rangle}{\partial x_j}\right)=\langle S_{CT}\rangle \tag{3.41}$$

The source term for CT is defined as

$$\langle S_{CT}\rangle=\langle C_l\rangle \tag{3.42}$$

where $\langle C_l\rangle$ is the Reynolds-averaged concentration of dissolved ozone.

3.5 Numerical Tool

The computational tool used to solve the framework nonlinear partial differential equations is the open source numerical library OpenFOAM (2010), an acronym for Open source Field Operations and Manipulations. OpenFOAM is a collection of C++ libraries, designed for solving continuum mechanics problems.

OpenFOAM uses the finite volume method to discretize the governing flow and scalar transport equations. Pressure-velocity coupling is accomplished using the well-known SIMPLE

(Semi-Implicit Method for Pressure Linked Equations) method for RANS equations and the well-known PISO (Pressure Implicit with Splitting of Operators) method for LES equations. The non-linear advection terms are discretized with a second order accurate upwind scheme and diffusion terms are discretized with a central finite difference scheme. Time integration for the tracer concentration consists of the first order accurate Euler method.

3.6 Chapter Summary

In this chapter, strategies and models for each sub-process (or stage) of ozone disinfection are presented. A modeling framework for ozone disinfection combining CFD with a kinetics-based reaction model for bromate formation has been developed for the first time. This modeling framework will be validated in Chapter 5 via application to a full-scale ozone contactor.

The framework components used in the following chapters vary depending on the objectives. A summary of the framework components used in each chapter is given in Table 3.3. In Chapter 4, both RANS and LES are used for flow and tracer transport simulations of laboratory-scale baffled and column contactors. In Chapter 5, flow, tracer transport, reaction, and inactivation RANS simulations are conducted for the full-scale ozone contactor operated by the City of Tampa Water Department. In Chapter 6, flow and tracer transport simulations are conducted using RANS for additional applications. In appendix B, LES and DNS and are conducted of a popular channel flow problem for the purpose of validating the numerical methods in OpenFOAM.

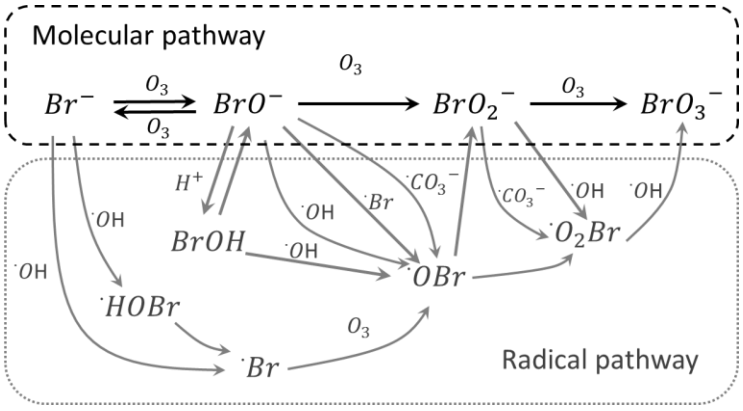

Figure 3.1: The pathways of bromate formation (the molecular pathway in black color was used in the present study).

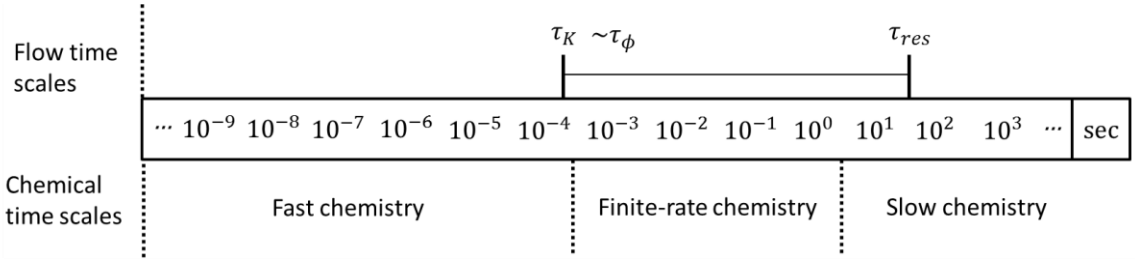

Figure 3.2: Categorization of a reaction system based on the ratio of chemical time scales to flow time scales (adapted from Fox (2003)). Note that, τ_K is Kolmogorov time scale, τ_ϕ is micro-mixing time scale, and τ_{res} is theoretical residence time scale.

Table 3.1: The reactions considered in the present modeling framework.

Reaction	Reaction expression	Reaction rate expression	Reference
Ozone self-decomposition	$2O_3 \overset{k_d}{\rightarrow} 3O_2$	$r_{[O_3]} = -k_d[O_3]$	Wols (2010); Zhang (2006, 2007)
TOC	$O_3 + TOC \overset{k_{[TOC]}}{\longrightarrow} O_2 + product$	$r_{[TOC]} = -k_{[TOC]}[TOC][O_3]$	Kim et al. (2007)
Bromide	$Br^- + O_3 \overset{k_1}{\rightarrow} BrO^- + O_2$	$r_{[Br^-]} = -k_1[Br^-][O_3]$	Haag and Hoigne (1983)
Hypobromite	$BrO^- + O_3 \overset{k_2}{\rightarrow} Br^- + 2O_2$	$r_{[BrO^-]} = -k_2[BrO^-][O_3]$	Haag and Hoigne (1983)

Table 3.1 (Continued)

Reaction	Reaction expression	Reaction rate expression	Reference
Bromite	$B_rO^- + O_3 \xrightarrow{k_3} B_rO_2^- + O_2$	$r_{[B_rO^-]} = -k_3[B_rO^-][O_3]$	Haag and Hoigne (1983)
Bromate	$B_rO_2^- + O_3 \xrightarrow{k_4} B_rO_3^- + O_2$	$r_{[B_rO_2^-]} = -k_4[B_rO_2^-][O_3]$	Haag and Hoigne (1983)

Table 3.2: Reaction rate constants for the reaction system of ozone disinfection.

Reaction rate constant	Value (20 ˚C)	Source
$\boldsymbol{k_d}$	2.5×10^{-3} s^{-1}	Wols et al. (2010a); Zhang (2006, 2007)
$\boldsymbol{k_1}$	1.6×10^{2} $(Mole/L)^{-1}s^{-1}$	Haag and Hoigne (1983)
$\boldsymbol{k_2}$	3.3×10^{2} $(Mole/L)^{-1}s^{-1}$	Haag and Hoigne (1983)
$\boldsymbol{k_3}$	1.0×10^{2} $(Mole/L)^{-1}s^{-1}$	Haag and Hoigne (1983)
$\boldsymbol{k_4}$	4.6×10^{4} $(Mole/L)^{-1}s^{-1}$	Mandel et al. (2012)
$\boldsymbol{k_{[TOC]}}$	3.8×10^{4} $(Mole/L)^{-1}s^{-1}$	Kim et al. (2007)

Table 3.3: Methodologies used in the present study.

	Flow simulation			**Tracer transport simulation**		**Reaction simulation**		**Inactivation based on CT concept**	
	RANS	**LES**	**DNS**	**RANS**	**LES**	**RANS**	**LES**	**RANS**	**LES**
Chapter 4	√	√		√	√				
Chapter 5	√			√		√		√	
Chapter 6	√			√					
Appendix B		√	√						

CHAPTER 4: EVALUATION OF COMPUATIONAL FRAMEWORK FOR DETERMINING HYDRAULIC PERFORMANCE OF CONTACTORS[1]

4.1 Introduction

As described in detail Section 3.1, how to treat turbulence is a primary challenge for CFD. DNS is the most straight forward approach for representing turbulent flow since it resolves all scales of the turbulence. However, DNS is often prohibitively cost-intensive in applications to realistic problems. RANS simulation resolves only the mean flow while modeling all of the scales of turbulence. Despite its low resolution, its cost-effectiveness makes it the most popular approach for industrial applications. LES is intermediate between DNS and RANS in terms of spatial resolution and thus computational cost. It resolves the more energetic turbulent scales while modeling the unresolved, less energetic smaller scales (Pope, 2000). Although it is cost-intensive, LES has been gaining popularity for realistic applications in aerospace engineering, ocean engineering, and mechanical engineering and so on, due to rapid development of computing power (Sagaut and Deck 2009; Georgiadis et al. 2009).

CFD for water treatment applications was not introduced until the late 1990s. As described in Section 2.3, applications of CFD have succeeded in trouble-shooting existing water treatment facilities and reducing the cost of process designs. CFD was firstly employed to study the flow in a disinfection reactor or contactor (Wang and Falconer 1998a, b). Then, it was used to simulate tracer transport in a reactor (Huang et al. 2004; Hofman et al. 2007a; Zhang et al.

[1] Part of Chapter 4 is reprinted from Journal of Environmental Engineering, 139(3), Jie Zhang, Andrés E. Tejada-Martínez, Qiong Zhang, RANS Simulation of the Flow and Tracer Transport in a Multi-chambered Ozone Contactor, 450-454, Copyright (2013), with permission from ASCE. Permission is included in Appendix D.

2013a, b; Amini et al. 2011; Kim et al. 2010a; Wols et al. 2008a). Note that, tracer transport is commonly used to evaluate the hydraulic performance of a chemical reactor or disinfection contactor. Researchers have also incorporated reaction processes into flow simulations in order to predict the removal of chemical or pathogens directly (Cockx et al. 1999; Huang et al. 2004; Zhang 2006; Bartrand 2006; Zhang et al. 2007; Bolaños et al. 2008; Wols et al. 2010a; Talvy et al. 2011). In Chapter 3 a CFD-based framework including a kinetics-based model for bromate formation in RANS simulation of the ozonation process in ozone contactors was developed. The flow and passive tracer simulation components of the framework are validated in this chapter via application to baffled and column contactors.

RANS has been the popular approach in CFD applications related to the water treatment industry since its very first application. However, recently, Kim et al. (2010b) presented results showing that RANS may perform poorly in predicting important design indices in tracer transport simulations, such as the t_{10} index (defined as the time it takes for ten percent of an inflowing tracer to exit the disinfection system). LES was shown to perform much better. In section 4.2, steady state RANS of the ozone contactor flow of Kim et al. (2010a) with flow domain and computational grid similar to those used in their study in which wall and baffle viscous sub-layers were well-resolved is revisited. Additional RANS simulations are made on significantly coarser grids in order to analyze the impact of grid resolution on the flow structure and tracer residence time. Such analysis is lacking in the literature and its merit lies in the fact that RANS has previously been applied to full-scale ozone contactors in which wall and baffle viscous sub-layers are not resolved (e.g. see Do-Quang et al. 1999; Cockx et al. 1999; Huang et al. 2004; Zhang et al. 2007). Thus, understanding how RANS flow and tracer solutions behave when these molecular sub-layers are poorly resolved or not resolved at all is important.

Furthermore, there is a need to re-visit the RANS of Kim et al. (2010a) in light of the discrepancies between their computations and laboratory experiments in terms of cumulative RTD and the more favorable comparisons reported by other researchers (e.g. Do-Quang et al. 1999; Cockx et al. 1999; Zhang et al. 2007).

The tracer or chemical species transport in water treatment facilities is a turbulent process which in principle should be better predicted by LES rather than by RANS since LES has the capability of resolving important turbulent scales not captured (and instead modeled) in RANS. Thus, studies are also conducted in order to identify in which flow configurations and for which desirable predicted quantities LES is a better choice than RANS.

4.2 The Impact of RANS Turbulence Model and Grid on Hydraulic Performance Prediction for a Baffled Ozone Contactor

In order to assess the impact of RANS turbulence model and grid resolution on flow and tracer transport, RANS simulations of a laboratory-scale baffled contactor were performed. Results are compared with those from LES in terms of flow and residence time statistics.

4.2.1 Flow Domain and Boundary Conditions

The RANS and LES methodologies used in this study have been introduced in Sections 3.1 and 3.2. The flow configuration consists of the laboratory-scale, baffled ozone contactor section in Figure 4.1. The laboratory-scale contactor of Kim et al. (2010b) consisted of 12 chambers. A truncated version consisting of 4 chambers was considered in the computations of Kim et al. (2010a) and is also considered for the present studies. The section formed by the 4 chambers (chamber width is 0.113m) is 0.48m long in the inflow (x_1) direction and 0.23m wide in the span-wise (x_3) direction. The rest of the dimensions of the contactor including the dimensions of the baffles are given in Figure 4.1. The water extends a distance of 0.21m above

the bottom and does not fill the entire contactor. Thus, a zero-shear stress with zero normal flow boundary condition is imposed at the surface. No-slip conditions are imposed at the bottom and baffle walls and the inlet and outlet are periodic for velocity and pressure. The Reynolds number based on hydraulic diameter ($h_R = \sqrt{4A_c/\pi}$, where A_c is the cross-section area at the periodic inlet) and bulk inlet velocity, U_{bulk}, is 2740. This corresponds to the same Reynolds number as in the computations and laboratory experiment of Kim et al. (2010a, b). This Reynolds number value was achieved by dynamically adjusting the streamwise body force in the momentum equation (see Eqn. B.1 for example) in both RANS and LES via Eqn. B.2.

RANS flow simulations were started from rest. Once the steady state RANS solution of the flow was obtained, the scalar advection-diffusion transport equation for the passive tracer was solved using the steady state RANS velocity. The tracer study was conducted by initially releasing a tracer pulse of Reynolds-averaged concentration $\langle C \rangle = 1$ at the inlet over the first 2.5 seconds of the tracer simulation. The normal gradient of $\langle C \rangle$ was set to zero at the outlet and at the walls, indicative of zero diffusive flux across these boundaries.

LES simulations for the flow were also started from rest and continued until a statistically steady state had been reached (i.e. until time-averaged velocity fields became independent of averaging window size). Once a statistically steady state was reached, simultaneous solution of the LES tracer transport equation was initiated by releasing a tracer pulse of resolved tracer concentration $\bar{C} = 1$ at the inlet over the first 2.5 seconds of the tracer solution. Zero diffusive flux was also set at the boundaries.

RANS simulations were performed on several structured grids in order to determine the grid dependence of results. Figures 4.2a, b show two of the grids used. The finest grid consists of 1,455,073 total grid points (208×101×83 in x_1-x_2-x_3 (x-y-z) directions, respectively) (grid A) and

the coarsest grid consists of 1864 total grid points (28×10×8) (grid D). Grids B and C consist of (108×41×35) and (52×21×17) points, respectively. LES was performed on the (208×101×83) grid (grid A). The grids are refined at bottom and at baffle walls in order to resolve steep velocity gradients. Note that the grid region close to the water surface is coarser than near wall boundaries due to smaller gradients there. For the finest grids (grids A and B), at the bottom and baffle walls, the grid is refined such that the distance between the first grid point and the bottom or baffle wall in plus units (y_1^+) is less than 11, thereby resolving the buffer zones and viscous sub-layers adjacent to these boundaries (see (Pope 2000) for more details about these sublayers characteristic of classical wall-bounded turbulent boundary layers). Distance y_1^+ is defined as $y_1^+ = (d/\nu)\sqrt{\tau_w/\rho}$ with $\tau_w = \mu V_1/d$ where τ_w is the wall shear stress, d is the distance of the first grid point off the wall and V_1 is the time averaged flow speed at the first grid point off the wall. In grids A (the finest grid), B, C and D (the coarsest grid) the maximum value of y_1^+ is approximately 2, 7, 15 and 23 for the baffle and bottom walls, respectively.

As mentioned above, in all RANS simulations the flow was started from rest and integrated (or iterated) until a steady state solution was reached. Solutions were deemed steady state once the momentum and continuity equation residuals reached certain threshold values and velocity profiles did not show significant changes (less than 1 percent) from iteration to iteration. At the end of iterations on all grids, the cumulative continuity equation residual was on the order of 1e-19. At the end of iterations on grids A-C, momentum equation residuals were all of order 1e-5 or less. On grid D, momentum equation residuals were all of order 1e-4 or less. Error residuals are defined by Jasak (1996).

4.2.2 Results and Discussions

Figure 4.3 shows absolute velocity (i.e. speed) superimposed with streamlines from RANS and LES performed with grid A. Absolute velocity and streamlines are shown for the streamwise-vertical (x_1-x_2) plane at mid span (at $x_3 = L/2$ where L is the spanwise length of the domain). Both RANS and LES solutions are characterized by an undulating, high-speed core jet extending from chamber to chamber and a secondary, slower-speed re-circulation zone within each chamber. The key difference between the two simulations is that RANS is not able to capture smaller scales eddies present near the entrance of each chamber, as revealed by the LES.

In Figure 4.4, profiles of the RANS x_2- or y-component of velocity versus chamber width along x_1 (x) are plotted at different depths. Figure 4.4 also shows corresponding profiles from the LES for which LES velocity fields have been time-averaged. In all of the RANS simulations with the different grids, the y-velocity vector changes direction from negative y to positive y along the chamber width, in accordance with the presence of the re-circulation zone occupying a large part of the chamber, seen in Figure 4.3. The LES profile exhibits a similar but more complicated behavior in which the y-component of velocity also changes sign near the walls at the chamber entrance (Figure 4.4a). This is due to small scale eddies resolved in LES and unresolved in RANS, seen in Figure 4.3.

For all RANS simulations on the different grids, locations of elevated tracer concentrations were found at the baffle walls and near the surface (not shown), in agreement with the LES and experiments of Kim et al. (2010a, 2010b). Furthermore, all simulations exhibited the effect of short-circuiting evidenced by tracer detection at the outlet at a time much shorter than expected (from a plug flow condition).

Figure 4.5 shows tracer RTD versus time for RANS solutions on various grids. Note that time, *t*, is normalized by the theoretical mean residence time, $\tau = 109.2$ s. Theoretical mean residence time assumes a perfectly mixed reactor and thus is computed as $\tau = V/Q$ where V is the volume of the contactor and Q is the volumetric flow rate. Tracer RTDs computed are characterized by primary and secondary peaks, indicating strong internal circulation. The intensity of peaks and troughs is affected by a combination of dispersion and short-circuiting. Furthermore, the peaks and troughs in the RTDs obtained using grids B, C and D (i.e. the coarser grids) are shifted to the left with respect to the RTD obtained with grid A (i.e. the finest grid). The shift of the peaks to the left means that short-circuiting in the simulations with the coarser grids is stronger than the short-circuiting in the simulation with the finest grid (grid A). Figure 4.5 also includes RTD curves obtained in the RANS of Kim et al. (2010a) and in the laboratory experiment of Kim et al. (2010b). Notice that the primary peak in the experimental RTD is significantly lower than the primary peak in the computations. Differences in statistics such as mean residence time (discussed further below) and cumulative RTD (in Fig. 4.6) are less pronounced due to the time integration required to compute these quantities. Finally, note that the RTD curve from the RANS of Kim et al. (2010a) is characterized by several peaks, inconsistent with the bimodal behavior exhibited by the RTD from the laboratory experiment and the present RANS.

Mean residence time obtained from RANS with different grids is as follows: grid A: 110.33 s, grid B: 109.90 s, grid C: 107.20 s, grid D: 112.99 s. Mean residence times were obtained via integration of RTD curves from t=0 through t=327.6 s = 3θ, where θ is time normalized by theoretical mean residence time (τ = 109.2 s). The mean residence times are

within 3% of each other, except for the difference between mean residence times on grid C and grid D which is 5.4%.

Figure 4.6 compares the cumulative RTD obtained in the present RANS on different grids with the cumulative RTD obtained in the experiments of Kim et al. (2010b) and in the RANS of Kim et al. (2010a). Cumulative RTDs predicted by the present RANS simulations on grids of varying resolution are all in much better agreement with the cumulative RTD in the experiment of Kim et al. (2010b) than the cumulative RTD in the RANS of Kim et al. (2010b). The LES of Kim et al. (2010a) led to excellent agreement with the experimental data, however, a RANS using the same grid as the LES did not perform as well (see the Kim et al. RANS data included in our Figure 4.6).

When the tracer is released into the contactor, the portion of the tracer initially within the high-speed core jet flow (see Figure 4.3) exits rapidly. The rest of the tracer remains in the contactor for longer times as it becomes trapped within large-scale eddies serving as dead zones or retention zones in each chamber. As time progresses, the tracer within these retention zones diffuses or spreads out and is ultimately carried out of the contactor by the core jet. Grid density impacts cumulative RTD as can be seen for example by comparing curves obtained with grids C and D in Figure 4.6. Grid D under-predicts the cumulative RTD due to the fact that this grid leads to lower speeds within the core jet of the flow (see Figure 4.4). These lower speeds also lead to smaller wall-normal velocity gradients and thus smaller eddy viscosity values, ultimately leading to a slower turbulent diffusion rate. Both of these factors are responsible for the under-prediction of cumulative RTD in RANS on grid D compared to grid C.

The t_{10} index (associated with the cumulative RTD (as marked in Figure 4.6) and more specifically serving to denote the time for 10% of the tracer to exit the contactor) is primarily

controlled by the speed of the flow in the core jet. The effect of grid density on t_{10} can be seen by comparing results with grids D and C in Table 4.1 and Figure 4.4. RANS on grid D (the coarsest of the grids) under-predicts the velocity in the core jet relative to RANS on grid C (e.g. see core jet velocities at x/W ~ 0.1 and x/W ~ 0.9 in Fig. 4), thereby leading to an over-prediction of t_{10} characterized by a 13.5% error with respect to the experimental value of Kim et al. (2010b). The greater resolution of grid C leads to a more accurate prediction of t_{10} with a 3.6% error.

Note that RANS on grids A and B lead to higher errors in t_{10} than the RANS on grid C. The reason for this is that grids A and B resolve down to the buffer zone and viscous sublayer close to the walls, however the k-ε turbulence model with standard wall functions used (see description in sub-section 3.1.3) is not equipped to give physically meaningful predictions of the eddy viscosity within these layers. The k-ε model with standard wall functions model calculates a non-zero eddy viscosity down to the log-layer and sets the eddy viscosity to zero at grid points within the buffer zone and viscous sublayer. This leads to a k-ε model with drastic different behaviors on grids A and B compared to grids C and D. To verify this we have also performed RANS on grids A and B with the Launder and Sharma k-ε model (Launder and Sharma, 1974; Patel et al. 1985), which is equipped to integrate the k-ε model equations down to the walls. Thus, this model provides physically meaningful eddy viscosity values within the buffer zone and the viscous sublayer leading to highly accurate predictions of t_{10} characterized by 0.6% and 1.8% relative errors on grids A and B, respectively. The model of Launder and Sharma is readily available in OpenFOAM.

4.2.3 Conclusions

LES predicts the existence of smaller scale eddies near the entrance of each chamber. These eddies are not present in any of the RANS simulations, even when the finest grid used in

RANS is identical to the grid used in the LES. Tracer RTD was found to have some dependence on grid resolution due to varying predictions of short-circuiting and dispersion on the different grids. RANS on all grids employed led to cumulative RTD in excellent agreement with the experimental data of Kim et al. (2010b). Similar agreement between computations and physical experiments had been found by other researchers (e.g. Do-Quang et al. 1999; Cockx et al. 1999; Zhang et al. 2007).

Furthermore, the agreement with experimental cumulative RTD was shown to be much better than what had been previously reported by Kim et al. (2010a).

Predicted t_{10} index depends on grid density and RANS turbulence model. For fine grids that resolve the viscous sub-layer, such as grids A and B, the k-ε turbulence model equipped with standard wall functions (Wilcox 2004) leads to greater errors in predicted t_{10} compared with the prediction from LES of Kim et al. (2010b). The k-ε model of Launder and Sharma which is equipped to integrate the model equations down to the wall and thus properly handling the viscous sub-layer significantly improves the accuracy of predicted t_{10} as expected. This results in smaller errors compared with the LES prediction from Kim et al. (2010b). Predicted t_{10} index on all grids with proper turbulence model are within 13% error with respect to the experimental data.

It is concluded that RANS is able to predict t_{10} on par or better than the LES reported by Kim et al. (2010a). The reason why the RANS approach performs on par with the LES approach in predicting the cumulative RTD and associated indexes such as t_{10} may be attributed to the fact that RANS is able to resolve the large-scale eddies or retention zones within each chamber. In addition to these large-scale retention zones, the LES is also able to resolve smaller scale eddies not resolved by the RANS. These smaller eddies can retain parts of the tracer, however, parts of the tracer that are not captured by these eddies are simply left to be captured by the larger eddies

as is the case in RANS. Thus, as long as the large-scale eddies are resolved and the turbulent smaller eddies are accounted for through a turbulence model, resolution of the smaller scale eddies is not crucial for predicting the cumulative RTD to some level of accuracy, as evidenced by our RANS results. Note that all of the grids used are able to resolve the largest retention zones in each chamber (not shown). An important function of the smaller-scale eddies resolved by the LES is to provide turbulent diffusion. In RANS, turbulent diffusion provided by these unresolved smaller scale eddies is accounted for through the turbulence model, which in our case is taken as the *k*-ε model.

Overall, results reported here are encouraging, especially those obtained on the coarser grids, indicating that fine-scale simulation methodologies such as LES are not always needed for numerical RTD studies. The next sub-section will highlight flow cases for which RANS does not perform as well as LES.

4.3 What Can Be Gained from LES over RANS?

4.3.1 Flow Domains and Boundary Conditions

Results from RANS and LES simulations of flow and tracer transport in a column contactor and a baffled contactor are compared. The focus here is on the identification of unsteady flow features which play an important role in determining the hydraulic performance of contactors. Due to their unsteady nature, such features require LES over RANS for their accurate representation and ultimately for the accurate determination of the hydraulic performance.

The present numerical studies of flow and tracer transport in a column contactor are based on the physical pilot-scale experiments of Chen (1998). The pilot-scale ozone contactor is a 6.081 meter long glass column in the flow direction (x_3) with an internal diameter of 152 mm and an inlet/outlet diameter of 25.4 mm, shown in Figure 4.7. Two scenarios with different water

flow rates were considered. Scenario AI was with flow rate of 13.0 gpm or 8.2×10^{-4} m^3/s and scenario AII was with a flow rate of 2.6 gpm or 1.64×10^{-4} m^3/s. The corresponding Reynolds numbers ($Re = Qd/A_c\nu$, where Q is mean flow rate, d is diameter of the column contactor, A_c is the cross section area, and ν is viscosity of water) are 6,900 and 1,380 for scenarios AI and AII respectively. Physical experimental data from Chen (1998) is available for *Re* = 6,900.

The computational grid used in RANS consists of 32,890 (14×24×111) points while the grid used in LES consists of 235,200 (29×41×211) points, shown in Figure 4.7. Note that these grids are structured. A finer grid is used in the LES in order to resolve near-wall regions. Inlet velocity and outlet pressure are prescribed boundary conditions. No-slip velocity is prescribed at the walls.

Both RANS and LES tracer simulations were conducted by initially releasing a tracer pulse with concentration $C_{init} = 1$ at the inlet over a 2.0 and 10.0-second period for scenarios AI and AII, respectively. Note that different release time periods were needed to ensure that the same amount of mass of tracer was released into the reactor in all simulations. At the outlet and at the walls, the normal gradients of tracer concentration were set to zero indicating zero diffusive flux across these boundaries.

The configuration and boundary conditions of the baffled contactor studied in this section are the same as these in section 4.2. Two scenarios with different Reynolds numbers (2740 and 5480) were studied. Recall that the Reynolds number is based on the hydraulic diameter ($h_R = \sqrt{4A_c/\pi}$, where A_c is the cross section area at the inlet) and target bulk inlet velocity U_{bulk}. The Reynolds number in scenario BI (2740) corresponds to the Reynolds number in the laboratory experiment of Kim et al. (2010a) and in the computations of Kim et al. (2010b). As noted earlier, a dynamically adjusted body force in the x_1 direction was included in the momentum equation in

order to drive the flows and attain these Reynolds numbers. Details of this body force can be found in Appendix B.

The grid employed in RANS simulation has 18,564 ($52 \times 21 \times 17$) points which was one of the coarsest grids studied in section 4.2 and for which the standard k-ε turbulence model worked well. The grid employed in the LES simulation has 1,743,664 ($208 \times 101 \times 83$) points, shown in Figure 4.8(b). A much finer grid is used in LES simulation in order to resolve near-wall regions.

The numerical tracer transport simulation was conducted by initially releasing a tracer pulse with concentration $C_{init} = 1$ at the inlet over a 2.5 and 1.25-second period for scenarios BI and BII considered, respectively. At the outlet and at the walls, the normal gradients of tracer concentration were set to zero indicating zero diffusive flux across these boundaries.

A summary of the configurations for column and baffled contactors studied is given in Table 4.2.

4.3.2 Results and Discussion

Figure 4.9 shows normalized tracer concentration at contactor outlet versus normalized time (i.e. RTD) for the column contactor flow at *Re* = 6900 (scenario AI). The RTD predicted by RANS for the column contactor greatly differs from the physical experimental data (Figure 4.9). The concentration peak predicted by RANS is delayed and has a higher value than the experimental data. The prediction by LES agrees better with the experimental data especially in terms of concentration peak location. To further explore this difference between RANS and LES predictions, characteristic residence times from the present numerical simulations and physical experiments of Chen (1998) are estimated from the RTD curves and listed in Table 4.3. In this table, T_1 denotes the time it takes for the amount of tracer at the outlet to reach 1% of the amount

of tracer injected at the inlet. T_{peak} denotes the time at which the peak RTD occurs in Figure 4.9. T_1 and T_{peak} predicted by LES are much closer to the experimental data than those predicted by RANS. Note that, a minor discrepancy still exists between the peak values of tracer concentration from LES and physical experiment. This is potentially caused by the fact that a counter gas-phase flow occurred in the physical experiment while this was not the case in the simulation.

Next, flow fields are examined in order to understand the discrepancy in RTD curves between LES and RANS. Based on Figure 4.10, it is seen that relative to LES, RANS is not able to accurately represent the spatial transition to turbulence induced by the inlet jet. RANS predicts a transition to fully developed turbulence within approximately 0.5 meters from the inlet. Meanwhile, in LES this transition occurs over a much greater distance of approximately 2 meters. Note that the LES is able to resolve the spatial instability of the inlet jet leading to its break-down and subsequent transition to fully developed turbulence. Such breakdown of the jet and transition to turbulence is not captured in RANS. The spatial breakdown is seen in Figure 4.10a as well as in Figure 4.11. In Figure 4.11, the breakdown of the jet in the LES gives rise to instantaneous, localized spikes in the downstream velocity in regions away from the centerline of the contactor.

Due to the shorter distance for transition to fully developed turbulence predicted by RANS, this methodology over-predicts turbulent mixing of momentum over the length of the contactor compared to LES (see time-averaged LES velocity profiles compared to RANS velocity profiles in Figure 4.11). For example, at 5m from the inlet, the RANS mean velocity is flatter bringing fluid with greater speed closer to the wall relative to the LES prediction. This leads the RTD peak to occur at a later time in the RANS, as seen in earlier in Figure 4.9.

Figure 4.12 shows RTD curves for flows under scenarios AI and AII (Re = 6900 and Re = 1380, respectively). A similar difference between LES and RANS-predicted RTD is observed at Re = 1380 as was observed at Re = 6900. The difference can be once again traced to LES resolution of the breakdown of the inlet jet and spatial transition to fully developed turbulence which is absent in RANS (see Figure 4.13).

Figure 4.14 shows cumulative RTD curves computed from the RTD curves in Figures 4.9 and 4.12. Cumulative RTD is useful for measuring characteristic residence times such as t_{10}. The Morrill dispersion index or MDI (defined as t_{90}/t_{10}, see sub-section 3.2.4, Eqn. 3.29) is also calculated from the characteristic residence time indices. Recall that the MDI is equal to 1 for an ideal flow reactor. Due to over-prediction of turbulent mixing and consequently under-prediction of the intensity of short-circuiting, RANS consistently under-predicts the MDI with respect to LES, as can be seen from Table 4.4. In other words, the RANS yields a flow closer to plug flow due to excessive unphysical mixing.

Next, results from LES and RANS of flow and tracer transport in the baffled contactor are presented. Figure 4.15 shows a comparison between the present LES and RANS, the LES of Kim et al. (2012a) and the physical laboratory experiments of Kim et al. (2012b) in terms of cumulative RTD. As observed from this figure, the cumulative RTD curves predicted by RANS and LES are in excellent agreement with the physical experimental data. Characteristic residence times, t_{10}, t_{50}, and t_{90} (scaled by theoretical residence time τ) of the tracer were estimated from the cumulative RTD curves (Figure 4.15) and are listed in Table 4.5. The characteristic dimensionless residence times from both present RANS and LES are in good agreement with each other.

Figure 4.16 presents speed contours and streamlines from LES and RANS. In the case of LES, speed contours and streamlines are presented in terms of instantaneous fields and time-averaged fields. Note that Figure 4.16 is the same as Figure 4.3. The latter figure has been repeated here for ease of discussion. As described earlier, both RANS and LES solutions are characterized by a high-speed core jet (i.e. short-circuiting) extending from chamber to chamber and a secondary, slower-speed re-circulation zone (i.e. a dead zone) within each chamber. Note that these large-scale structures are baffle-induced, persistent and quasi-steady. Smaller scale eddies resolved by the LES and present near the entrance of each chamber are less stable. The main difference between the two simulations strategies here is that RANS is not able to capture these smaller scale eddies.

The main factors affecting tracer transport and associated RTD are the large scale short-circuiting and dead zones. Short-circuiting dominates the initial tracer passage through the contactor and thus t_{10} while dead zones dominate the tail shape of the RTD curve. Given that RANS and LES tracer residence time indices are similar and that RANS does not resolve the smaller scale eddies resolved by the LES, it is concluded that these small scale structures have negligible impact on the contactor's hydraulic efficiency.

The strength of baffle-induced short-circuiting changes temporally and spatially, but the end-to-end (inlet-to-outlet) extent of the short-circuiting is never interrupted. Since the short-circuiting is global and quasi-steady, RANS is well-suited to capture this flow structure (Figure 4.16a), unlike the highly unsteady spatial breakdown of the inlet jet in the column contactor analyzed earlier.

Figures 4.17 and 4.18 show RTD and cumulative RTD curves from RANS and LES simulations at different Reynolds numbers (Re = 2,740 and 5,480). No significant differences are

seen in terms of these quantities nor associated normalized characteristic residence times (listed in Table 4.6), further confirming that RANS performs on par with the LES for flow and tracer transport in baffled contactors.

4.3.3 Conclusions

Flow and passive tracer transport in a column contactor and a baffled contactor under different Reynolds numbers using RANS and LES methodologies were studied. Two main conclusions are described next.

LES is a reliable methodology for evaluating the hydraulic efficiency of water treatment contactors as it was shown to be able to capture flow features playing key roles in determining characteristic tracer residence times in the systems. Furthermore, the results from LES can be used to verify the accuracy of other less expensive simulation approaches, such as RANS. The drawback of LES is that it can become computational cost-intensive, especially for full-scale water treatment systems. However, current advancing computer technologies can lessen this drawback.

It was shown that RANS is reliable for conducting simulations of flow and tracer transport in contactors as long as there are no unsteady or unstable flow structures dictating the characteristic residence times of the systems. In the case of the column contactor studied here, mixing and consequently hydraulic performance of the contactor are strongly influenced by the spatial breakdown of the inlet jet and downstream transition to fully developed turbulence. RANS was not able to resolve this flow structure and thus did not provide an accurate evaluation of the hydraulic performance of the contactor. However, in the case of the baffled contactor, a quasi-steady, short-circuiting jet and associated dead zones that are important in determining the

hydraulic efficiency of the contactor, were resolved by RANS thus leading to accurate evaluation of contactor hydraulic performance.

Future research should focus on testing methodologies less computationally expensive than LES such as, for example, unsteady RANS (URANS, Johansson et al. 1993) or detached LES (DES, Spalart et al. 1997) for evaluating hydraulic performance of systems characterized by unsteady and unstable flow structures.

4.4 Chapter Summary

In this chapter RANS simulations of a baffled ozone contactor were conducted following a physical laboratory experiment detailed in the literature. Simulations performed on different grids lead to varying degrees of short-circuiting and dispersion which ultimately lead to differences in the residence time distribution (RTD) of the tracer (released at the inflow as a pulse). Predicted t_{10} index depends on grid density and RANS turbulence model. For fine grids that resolve the viscous sub-layer adjacent to no-slip boundaries, a turbulent model such as the k-ε model of Launder and Sharma (which is equipped to integrate the model equations down to the wall) has to be applied for accurate prediction of t_{10} index. The standard k-ε model was shown to yield good results on coarser meshes that do not resolve the viscous and buffer sub-layers. Overall, simulations on all considered grids with proper turbulence model yielded cumulative RTD and associated t_{10} index in good agreement with physical experimental data despite the under-resolution of the flow by the RANS methodology relative to a large-eddy simulation (LES) of the same flow. This result is encouraging in light of the significant discrepancy between computational (RANS) and experimental cumulative RTD recently obtained by other researchers for the same flow studied here (Kim et al. 2010b).

This chapter also conducted a careful assessment of RANS and LES in order to understand under which flow conditions LES should be recommended instead of the less computationally intensive RANS for predicting hydraulic performance of a disinfection system. Results from RANS and LES simulations of flow and tracer transport in a laboratory scale column contactor and a laboratory scale baffled contactor were presented; and flow fields, residence time distributions and characteristic residence times were analyzed. LES was shown to be a more reliable strategy than RANS in simulating tracer transport in column contactors due to its ability to better predict the spatial transition to turbulence characterizing the flow. However, in baffled contactors where such transition does not occur and the flow is characterized by a quasi-steady short circuiting jet and dead zones, RANS performs on par with LES.

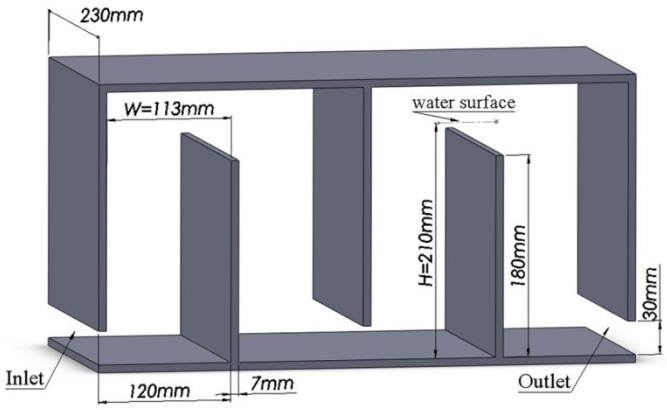

Figure 4.1: Flow domain dimensions.

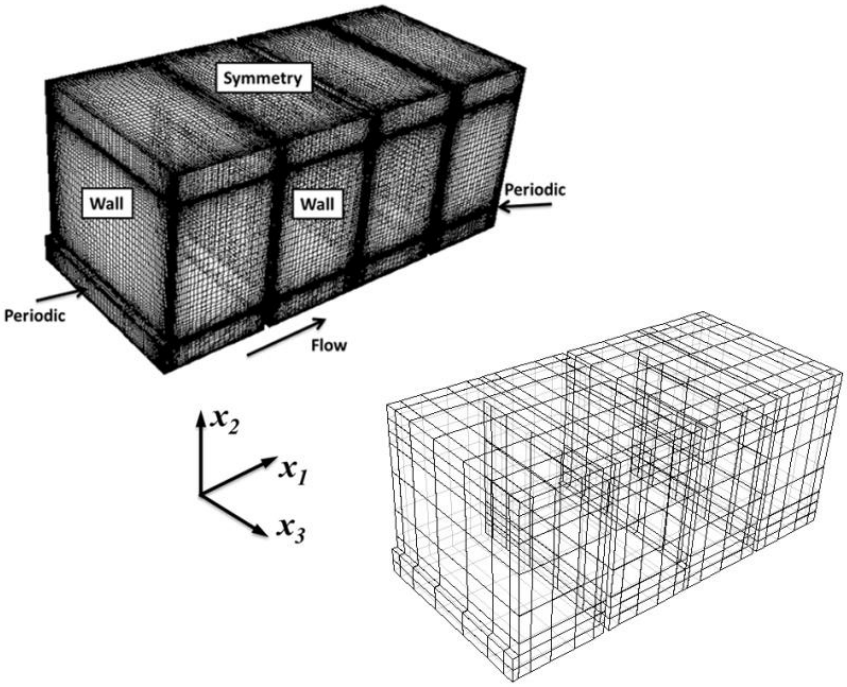

Figure 4.2: Finest (left) and coarsest (right) grids employed in RANS grid dependence study.

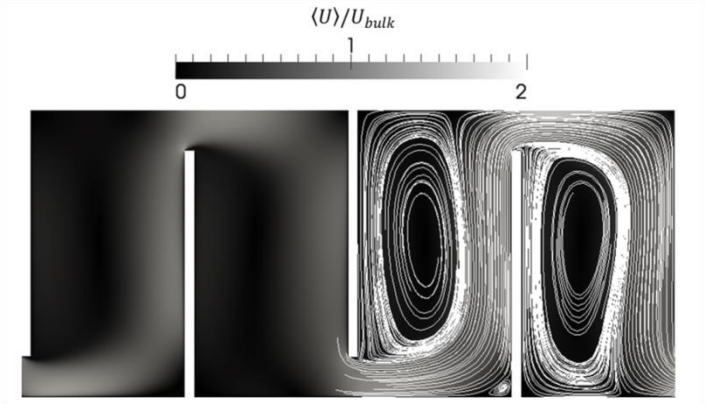

(a)

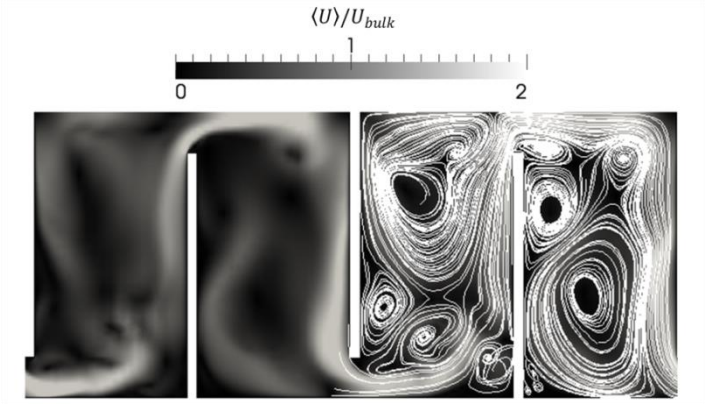

(b)

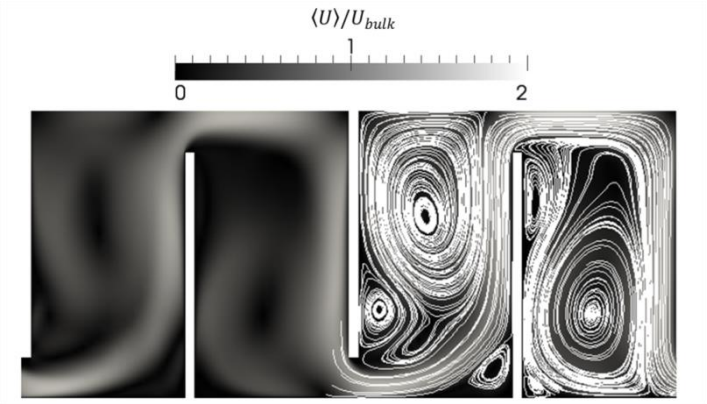

(c)

Figure 4.3: (a) x-y distribution of absolute velocity superimposed with corresponding streamlines (in last two chambers) in RANS on grid A; (b) Instantaneous and (c) time-averaged x-y distribution of absolute velocity superimposed with corresponding streamlines (in last two chambers) in LES. All cases are plotted on the x-y plane at mid span ($z = L/2$).

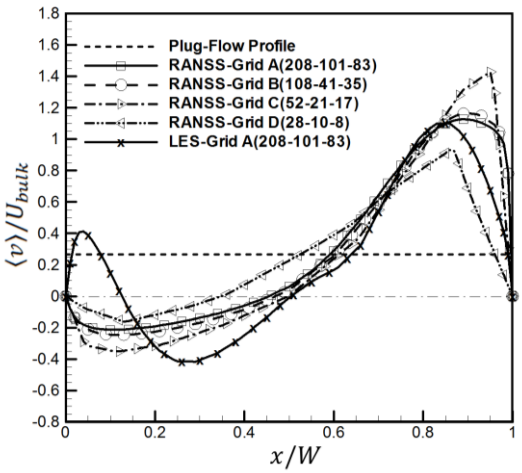

(a)

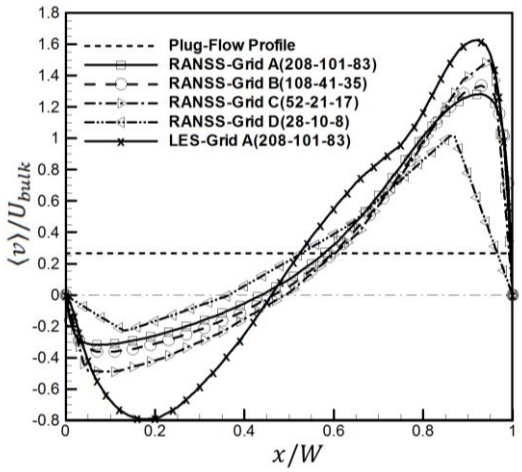

(b)

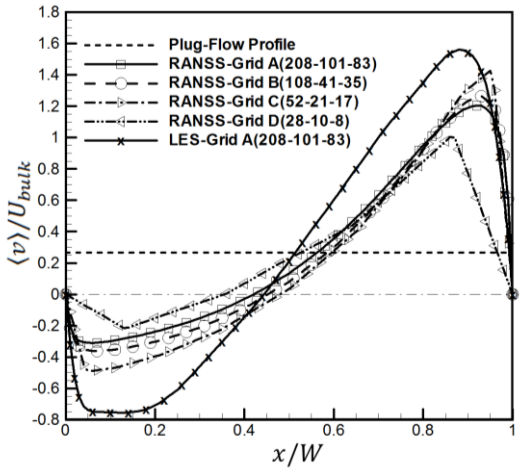

(c)

Figure 4.4: Y-velocity profiles across the chamber width (W) at different depths: (a) y/H = 0.27; (b) y/H = 0.50; (c) y/H = 0.72, where H is contactor height. For LES, profiles shown have been time-averaged.

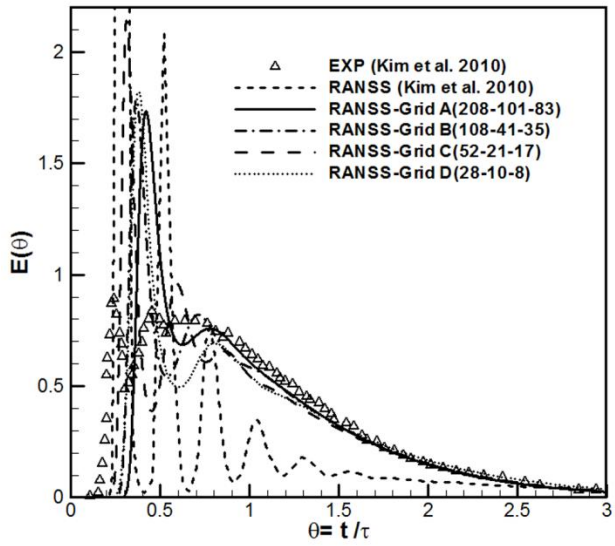

Figure 4.5: Comparison of tracer residence time distributions.

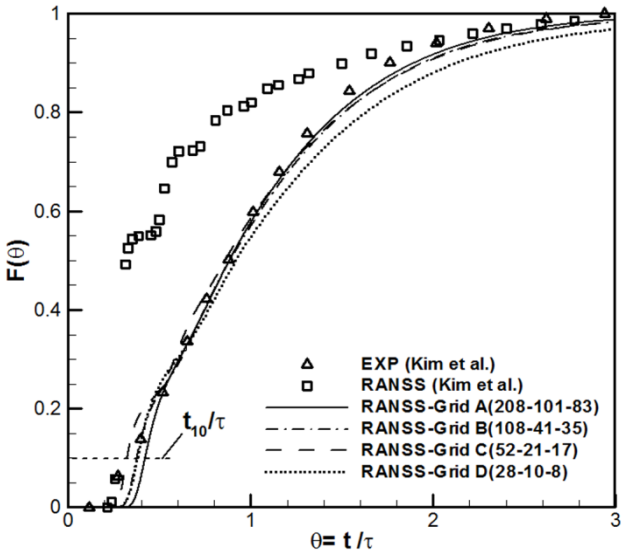

Figure 4.6: Comparison of cumulative residence time distributions.

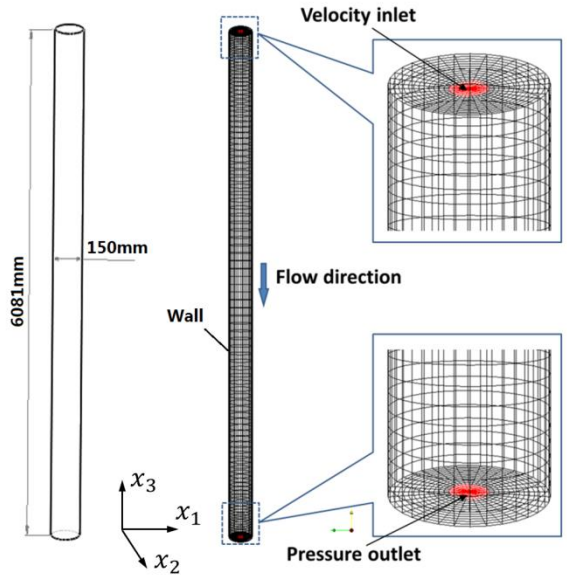

Figure 4.7: Layout and computational grid of column contactor following physical experiments of Chen (1998).

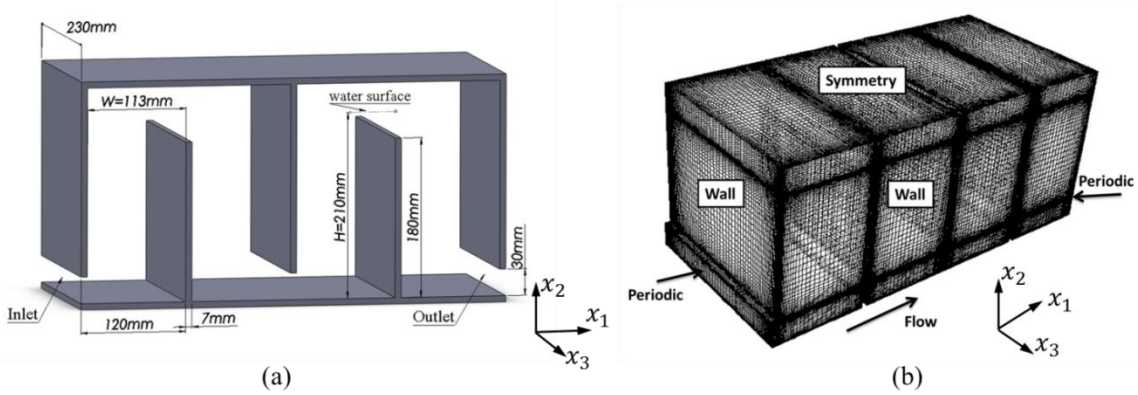

Figure 4.8: Layout (a) and grid (b) of baffled ozone contactor (Kim et al. 2010a).

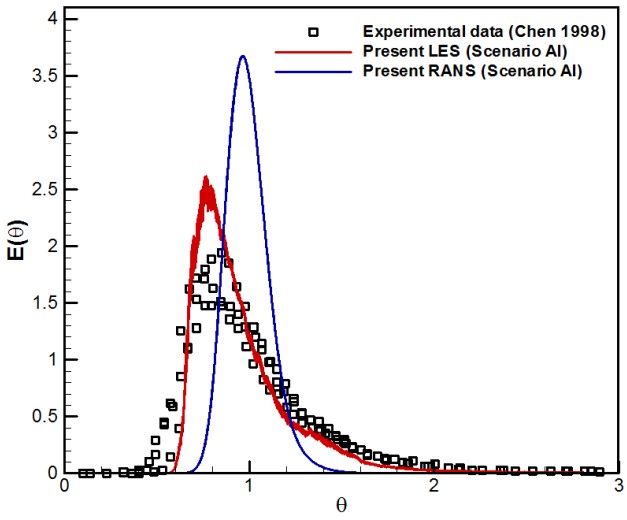

Figure 4.9: Comparison of normalized tracer concentration (i.e. RTD) measured at the outlet versus normalized time from the present numerical simulations (RANS and LES) and the physical experiment of Chen (1998) of the column contactor Re = 6900 (scenario AI).

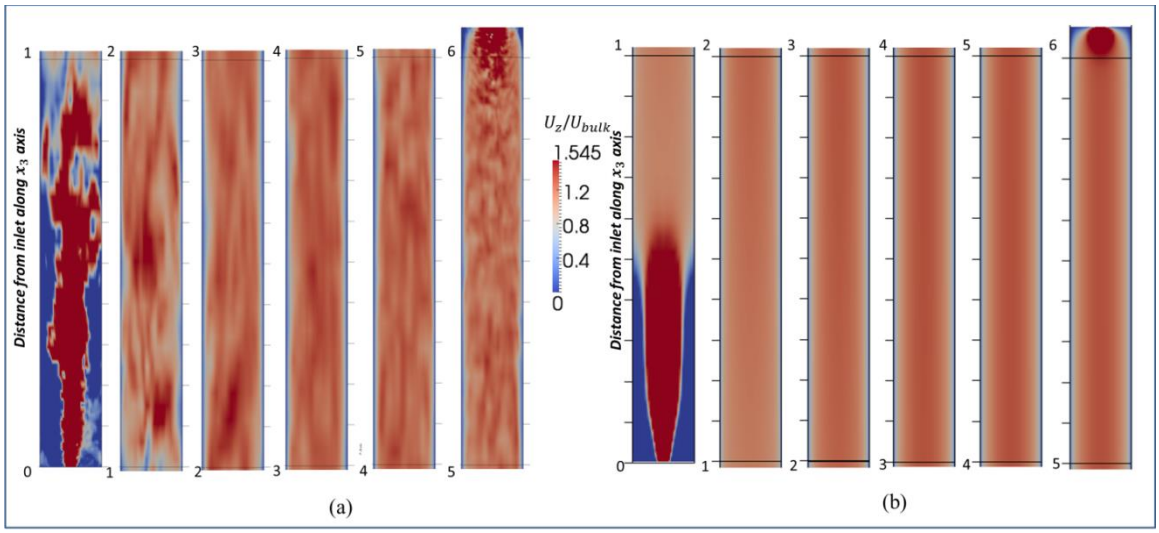

Figure 4.10: (a) Instantaneous stream-wise velocity contours from LES and (b) stream-wise velocity contours from RANS in the column contactor at Re = 6900 (scenario AI). Note that for ease of presentation, the column contactor has been split into 6 stream-wise segments. For example, segment 1 extends from the inlet cross-section up through 1 meter away from the inlet. Segment 2 extends from 1 meter away from the inlet through 2 meters away from the inlet and so on.

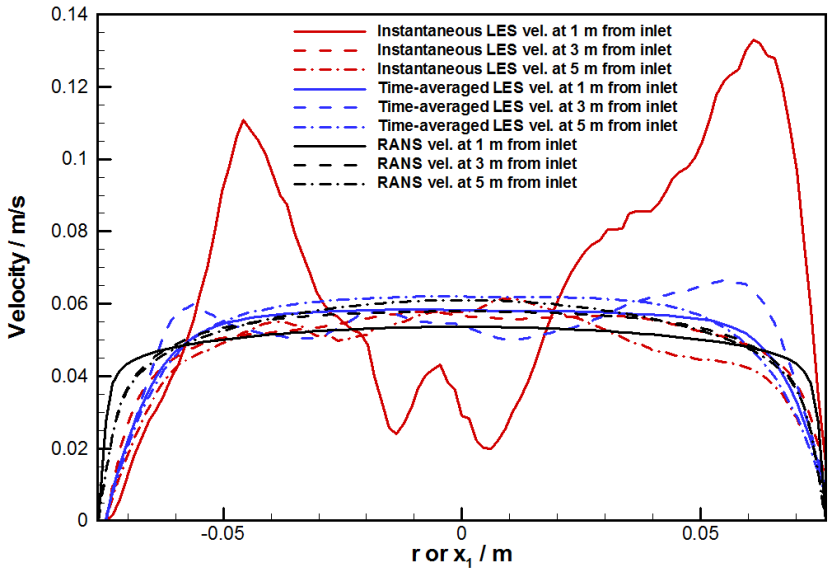

Figure 4.11: Variation of stream-wise velocity over various cross-sections of the column contactor for scenario AI.

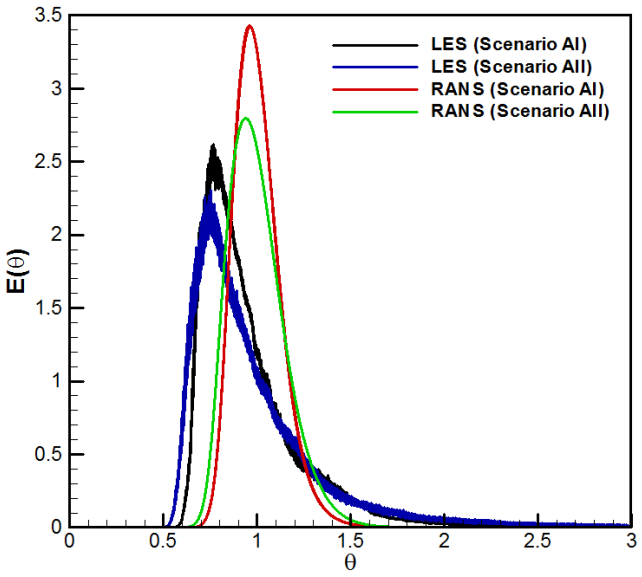

Figure 4.12: Normalized tracer concentration (i.e. RTD) versus normalized time for different scenarios in the column contactor.

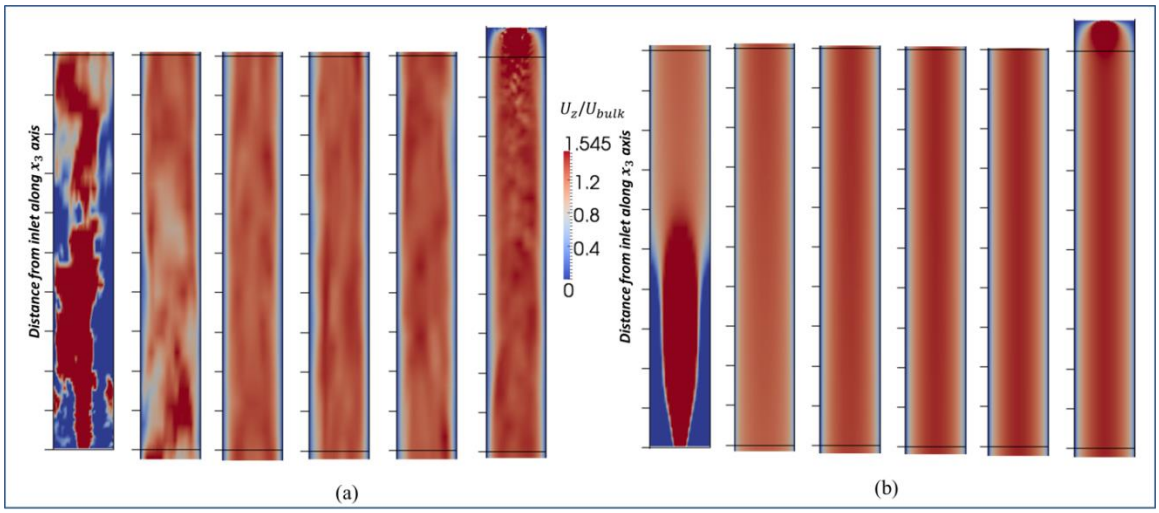

Figure 4.13: (a) Instantaneous stream-wise velocity contours from LES and (b) stream-wise velocity contours from RANS in the column contactor at Re = 1380 (scenario AII). See caption of Figure 4.9 for explanation of the different segments.

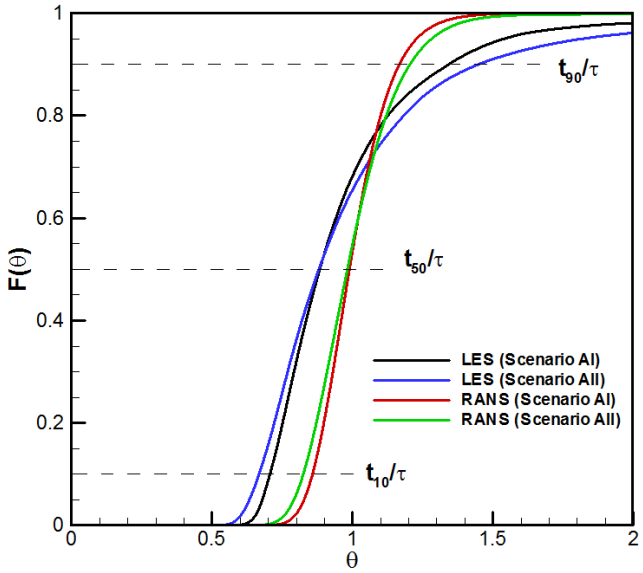

Figure 4.14: Cumulative normalized tracer concentration versus normalized time for different scenarios in the column contactor.

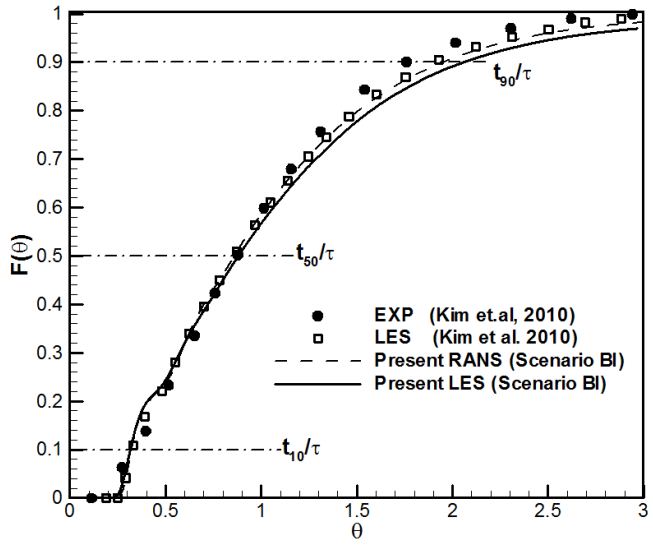

Figure 4.15: Comparison of cumulative residence time distributions from the present RANS and LES, the LES of Kim et al. (2010b) and physical experiment of Kim et al. (2010a) of the baffled contactor at Re = 2740 (scenario BI).

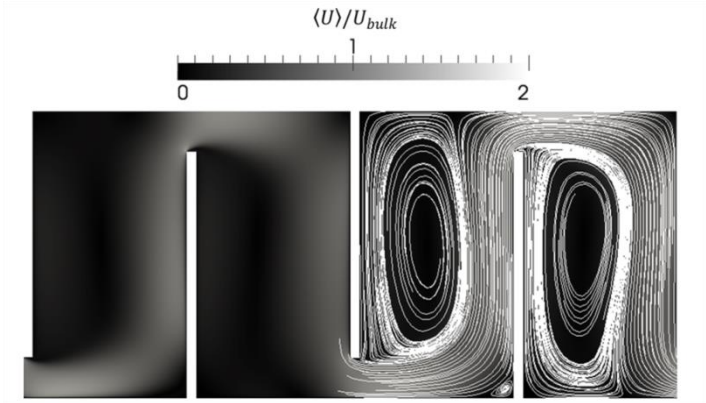

(a)

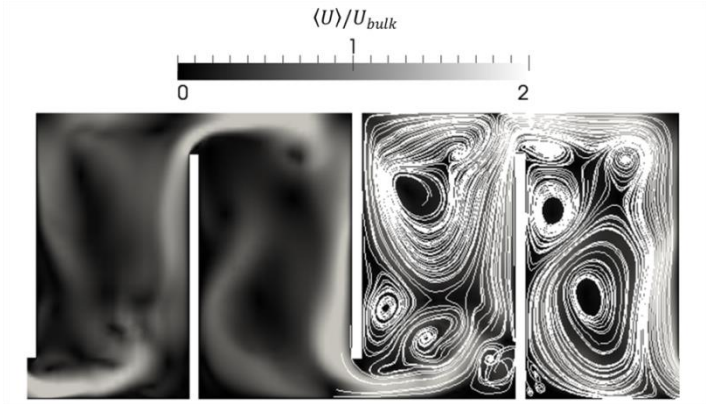

(b)

Figure 4.16: Speed contours and streamlines in the baffled contactor at Re = 2740 (scenario BI) from (a) RANS, (b) LES instantaneous result and (c) LES time-averaged result.

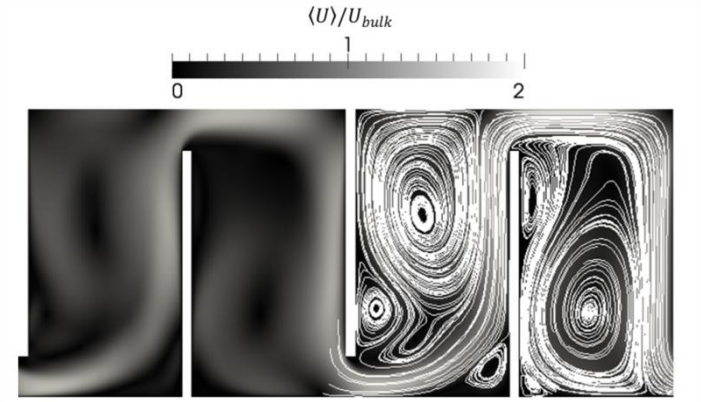

(c)

Figure 4.16 (Continued)

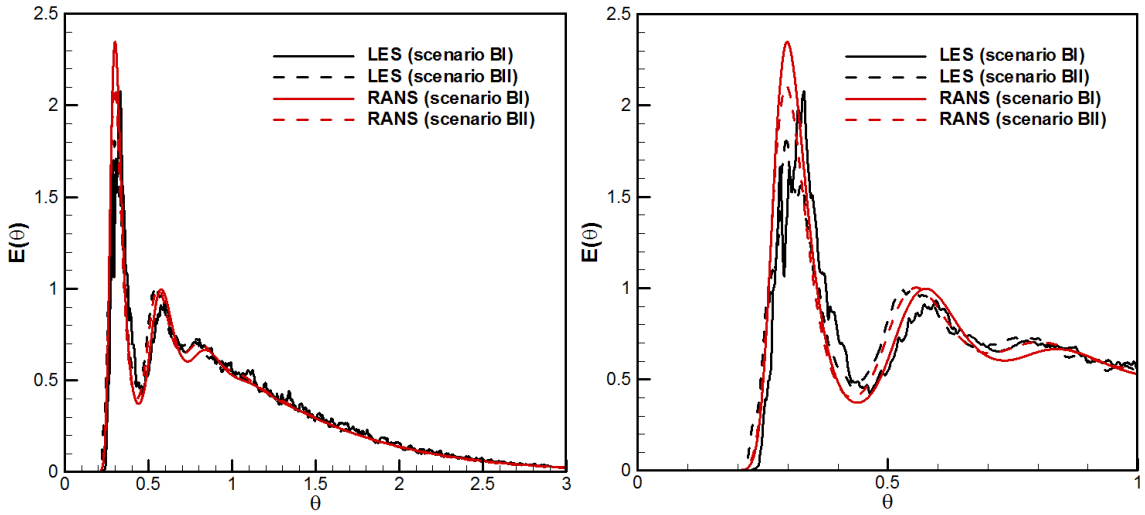

Figure 4.17: Normalized tracer concentration versus normalized time predicted by present LES and RANS of the baffled ozone contactor (the figure on the right is the same as the figure on the left but with different range in *x* axis).

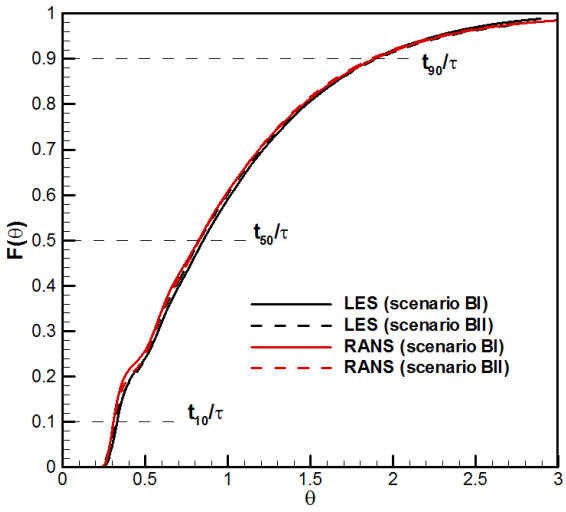

Figure 4.18: Cumulative normalized tracer concentration versus normalized time predicted by present LES and RANS of flow in the baffled contactor.

Table 4.1: Values of t_{10} scaled by theoretical mean residence time (τ = 109.2 s) and relative error with respect to experimental result of Kim et al. (2010b). All RANS were performed using the standard k-ε model except for those on grid A* and grid B*. RANS on grids A* and B* were performed on grids A and B, but with the Launder Sharma model (Launder and Sharma, 1974; Patel et al. 1985) instead of the standard *k*-ε model.

Case	t_{10}/τ	Relative error (%)
Present RANS on grid D	0.379	13.5
Present RANS on grid C	0.322	3.6
Present RANS on grid B	0.375	12.3
Present RANS on grid B*	0.34	1.8
Present RANS on grid A	0.421	26
Present RANS on grid A*	0.336	0.6
Kim et al.'s RANS on grid A	0.22	34.1
Kim et al.'s LES on grid A	0.30	10.2
Kim et al.'s experiment	0.334	NA

Table 4.2: A summary of the present numerical studies on disinfection contactors.

Contactor type	Scenario	Re	Flow rate / m^3/s	Theoretical Residence time / sec	Tracer release time
Column contactor (Chen 1998)	AI	6900	8.26×10^{-4}	134	2.0
	AII	1380	1.652×10^{-4}	671	10.0
Baffled contactor (Kim et al. 2010a)	BI	2740	2.0×10^{-4}	112	2.5
	BII	5480	4.0×10^{-4}	56	1.25

Table 4.3: Comparison of characteristic residence times from the present numerical simulations and experiment of Chen (1998) of the column contactor at Re = 6900 (scenario AI).

	T_1/τ	T_{peak}/τ	**Peak value of normalized concentration**
Experiment (Chen 1998)	~0.65	~0.82	~1.91
Present LES (scenario AI)	0.66	0.77	2.58
Present RANS (scenario AI)	0.81	0.96	3.67

Table 4.4: Characteristic residence times normalized by mean residence time τ for scenarios with different Reynolds number in the column contactor.

Scenario	**Model**	t_{10}/τ	t_{50}/τ	t_{90}/τ	**MDI**
AI (Re = 1380)	LES	0.6672	0.8800	1.4474	2.17
	RANS	0.8245	0.9814	1.2041	1.46
AII (Re = 6900)	LES	0.7057	0.8832	1.3411	1.90
	RANS	0.8573	0.9890	1.1664	1.36

Table 4.5: Comparison of characteristic dimensionless residence times from present simulation, LES (Kim et al. 2010a) and experiment (Kim et al. 2010b) of the baffled contactor at Re = 2740 (scenario BI).

	t_{10}/τ	Relative error	t_{50}/τ	Relative error	t_{90}/τ	Relative error
EXP (Kim et al. 2010b)	0.334	0%	0.875	0%	1.762	0%
LES (Kim et al. 2010a)	0.325	-2.7%	0.857	-2.1%	1.902	7.9%
Present LES	0.316	-5.4%	0.879	0.5%	2.057	16.7%
Present RANS	0.322	-3.6%	0.860	-1.7%	1.949	10.6%

Table 4.6: Characteristic residence times for scenarios with different Reynolds number predicted by present LES and RANS of flow in baffled contactor.

Scenario	Model	t_{10}/τ	t_{50}/τ	t_{90}/τ	MDI
BI (Re = 2740)	LES	0.3288	0.8501	1.8852	5.73
	RANS	0.3063	0.8214	1.8864	6.16
BII (Re = 5480)	LES	0.3176	0.8272	1.9026	5.99
	RANS	0.3086	0.8259	1.8654	6.04

CHAPTER 5: NUMERICAL STUDY ON A FULL-SCALE OZONE CONTACTOR IN CITY OF TAMPA WATER DEPARTMENT[2]

5.1 Introduction

The primary concerns in the second part of the CFD framework presented in Chapter 3 are (1) the degree of detail in the reaction system and (2) the models representing the reactions. Usually, a reaction system in ozone disinfection process consists of a large number of reactions. Thus it is necessary to develop a reduced reaction mechanism as was done in Chapter 3. The reduced reaction mechanism should contain key chemical species and reactions. In the simulation of ozone disinfection process, the most commonly considered reactions are ozone decomposition and reaction between ozone and instantaneous ozone demand (IOD) or natural organic matter (NOM). Only a few studies have incorporated bromate formation (Zhang 2006; Bartrand 2006; Zhang et al. 2007) as was done for the CFD framework developed in Chapter 3. A summary of the reaction systems used in prior CFD-based simulations of ozone disinfection was given in Table 2.4 and Figure 2.2 in Chapter 2. In the prior studies that have considered bromate formation, an empirical model under the assumption that bromate concentration changes linearly with ozone exposure was used to represent the process (Zhang 2006; Bartrand 2006; Zhang et al. 2007). Although Zhang (2006) and Zhang et al. (2007) have a bromate formation module in their framework, those author(s) deemed not practical to predict bromate formation

[2] Part of Chapter 5 is reprinted from Water Research, 52, Jie Zhang, Andrés E. Tejada-Martínez, Qiong Zhang, Hongxia Lei, Evaluating hydraulic and disinfection efficiencies of a full-scale ozone contactor using a RANS-based modeling framework, 155-167, Copyright (2014), with permission from Elsevier. Permission is included in Appendix D.

due to the sensitivity of the process of bromate formation to water quality. Bartrand (2006) showed prediction of bromate formation in the Alameda County Water District ozone contactor in Fremont, CA. However, the predictions were not compared with physical experimental data. Instead of empirical modeling, Mandel et al. (2012) used a quasi-mechanistic chemical model or kinetics-based model to represent the process of bromate formation. However, a systematic network was used by Mandel et al. (2012) to represent the flow, thereby reducing the accuracy of the flow solution and consequently reducing the fidelity of ozone and bromate concentration predictions.

In Chapter 3, a CFD-based framework including a kinetics-based reactions model in RANS species transport equations was developed for the ozonation process in ozone contactors. This framework should be suitable for the ozonation process in baffled contactors given the success of RANS in predicting the hydraulic performance of these contactors (Chapter 4). The reaction system for ozonation process in the current framework includes ozone self-decomposition, reaction between ozone and natural organic matter, and bromate formation (Chapter 3). In particular, bromate formation is modeled using kinetics-based modeling, unlike the previous CFD studies summarized above. In the present chapter, the computational framework prediction of ozone consumption and bromate formation are validated via comparisons with measured physical data from the full-scale ozone contactor at the City of Tampa Water Department. Note that, the results discussed in the present chapter have been included in a published manuscript (Zhang et al. 2014).

5.2 The Ozone Contactor Operated by City of Tampa Water Department

The City of Tampa Water Department treats and delivers daily drinking water to a service population of about 600,000 people in the Tampa Bay area (Kim et al. 2009). In 2000, a project

was carried out for improving the water quality at the David L. Tippin Water Treatment Facility managed by the City of Tampa Water Department. This project added an extra treatment process of ozonation/biological activated carbon (BAC) for improving water quality. The schematic diagram of treatment processes after the completion of the Water Quality 2000 Project is shown in Figure 5.1. The extra treatment process of ozonation is performed by two trains of ozone contactors. Each train has eight cells and an overall hydraulic residence time of 34 minutes at the designed flow rate of 85 million gallons per day (Kim et al. 2009). A sketch of one of the ozone contactor trains is shown in Figure 5.2.

The source water for the David L. Tippin Water Treatment Facility is the Hillsborough River. The ozone contactors (ozone dosing) run continuously. Concentrations of dissolved ozone are measured once per day at cell #2, cell #5 and at the contactor exit (Figure 5.2). These sampling locations are denoted as A, B, and C and marked in red dots in Figure 5.2. Concentrations of bromide and bromate are measured once per week at the entrance and exit of the contactor (see Figure 5.2, yellow dots). Thus, the conversion of bromide to bromate is calculated every week. Bromide and bromate concentrations are measured twice per week during times when bromide levels become relatively high. Note that bromate is a by-product of ozone disinfection. A long-term exposure to large amounts of bromate may cause human health issues. (U.S. EPA 2001)

Data collected from March 8 to July 21, 2011 is used in this dissertation. The data and the dimensions of the contactor have been provided by Dr. Hongxia Lei from the City of Tampa Water Department.

5.3 Numerical Set-up

To further validate the computational framework developed for this dissertation, simulations of the previously described full-scale ozone disinfection contactor were conducted. In order to compare with the data measured on site, the computational domain in the present study includes the middle eight chambers of the ozone contactor. The size of this computational domain is Length × Width × Height = 51.7m × 12.2m × 7.32m. The rest of the dimensions of the contactor including the dimensions of the baffles are given in Figure 5.3(a). The mesh used for all simulations has 881,050 structured cells, shown in Figure 5.3(b). In this mesh the y_1^+ distance of the first grid point away from the bottom or baffle walls is similar to that in grid C studied in section 4.2 (Chapter 4), that is $10 < y_1^+ < 50$. Thus the standard *k*-ε turbulence model is used. The water extends to a height H = 7.32m above the bottom and does not fill the entire contactor. The free-surface is treated as a no-penetration, zero-shear, rigid lid allowing full slip. Thus, the corresponding surface boundary conditions are $\partial\langle u_1\rangle/\partial x_2 = \partial\langle u_3\rangle/\partial x_2 = \langle u_2\rangle = 0$ where x_2 is the surface-normal direction and $\langle u_1\rangle$, $\langle u_2\rangle$ and $\langle u_3\rangle$ are the streamwise, surface-normal and spanwise velocities respectively. Velocity inlet boundary condition with a fixed flow rate is applied to the inlet. Pressure is imposed at the outlet. No-slip conditions are imposed at the bottom and other walls. The viscous wall regions are not resolved, however, everywhere the first grid point away from a no-slip boundary is less than 85 plus units thereby permitting the use of the standard k-ε turbulence model (Wilcox, 1994).

The strategy of simulation is based on the "frozen" flow approach described earlier. In this approach, the flow is solved first using RANS and then this "frozen" flow field is used to conduct separate simulations for concentrations of non-reactive tracer and reactive chemical species.

Five scenarios (scenarios I-V) with weekly averaged data measured on site from April to July 2011 were selected to set up the chemical reaction simulations and to compare with physical measurements. The flow rates in the ozone contactor were kept constant during each scenario, but vary from 45 to 55 MGD (million gallons per day) from scenario to scenario, as listed in Table 5.1. Different flow rates from those of Table 5.1 were used to conduct numerical tracer transport simulations in order to cover a wider range of flow rates. In the tracer simulations, the flow rates used are 33.8, 46.0 and 63.8 MGD, corresponding to the minimum flow rate in 2011, the averaged flow rate in April 2011, and the maximum flow rate in 2011.

In the numerical tracer simulations, a tracer pulse was released at the inlet within the first 2% of the theoretical residence time period. Note that the theoretical residence time varies from 2,180 s to 1,848 s. Other necessary inputs for the chemical reaction simulations, such as ozone dose or ozone concentration at diffuser, TOC concentration at inlet, TOC concentration removed by the ozone contactor, and bromide concentration at inlet are listed in Table 5.1. At the outlet and at the walls, the normal gradients of the tracer and chemical species are set to zero indicating zero diffusive flux across these boundaries.

Chemical time scale analysis is conducted to determine the closure method for the turbulence-chemistry interaction term described in section 3.3, Eqn. (3.33). Note that the values in the *Jacobian matrix* (Eqn. 3.37) depend on initial chemical conditions. In order to determine the chemical time scales in the most reaction-intensive situation, scenario II, in which the initial concentrations of the chemical species are higher than those in other scenarios, was selected. Inserting the initial conditions in scenario II (shown in Table 5.1) and the reaction rate constants in Table 3.2 (Chapter 3) into the *Jacobian matrix*, the chemical time scales in scenario II are ∞, 0.225, 0.210, 1.31, 339, and 17.1 seconds. The chemical time scales in the other scenarios are

higher than these in scenario II. Thus, all the chemical time scales in the present simulations are greater than the micro-mixing time scale which is estimated to be approximately 0.1 second following the Kolmogorov timescale defined in Eqn. (3.39). Thus, following the classification of Fox (2003), the chemical reaction system used in the present study can be classified as a slow chemistry system. Note that, the smallest chemical time scale (0.210 sec) is on the same order as the micro-mixing time scale (0.1 sec). This indicates that some of the reactions may possibly be categorized as finite-rate chemistry. In order to avoid increasing complexity of the modeling framework, the slow-chemistry limit is applied to all reactions.

Since the present chemical reaction system is in the slow-chemistry limit, the mixing is fast enough that the composition of variables, e.g. $\langle AB \rangle$, can be approximated by their mean values $\langle A \rangle \langle B \rangle$, and thus $\langle A'B' \rangle = 0$ in Eqn. (3.33).

5.4 Results and Discussion

In this section visualizations of the flow pattern in the full scale ozone contactor are firstly presented. Results from the tracer test are then analyzed to evaluate the hydraulic performance of the ozone contactor. Then, the simulation framework is validated by comparing predicted ozone concentrations with on-site measured data at sample points in the contactor tank. Based on predicted ozone concentration distribution, CT was calculated to evaluate the disinfection performance of the ozone contactor.

5.4.1 Flow Simulations

Figures 5.4(a) and 5.4(b) show absolute velocity (i.e. speed) and streamlines on the streamwise-vertical (x_1-x_2) plane at mid-span (x_3 = L/2 where L is the spanwise length of the contactor) respectively. The flow pattern is characterized by an undulating, high-speed core jet extending from chamber to chamber and a secondary, slower-speed re-circulation zone, or dead

zone, within each chamber. This core jet is similar to the core jet observed earlier in LES and RANS of a laboratory-scale ozone contactor. The core jet facilitates the passage of a portion of water through the whole length of the contactor over much shorter times than the mean residence time, resulting in short-circuiting and thus a reduction in hydraulic efficiency. Furthermore, regions of high speed flow can be found near the left side of each chamber. Note that, the high-speed core jet in the first chamber (the chamber on the right side) is more intense than that in other chambers because the inlet cross-sectional area of the first chamber is smaller than that of the other chambers. As observed from Figure 5.4(b), the size of dead zones varies in the different chambers. However, all of the dead zones occupy most of each chamber. More characteristics of the high-speed core jet and dead zones will be discussed in the following tracer simulation section.

5.4.2 Tracer Transport Simulation

Recall that tracer transport simulations were conducted for flow rates of 33.8, 46.0 and 63.8 MGD, corresponding to the minimum flow rate in 2011, the averaged flow rate in April 2011, and the maximum flow rate in 2011. These flow rates are different from the flow rates used in the chemical reaction simulations (listed in Table 5.2) in order to cover a wider range of flow rates.

Figure 5.5 shows instantaneous snapshots of tracer concentration at various points at different times for the tracer transport simulation with flow rate of 46.0 MGD. Recall that the tracer is released at the inlet during the first 2% of the theoretical residence time period of the simulation. Higher tracer concentrations are found close to baffle walls and near the surface. The effect of short-circuiting can be seen in the snapshots at times t = 1,600 s and t = 2,100 s showing non-negligible tracer concentration levels at the inlet and first chamber occurring simultaneously

as a large portion of the tracer in the last two chambers is close to exiting the contactor. Such behavior is due to entrapment of tracer within re-circulation (dead) zones. This shows that remnants of the tracer persist throughout the entire contactor for long times after its initial release.

Further analysis of tracer evolution was carried out by analyzing residence time distribution (RTD) and cumulative residence time distribution (CRTD), shown in Figure 5.6. Several peaks can be observed in the RTD curve in Figure 5.6. The first peak of the RTD is solely caused by short-circuiting. The following peaks result from the combined effect of re-circulation (dead) zones and short-circuiting. Note that, usually in laboratory-scale contactors the first peak has the highest value while the value of the following peaks decreases. However, in full-scale contactors, the theoretical residence time is much longer (2,180 s in this case) than in laboratory-scale contactors, and thus diffusion serves to attenuate the intensity of the first peak of the RTD curve. Finally, note that RTDs and CRTDs for the cases with different flow rates are quite similar.

Characteristic dimensionless residence time indices, $\theta_{10} = t_{10}/\tau$, $\theta_{50} = t_{50}/\tau$, and $\theta_{90} = t_{90}/\tau$, (scaled by theoretical residence time τ) of the tracer are estimated from the CRTDs in Figure 5.6; the time indices are listed in Table 5.2. In the present study, the calculated θ_{10} is approximately 0.43 for all flow rates simulated (33.8 MGD, 46.0 MGD and 66.8 MGD). But in the physical tracer tests conducted by the Tampa Water Department, θ_{10} was measured to be approximately 0.54 for flow rates ranging from 38 to 75 MGD. This difference in θ_{10} may be attributed to the fact that the predicted θ_{10} in the present study is for a truncated domain of the ozone contactor which excludes the inlet chamber before chamber #1 and the exit chamber after chamber #8 (see Figures 5.2 and 5.3a). Tracer concentration versus time was collected in the simulations at the exits of chambers 2 through 8. Based on these collected data, CRTD curves

were generated to estimate the θ_{10}s corresponding to truncated domains with two to seven chambers (Figures 5.7 and 5.8). As observed from Figure 5.8, the value of θ_{10} increases from 0.19 to 0.43 as the number of domain chambers increases from 2 to 8. This indicates that the value of θ_{10} would be higher than 0.43, which is closer to the measured value, if the chambers before chamber #1 and after chamber #8 were to be included in the simulations.

Furthermore, a simulation was conducted for the scenario with flow rate 46 MGD with expanded domain including the inlet and exit chambers in addition to the interior chambers. The θ_{10} value obtained in the simulation was 0.492 in better agreement with the physical data (0.54) than the θ_{10} value obtained with the truncated domain domain. Overall this exercise shows the dependence that residence time indices can have on truncated domains. Throughout the remainder of this chapter, simulation results reported are based on the truncated (8-chamber) contactor shown in Figure 5.3b unless specified otherwise.

The Morrill dispersion index (MDI) is also calculated from the characteristic dimensionless residence time indices. The MDIs obtained from the scenarios with different flow rates are slightly different, but all of them are close to 4.0.

Note that even as the flow rate increases by 88.7% from 33.8 MGD to 63.8 MGD, the corresponding changes in θ_{10} and MDI are negligible (less than 2.5%). This indicates the θ_{10} and MDI of a full scale ozone contactor are nearly independent of flow rate. However, the mean residence time decreases as flow rate increases. As shown in Table 5.2, doubling the flow rate serves to decrease the mean residence time by a factor of two, ultimately leading to a decrease in disinfection efficiency. More discussion on this will be given further below in terms of contact time or CT.

5.4.3 Chemical Reaction Simulations

Figure 5.9 (a-e) shows the distribution of ozone concentration on the streamwise-vertical (x_1-x_2) plane at mid-span of the ozone contactor for scenarios I through V, respectively. For all scenarios of Table 5.1, the following phenomena are similar: a high ozone concentration region can be observed at the bottom of chambers 1 and 2 since it is where the ozone diffuser is located. In the first chamber, dissolved ozone accumulates within the dead zone while the ozone concentration in the high-speed core jet is relatively low. However, in the second chamber, the ozone concentration in the high-speed core jet is much higher than that in the dead zone. This is because the ozone diffuser in the first chamber is mostly located within the region of the dead zone while the ozone diffuser in the second chamber is located within the region of the high-speed core jet. In the following six chambers, the ozone concentration in the high-speed jet region is higher than that in the dead zones, as there are no ozone sources within these chambers. Note that transfer of ozone between dead zones and high-speed jet is by diffusion.

Comparing all panels in Figure 5.10, the overall ozone concentration in scenario II is higher than the others, due to its high ozone dose at the diffuser. Note that concentration of ozone in scenario I is lower than that in scenario III in spite of the ozone dose at the diffuser in scenario I being higher than that in scenario III. The reason is that the influent TOC concentration in scenario I is much higher than that in scenario III. Such influent consumes more ozone and consequently results in the lower ozone concentration in the first chamber in scenario I.

In Figure 5.10, the predicted ozone concentrations are compared with physical measured data for all scenarios at the sample points marked in Figure 5.2. In Fig. 5.10, it can be observed that all the data points are close to the bisector with an R-square equal to 0.93. This indicates that

the predictions of ozone concentrations have good agreement with the physical experimental data, serving to validate the chemical reaction simulations conducted as well as the overall computational framework. Furthermore, now that the predicted ozone concentration distribution has been shown to be reliable it may be used for the prediction of contact time or CT distribution, as will described in the next section.

Table 5.3 shows a comparison between predicted and measured bromate concentration at the outlet. The simulations tend to underestimate the bromate concentrations at the outlet of the domain. The predictions are approximately within 40% to 87% of the corresponding physical experimental data. The underestimation of outlet bromate concentrations could be caused by the following reasons:

1. The neglect of hydroxyl radical pathway of bromate formation: Although in the present study the hydroxyl radical pathway was deemed less important than the molecular pathway, as described in Chapter 3, it may still play a significant role in the process of bromate formation.
2. The underestimation of turbulence-chemistry interaction: Although the micro-mixing time scale was found to be less than all of the chemical timescales, the former was found to be on the order of the smallest chemical time scales. This indicates that some of the reactions could be considered as finite-rate chemistry. However for simplicity the entire system was assumed to be slow chemistry and thus all the covariance terms of chemical concentration fluctuations were set to zero. However, some of the covariances may be significant enough to impact the mean concentrations, especially the mean concentration with small values such as the bromate concentrations.

3. Uncertainty of the equilibrium assumption: The percentage of B_rO^- for bromate formation, $p_{B_rO^-}$, was estimated as 14% (recall Chapter 3) based on the equilibrium assumption at pH = 6.5. Note that p depends on pH to some extent and that $p_{B_rO^-}$ tends to increase as pH decreases (Haag and Holgne 1983). A sensitivity study of the predicted bromate concentration at the outlet with respect to $p_{B_rO^-}$ was conducted for scenario III and the results are shown in Figure 5.11. It can be observed from this figure that a slight increase in $p_{B_rO^-}$ (which is possible because the pH in this scenario is 6.43 which is lower than 6.5), can lead to a better prediction by the simulation. Figure 5.11 shows that a value of $p_{B_rO^-}$ ~ 40% would lead to excellent results in terms of the prediction of bromate concentration. Unfortunately it is not possible to determine the corresponding value of pH for $p_{B_rO^-}$ = 40% because Haag and Holgne (1983) only studied three cases with pH=6.1, 6.5 and 7.2, respectively.
4. Underestimation of baffling factor: Recall that in the scenarios explored here with an 8-chamber truncated domain, the baffling factor (θ_{10}) was ~0.43, lower than the 0.54 measured physically. This under-prediction of the baffling factor could potentially lead to under-prediction of bromate concentration at the outlet of the domain. In order to test this, a simulation with the entire contactor domain (i.e. the 8 chambers plus the inlet and exit chambers (see Fig. 5.2)) was conducted for scenario 3. The predicted value of the baffling factor was found to be 0.492 in better agreement with the physical measurements (0.54) than the original simulations with truncated domain. However, the predicted bromate concentration at the outlet with the expanded computational domain was 0.00282mg/L, under-predicting the physically measured value with a predicted-to-measured ratio of 39.7%. Comparing this ratio to the ratios

reported in Table 5.3 for the truncated domain, it is concluded that expansion of the computational domain to accommodate the full length of the contactor does not lead to significant change in predicted bromate concentration. Furthermore, under-estimation of the baffling factor obtained with the truncated computational domain may be discarded as a potentially major reason for the under-prediction of bromate concentration at the outlet of the domain.

Finally, note that since the bromate concentration at the contactor outlet has a much smaller value than the other chemical species, it is challenging to predict it accurately. Overall, the predictions from the present simulations are acceptable because they are on the same order as the measured experimental physical data.

5.4.4 CT Prediction

Based on the predicted ozone distribution in the contactor, CT distributions were obtained by solving the transport equation for CT (see equation (3.38)). CT distributions are shown in Figure 5.12. For all the scenarios, a CT gradient exists across the dead zones and the high-speed core jet in the first two chambers. For subsequent chambers, this CT gradient gradually disappears as CT distribution tends to be uniform within each chamber.

Table 5.4 lists the values of average CT at contactor outlet and theoretical residence time for all scenarios. The average CT value varies depending on the overall ozone concentration distribution and the mean residence time. The average CT in scenario II (22.06 mg·min/L) is the highest among the five scenarios. This is mainly because scenario II has the highest ozone distribution, as can be seen in Figure 5.9. Although scenario I has a relative low ozone distribution, it still has the second highest CT value at 14.04 mg·min/L. The reason is that scenario I has the longest mean residence time which is approximately 22% higher than the

shortest mean residence time in the five scenarios, based on Table 5.4 assuming mean residence time is approximately equal to theoretical residence time for the cases studied here. (Note that based on the tracer simulations performed, the mean residence time tends to be very close to the theoretical residence time (see Table 5.2), therefore, it is reasonable to use the theoretical residence time to represent the mean residence time here.) In conclusion, besides ozone dose, the mean residence time, which is related to seasonal flow rate change, is also a critical factor for determining the disinfection efficiency measured in terms of CT.

A summary of reported ozonation CT requirements for 99 percent inactivation of selected pathogens which are regulated by U.S. EPA under safe drinking water act is shown in Table 5.5. The predicted average CT values at the outlet for all the scenarios are higher than the ozonation requirements for 99 percent inactivation of pathogens. Thus, it can be concluded that the ozone contactor operated by the City of Tampa Water Department is able to meet disinfection regulations.

5.5 Summary and Future Work

In this chapter, a CFD-based (RANS-based) computational framework for the ozonation process in a full-scale ozone contactor was validated. This framework was validated via comparison with physical experimental data from the ozone contactor of the City of Tampa Water Department. The computed predictions of ozone concentrations at sample points agree well with the physical experimental data. Although the computed predictions of bromate concentration at the contactor outlet were underestimated with respect to the physical experimental data, they were on the same order as the physical data. Based on the predicted ozone concentration distribution, CT at the outlet was calculated for different scenarios. Average CT values at the outlet demonstrated that the ozone contactor studied is able to meet disinfection

regulations. Numerical tracer studies conducted indicate that seasonal flow rate changes do not impact dimensionless time indices of a full-scale ozone contactor, such as θ_{10} and MDI. However, flow rate increment can reduce the mean residence time and consequently lower disinfection efficiency. Thus, water/wastewater treatment plant managers should carefully monitor potential changes in disinfection efficiency caused by seasonal flow rate changes.

Results of this initial attempt to combine CFD with a kinetics-based reaction model are encouraging. The new CFD framework with a kinetics-based reaction model for bromate has eliminated the drawback of previous frameworks with empirical models for bromate in which the empirical reaction rate constant needs to be calibrated for the specific disinfection system being modeled.

The reaction system in a contactor varies for different situations. Therefore, a good representation of the reaction system, including accurate reaction rate constants for kinetics-based modeling, should be obtained before applying a framework such as the one proposed in this dissertation. Note that these reaction rate constants are specific to basic reaction kinetics and do not have to be calibrated for the specific water disinfection system being modeled (as are the empirical reaction rate constants discussed earlier). As observed in the present study in terms of predicted bromate concentration and uncertainty of the percentage of B_rO^- for bromate formation (p), uncertainties of reaction kinetics and reaction rate constants can become significant error sources. Only with more accurate reaction kinetics and reaction rate constants, it would be feasible to conduct further studies of more complex flows involving important unsteady flow features and turbulence-chemistry interactions. Such studies would have to be performed with LES in order properly capture unsteady flow features that could be important for accurately determining hydraulic (disinfection) efficiency and flow-chemistry interaction.

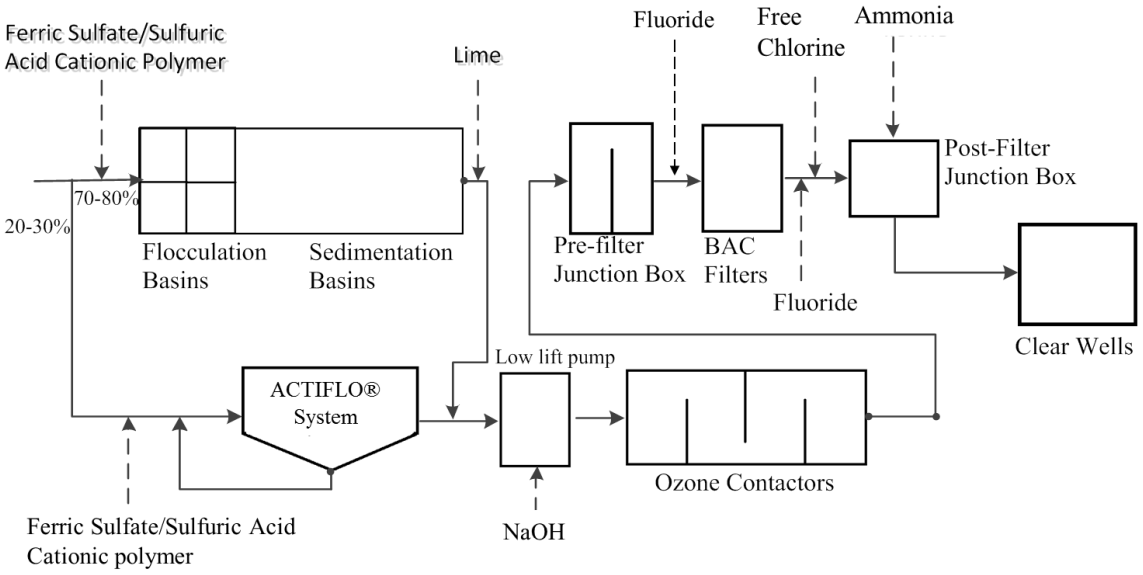

Figure 5.1: Schematic diagram of treatment processes in the David L. Tippin Water Treatment Facility (City of Tampa Water Department) after the completion of the Water Quality 2000 Project (Kim et al. 2009).

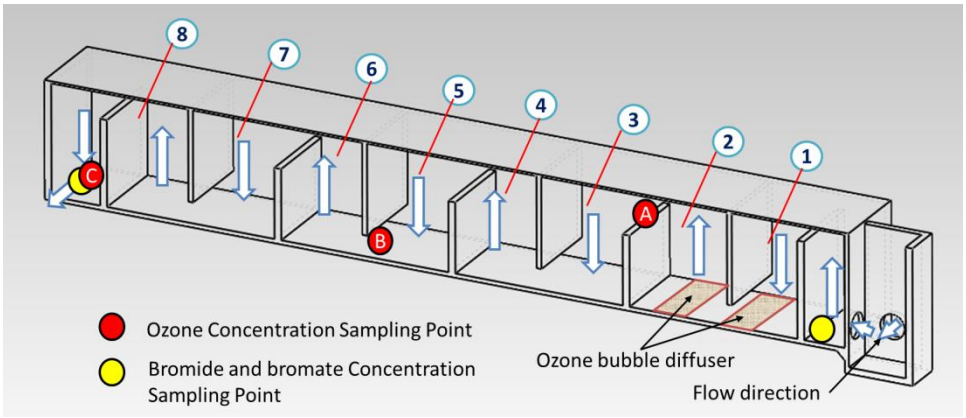

Figure 5.2: Layout showing chamber numbers and ozone and bromate sampling points in one of the ozone contactor trains in the David L. Tippin Water Treatment Facility (City of Tampa Water Department). Note that the flow goes from right to left and thus chambers are counted from right to left.

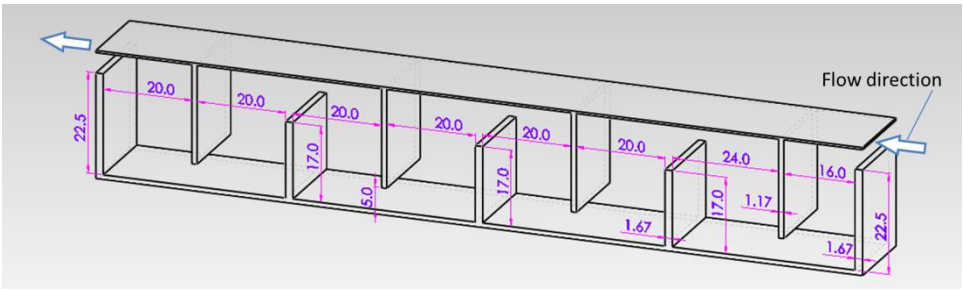

(a)

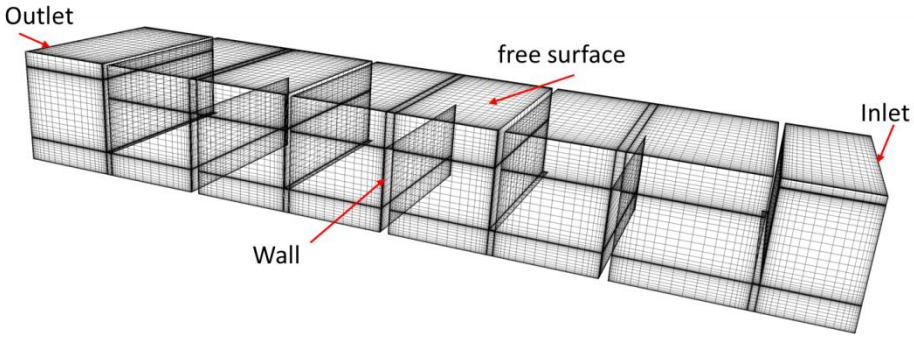

(b)

Figure 5.3: (a) Layout showing chamber number, (b) dimensions (unit: inch) and (c) computational grid of ozone contactor in the David L. Tippin Water Treatment Facility (City of Tampa Water Department). Note that the flow goes from right to left and thus chambers are counted from right to left.

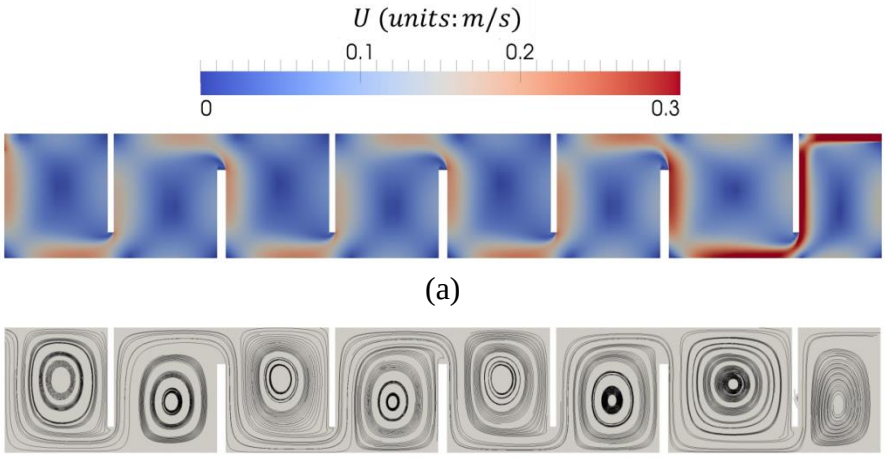

(a)

(b)

Figure 5.4: (a) Speed contours and (b) streamlines on the streamwise-vertical (x_1-x_2) plane at mid-span of the simulated full-scale ozone contactor for scenario I. Note that, the flow direction is from right to left.

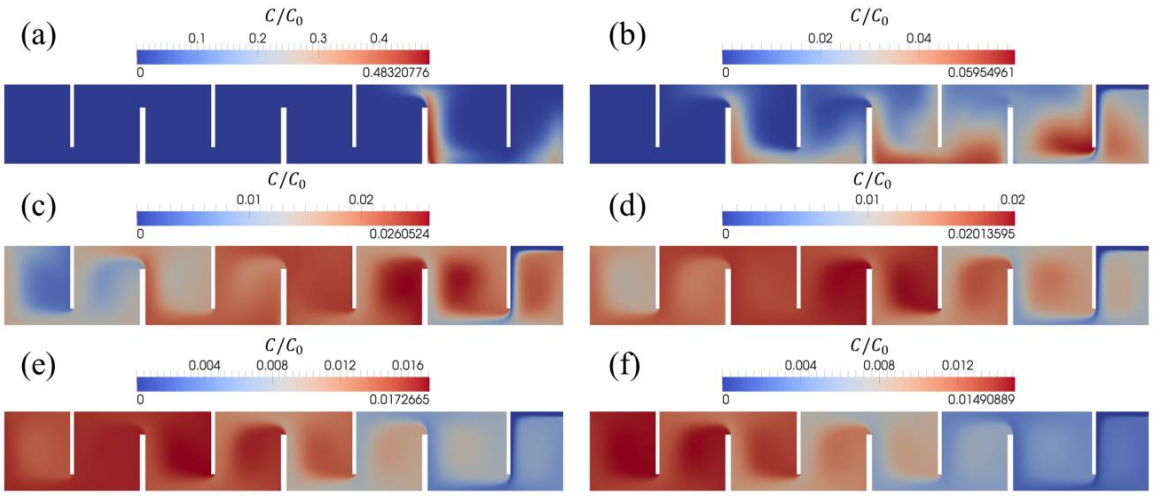

Figure 5.5: Instantaneous snapshots of tracer concentration on the streamwise-vertical (x_1-x_2) plane at mid-span of the ozone contactor at various times: (a) t=100s; (b) t=400s; (c) t=800s; (d) t=1200s; (e) t=1600s; and (f) t=2100s. The flow rate is 46.0 MGD. The flow direction is from right to left.

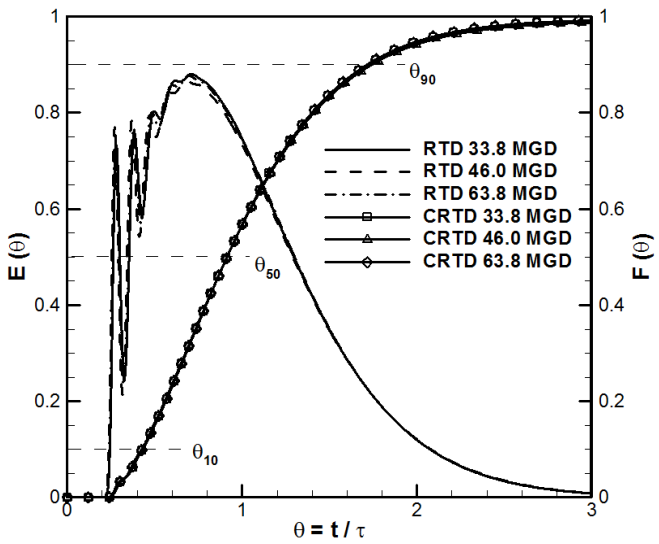

Figure 5.6: Normalized residence time distribution (RTD) (left axis) and cumulative residence time distribution (CRTD) (right axis) for different flow rates.

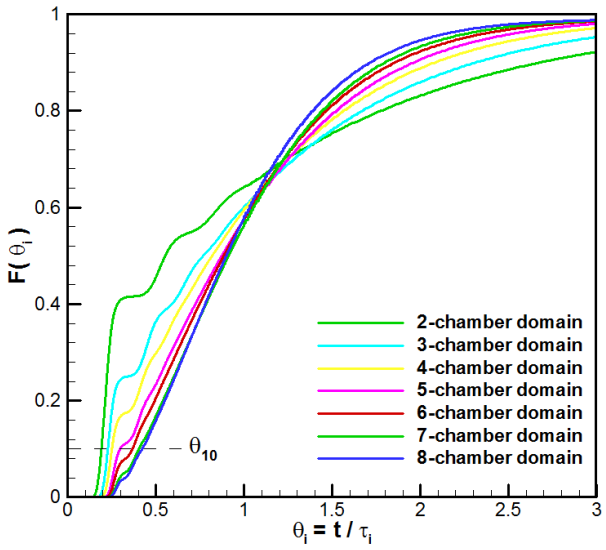

Figure 5.7: Cumulative residence time distribution curves for contactor domains with different number of chambers. Flow rate used was 46.0 MGD in all cases.

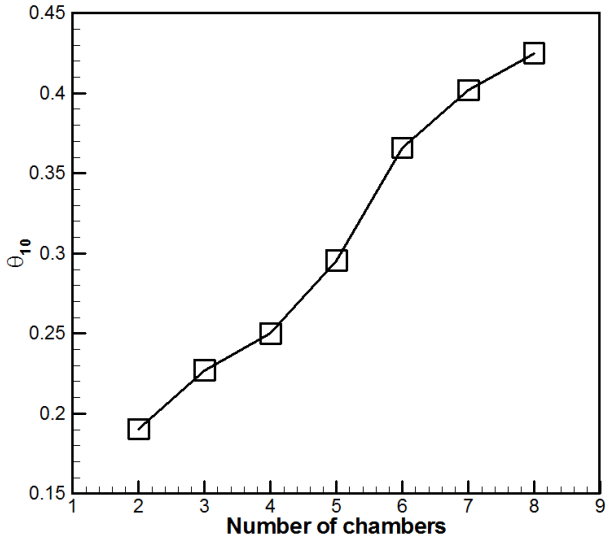

Figure 5.8: The change of θ_{10} with increment of number of chambers. The flow rate used was 46.0 MGD.

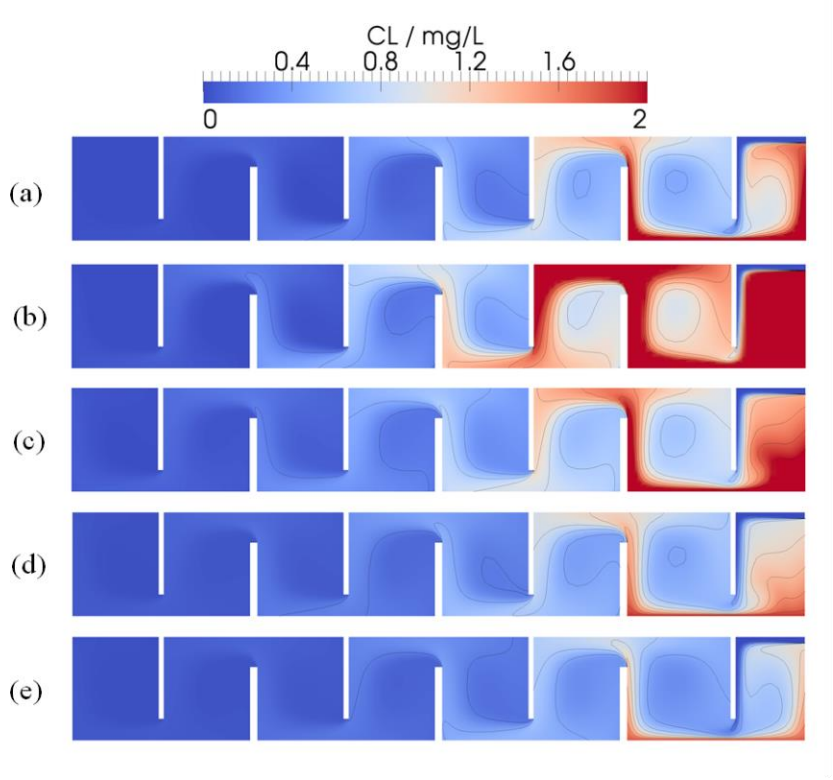

Figure 5.9: Ozone concentration contour on streamwise-vertical plane at mid-span of the ozone contactor for scenarios (a) I, (b) II, (c) III, (d) IV, and (e) V. Note that the flow direction is from right to left (i.e. from chamber #1 through #8).

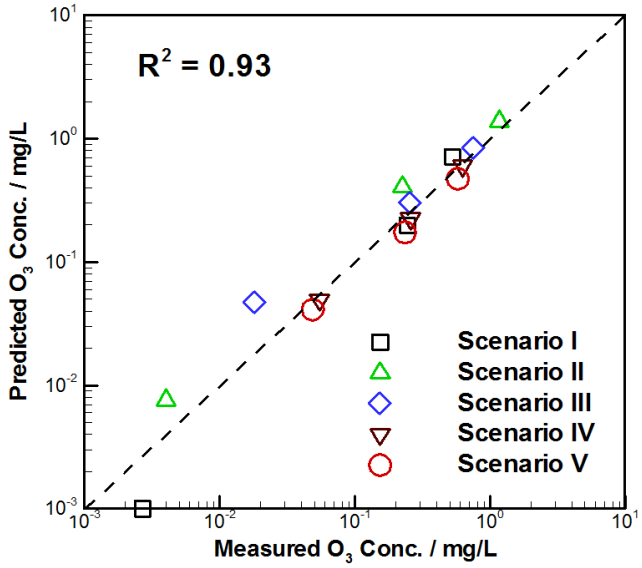

Figure 5.10: Comparison of predicted and measured ozone concentration at the sample points A, B, and C for different scenarios

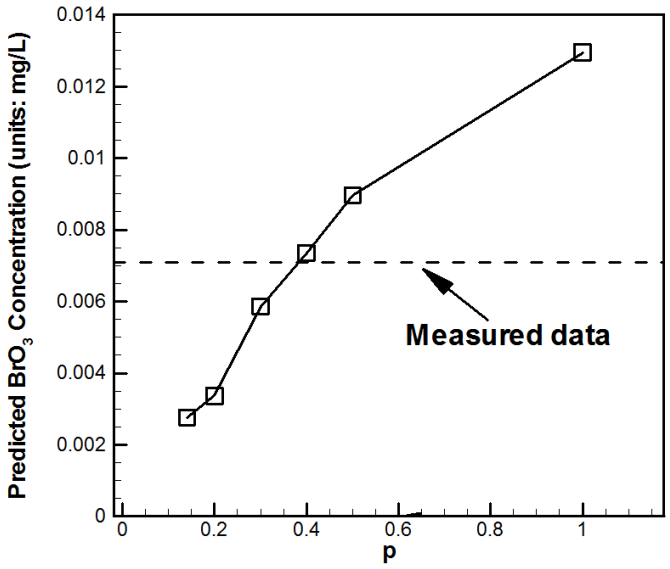

Figure 5.11: Predicted bromate concentration as a function of $p_{B_rO^-}$, the percentage of B_rO^- for bromate formation. Simulations were conducted under scenario III.

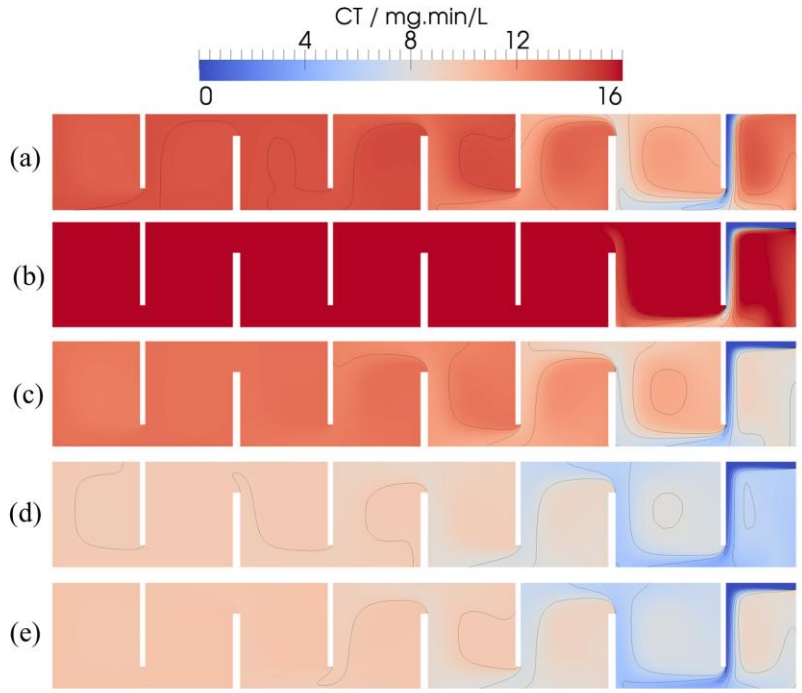

Figure 5.12: CT distribution on the streamwise-vertical (x_1-x_2) plane at mid-span of the contactor for scenarios I-V (a-e, respectively). Note that, the flow direction is from right to left (i.e. from chamber #1 through #8).

Table 5.1: Operation parameters in the ozone contactor of the City of Tampa Water Department used for chemical reaction simulations.

	Scenario I	Scenario II	Scenario III	Scenario IV	Scenario V
Duration	Apr 4-12	Apr 27-May 2	May 19-25	Jun 4-Jun 16	Jun 30-Jul 11
Flow rate / MGD	45.40	50.65	54.53	55.39	45.82
pH	6.500	6.550	6.430	6.310	6.280
Ozone conc. at diffuser / mg/L	2.982	4.975	2.744	1.903	1.770
TOC conc. at inlet / mg/L	3.200	4.900	3.200	1.800	1.350
TOC conc. removed by the ozone contactor / mg/L	0.400	0.400	0.200	0.000	0.000
Bromide conc. at inlet / mg/L	0.036	0.053	0.150	0.242	0.137

Table 5.2: Time indices for scenarios with different flow rates.

Time Index	**Flow rate (MGD)**		
	33.8	**46.0**	**66.8**
$\boldsymbol{\theta_{10} = t_{10}/\tau}$	0.4301	0.4249	0.4287
$\boldsymbol{\theta_{50} = t_{50}/\tau}$	0.9129	0.9131	0.9131
$\boldsymbol{\theta_{90} = t_{90}/\tau}$	1.7175	1.7400	1.7133
MDI $= \boldsymbol{\theta_{90}/\theta_{10}}$	3.9930	4.0950	3.9960
Theoretical residence time / s	2981.8	2181.5	1579.7
Mean residence time / s	2972.3	2143.8	1573.9

Table 5.3: Comparison of predicted and measured bromate concentration at outlet (unit: mg/L).

Scenario	Measured	Prediction	Prediction / Measured
I	0.00070	0.00061	87.1%
II	0.00140	0.00078	55.5%
III	0.00710	0.00276	38.8%
IV	0.00640	0.00313	49.1%
V	0.00740	0.00281	38.2%

Table 5.4: Comparison of average CTs at outlet for different scenarios at 20 ˚C.

Scenario	Theoretical residence time (sec)	Average CT at outlet (mg·min/L)
I	2220.0	14.04
II	1989.9	22.06
III	1848.3	13.19
IV	1819.7	9.560
V	2199.4	9.970

Table 5.5: Summary of reported ozonation CT requirements for 99 percent inactivation of selected pathogens.

Species	pH	Temperature (C)	CT (mg·min/L)	Reference
Cryptosporidium muris oocysts	8.40	23.6	7.8	Owens et al. 1994
Cryptosporidium parvum oocysts	8.24	24.5	5.5	Owens et al. 1994
Giardia muris cysts	7.57	25.2	0.28 – 1.04	Owens et al. 1994
Viruses	N/A	25.0	0.15	Canada Ministry of Health and Long-Term Care 2008
Escherichia coli	6 – 7	5.0	0.02	Hoff 1986

CHAPTER 6: EXTENDED APPLICATIONS[3]

This chapter presents extended applications of the modeling framework developed in this dissertation. First, an investigation of the hydraulic efficiency and its impact on energy consumption of baffled ozone contactors is presented. The energy consumption here refers to energy required for ozone generation in addition to hydraulic energy loss. A second application involves the study of the hydraulic efficiency of a water stabilization pond and comparison with tracer field measurements.

6.1 Hydraulic Efficiency and Energy Consumption of Ozone Disinfection

6.1.1 Introduction

Continued advances in computational power have enabled CFD analysis of the flow in ozone reactors leading to a detailed description of the flow behavior. As seen in previous chapters, CFD solutions are able to identify localized flow phenomena such as short-circuiting and dead zones which hinder disinfection efficiency. Increasing the number of baffles is a commonly used approach to reduce dead zones and diminish short-circuiting. Several studies have concluded that an increase of the number of baffles usually leads the fluid flow to approach plug-flow conditions characteristic of a plug-flow reactor (Kim et al. 2010a; Amini et al. 2011; Wols et al. 2008a). However, hydraulic energy loss due to friction may also increase when the number of baffles increases. On the other hand, an increase in hydraulic efficiency by an increase in the number of baffles would lead to lower doses of ozone applied, which would lead to lower

[3] Section 6.1 is reprinted from Journal of Hydraulic Engineering, 139(11), Jie Zhang, Andrés E. Tejada-Martínez, Qiong Zhang, Hydraulic Efficiency in RANS of the Flow in Multi-Chambered Ozone Contactors, 1150-1157, Copyright (2013), with permission from ASCE. Permission is included in Appendix D.

energy demand for ozone generation. These issues/relationships have not been investigated in previous studies.

In this section, RANS of the two ozone contactors of Kim et al. (2010b) and a third contactor, which is hypothetical, are performed in order to compare the differences in performance caused by narrowing chamber width. Baffling performances of the three ozone contactors are compared based on hydraulic efficiency measured from passive tracer concentration distributions. Additional comparison between the three contactors is made through estimates of energy loss due to friction. A trade-off between baffling performance and energy loss is identified for the first time, as previous works have focused on baffling performance (hydraulic efficiency) only. Ultimately, it is seen that the energy saving due to a lower demand for ozone generation afforded by improving hydraulic efficiency is able to offset the friction energy loss incurred by the addition of baffles required to enhance baffling performance. Furthermore, energy loss due to friction in flow through a contactor is identified as an important component to consider when determining ozone disinfection and overall water treatment plant operation costs.

6.1.2 Flow Domain and Boundary Conditions

The flow configurations consist of the baffled ozone contactor studied in the physical experiments of Kim et al. (2010a) and the LES and RANS of Kim et al. (2010b), as noted earlier. The laboratory scale contactor of Kim et al. (2010a) consisted of 12 chambers. A truncated version consisting of 4 chambers was considered in the computations of Kim et al. (2010b) and was also considered for the present computations. This was the domain studied earlier in Chapter 4, but described here again for completeness. The section formed by the 4 chambers (chamber width is 0.113m) is 0.48 m long in the streamwise (x_1) direction and 0.23 m wide in the

spanwise (x_3) direction. The rest of the dimensions of the contactor including the dimensions of the baffles are given in Figure 6.1a. The other two contactors studied in the present computations have the same dimensions except with twice and thrice the number of chambers, respectively, corresponding to approximately half (0.053m) and quarter (0.033m) chamber widths of the original contactor. The geometries of the three contactors are shown in Figures 6.1a-c. Henceforth, the original contactor is denoted as NW (for normal chamber width), the second contactor is denoted as HW (for half chamber width) and the third contactor as QW (for quarter chamber width). The structured grids employed in RANS of flows through NW, HW and QW models have 1,394,000 cells, 1,738,400 cells, and 1,974,960 cells respectively, shown in Figure 6.2. Note that the increase of grid points is caused by the increase of wall boundaries (baffles). Based on wall-resolution considerations, the Launder-Sharma model (Launder and Sharma, 1974; Patel et al. 1985) studied earlier was employed. The water extends to a height H = 0.21 m above the bottom and does not fill the entire contactor. The free-surface is treated as a no-penetration, zero-shear, rigid lid allowing full slip. Thus, the corresponding surface boundary conditions are $\partial\langle u_1\rangle/\partial x_2 = \partial\langle u_3\rangle/\partial x_2 = \langle u_2\rangle = 0$ where x_2 is the surface-normal direction and $\langle u_1\rangle$, $\langle u_2\rangle$ and $\langle u_3\rangle$ are the streamwise, surface-normal and spanwise velocities respectively. No-slip conditions are imposed at the bottom and baffle walls and the inlet and outlet are periodic for velocity and pressure. The streamwise body force f_1 appearing in the x_1 momentum equation in (2) is prescribed such that the Reynolds number is 2740 based on hydraulic diameter ($h_R = \sqrt{4A_c/\pi}$, where A_c is the cross section area at the inlet/outlet) and target bulk velocity U_{bulk} at the periodic inlet/outlet. This corresponds to the Reynolds number in the laboratory experiment of Kim et al. (2010a) and in the computations of Kim et al. (2010b). This approach leads to the same flow rate Q passing through all contactor models considered (NW, HW and

QW). Using this flow rate, an alternate Reynolds number may be defined based on chamber dimensions: $Re_{ch} = (4Q/P)/\nu$ where ν is kinematic viscosity and P is the perimeter of the cross-sectional chamber area normal to x_2. For the NW, HW and QW models considered, the values of Re_{ch} are 1143, 1413 and 1521, respectively.

Once the steady state RANS solution of the flow is computed (Eqns. 3.17-3.20), the scalar advection-diffusion transport equation for the passive tracer in (3.22-3.23) is solved using the steady flow velocity. The numerical tracer study is conducted by initially releasing a tracer pulse with concentration $\langle C \rangle = 1$ at the inlet over a 2.5 second period. At the outlet and at the walls, the normal gradients of $\langle C \rangle$ are set to zero indicating zero diffusive flux across these boundaries.

6.1.3 Results and Discussion

Figures 6.3a-c show absolute velocity (i.e. speed) superimposed with streamlines in the RANS performed with the grids depicted in Figures 6.2a-c respectively. Absolute velocity and streamlines are shown for the streamwise-vertical (x_1-x_2) plane at mid-span (x_3 = L/2 where L is the spanwise length of the contactor). The flow patterns in both models are similarly characterized by an undulating, high-speed core jet extending from chamber to chamber and a secondary, slower-speed re-circulation zone, or dead zone, within each chamber. The core jet facilitates the passage of a portion of water through the whole length of the contactor over much shorter times than the mean residence time, resulting in short-circuiting and thus a reduction in hydraulic (disinfection) efficiency. Furthermore, regions of high speed flow can be found near the right side of each chamber and at the exits of each chamber where the speed can reach up to twice the inlet/outlet bulk velocity due to the presence of baffles. As the number of baffles increases or chamber width narrows, the length of short-circuiting increases due to a more

bended flow path caused by the baffles. Comparing Figures 6.3a-c, the slower-speed re-circulation zones, or dead zones, decrease significantly as the number of baffle increases. In the NW model, dead zones stretch out over most of the vertical length of the baffles and occupy approximately two thirds of each chamber width. Meanwhile the dead zones in the HW model are much smaller, stretching out over no more than half the length of a baffle and extending over approximately half a chamber width. Furthermore, the dead zones in the QW model are the smallest, stretching out over approximately one sixth of the length of the baffle and one third of a chamber width. These characteristics indicate that the QW model gives rise to a flow closest to a plug flow, which is ideal for disinfection efficiency. This will be further demonstrated by the study of the passive tracer advected through the contactors presented further below.

In Figure 6.4, profiles of the *y*-component (x_2-component) of velocity versus chamber width along *x* (x_1) are plotted for each flow at different depths. In the RANS with the NW model, the *y*-velocity vector changes direction from negative *y* to positive *y* along the chamber width at all three depths shown, in accordance with the presence of the re-circulation zone or dead-zone occupying a large part of the chamber, seen in Figure 6.3a. Note that the *y*-velocity magnitude is greater along the right side of the chamber coinciding with the high-speed core jet. In the RANS with the HW model, the *y*-velocity vector has obvious direction change only at depth y/H = 0.27 (x_2/H = 0.27), in accordance with the presence of the re-circulation zone occupying a small part of the chamber, seen in Figure 6.3b. Note that *H* is the height of the water in the contactor. In the RANS of the QW model, the direction change of the *y*-velocity vector is small even at depth y/H = 0.27. Furthermore, in the RANS of the QW model, the velocity profile at depth y/H = 0.72 shows a trend towards the velocity profile in an ideal plug flow reactor (PFR) which is not observed in the RANS of the other two models. Such behavior further indicates that the QW

model is closer to a PFR than the other two models. Overall, the flow structures in Figure 6.3 and velocity profiles in Figure 6.4 agree with those in the LES of Kim et al. (2010b).

Figure 6.5 shows instantaneous snapshots of tracer concentration at various points in time for the RANS of flow through the NW model. Recall that the tracer is released at the inlet during the first 2.5 seconds of the simulation. Higher tracer concentrations are found close to baffle walls and near the surface, in agreement with the LES and experiments of Kim et al. (2010a, b, respectively). The effect of short-circuiting can be seen in the snapshots at times t = 90 s and t = 112.5 s showing non-negligible tracer concentration levels at the inlet occurring simultaneously as a large portion of the tracer in the third and fourth chambers is close to exiting the contactor. Such behavior is due to entrapment of tracer within re-circulation (dead) zones. This shows that remnants of the tracer persist throughout the entire contactor for long times after its initial release.

A similar trend is observed in the RANS of the HW model (Figure 6.6). However, comparing the concentration snapshots between RANS with the NW model and the HW model at corresponding times, e.g. t = 90.0 s or t = 112.5 s (110.0 s), the behavior caused by entrapment of tracer within re-circulation zones is less apparent in the HW model due to the diminishing of the dead zone regions. Overall, Figures 6.5 and 6.6 show that in the RANS with the HW model, the tracer is less diffuse and thus more concentrated as it travels through the contactor in comparison with the tracer distribution in the RANS with the NW model. Note that the same color-bars denoting tracer concentrations are used at each corresponding time in Figures 6.5, 6.6 and 6.7.

In the RANS with the QW model (Figure 6.7), at time t = 110 s, non-negligible tracer concentrations are only observed in the second to last and last chambers, unlike in models NW and HW (Figures 6.5 and 6.6). This indicates that the entrapment of tracer within dead zone

regions is the weakest in the QW model out of the three cases. This is consistent with the dead zone regions observed in Figure 6.3.

Comparing Figures 6.6 and 6.7, high concentration regions of tracer at t =20 s for both HW and QW models are limited to approximately one chamber. At t = 40 s and 60 s, high concentration regions have spread to approximately two and three chambers, respectively, in both HW and QW models due to the universality of diffusion. However, the actual occupied region of high tracer concentration in the QW model is limited within a smaller space as the chambers in this model are narrower. This is consistent with the assumption used for PFR that diffusion occurs only within a small segment. Overall, results described here show that adding more chambers to a reactor with fixed volume can lead the reactor to behave closer to an ideal PFR model.

Further analysis of tracer evolution is carried out by comparing cumulative residence time distribution (CRTD) with results from previous physical laboratory experiments and computations (Kim et al. 2010a, b), shown in Figure 6.8. Characteristic dimensionless residence times, t_{10}/τ, t_{50}/τ, and t_{90}/τ, (scaled by theoretical residence time τ) of the tracer in models NW and HW are estimated from the CRTD curves, and are listed in Tables 6.1 and 6.2, respectively.

Figure 6.8 compares CRTD curves from the present RANS with CRTD curves from prior physical laboratory experiments of Kim et al. (2010a) and prior LES and RANS of Kim et al. (2010b). Present RANS with the NW model yields a CRTD curve and characteristic residence times in excellent agreement with the CRTD curves recorded in the physical experiment and LES of Kim et al. (2010a, b). Furthermore the present RANS results of the flow through the NW model are in closer agreement with the LES and experiments of Kim et al. (2010a, b) than the

RANS results of Kim et al. (2010b). Similar trends are also observed for the HW model, although comparison here is with respect to the LES of Kim et al. (2010b) only, as no physical experiments were conducted for this model. Finally, the CRTD curve obtained in the RANS with the QW model is closest to the CRTD curve for PFR (plug flow reactor) compared to the CRTD curves obtained with the other models, as expected based on earlier analysis.

Ideally, the flow in a contactor should resemble that of a plug flow reactor. In a plug flow reactor the flow entering spreads across the width and remains in the reactor for exactly one hydraulic residence time $\tau = V/Q$ where V is the volume of the reactor and Q is the volumetric flow rate going through it. This helps to achieve the desired disinfection efficiency while minimizing undesired disinfection by-products such as bromate (Roustan et al. 1993).

In the following discussion, θ_{10} will be highlighted because it has been traditionally used for classification of contactors by U.S. EPA (2003). Table 6.3 lists θ_{10} for all models considered. Note that the θ_{10} value listed for the NW model is taken from the experiments of Kim et al. (2010a); the θ_{10} listed for the HW model is taken from the LES result of Kim et al. (2010b); and the θ_{10} listed for the QW model is taken from the present RANS. According to a reactor classification of U.S. EPA, the NW model is classified as a reactor of poor baffling condition because its θ_{10} of 0.3 is relatively far from 1 which corresponds to the θ_{10} value of an ideal plug flow reactor. The HW and QW models are classified as reactors of superior baffling conditions because their θ_{10} values reach 0.700 and 0.780 respectively.

As previously discussed, an increase in the number of chambers increases the baffling performance of a reactor. Next, energy consumption associated with the increase in the number of chambers is investigated. Based on Eqn. (B.3), the values of energy loss for the NW, HW and QW models are 1.2×10^{-3} kWh/m^3, 2.0×10^{-3} kWh/m^3 and 3.5×10^{-3} kWh/m^3, respectively, with a

ratio of 1:1.7:2.9. Friction energy losses in the flows through the HW and QW models are respectively 66.7% and 191.7% higher than that in the NW model. This indicates a trade-off between baffling performance and energy consumption. Figure 6.9 shows a clear trend in the relationship between energy loss and baffling factor. An increase in the number of chambers and thus an increase in baffling factor (θ_{10}) towards the ideal value of 1.0 is accompanied by a disproportionate energy loss. For example, an increase in the baffling factor from 0.700 to 0.780 (i.e. an increase of approximately 10%) between the HW and QW models, respectively, is accompanied by a 71% increase in energy consumption. Thus, it is important to consider energy consumption as a key variable to optimize the design of ozone contactors in terms of both reactor performance and environmental sustainability.

A typical value of total energy consumption rate for a water treatment plant without considering ozone disinfection is 1.4kWh/1000 gallons or 0.37kWh/m^3. The ozone disinfection process increases energy consumption by about 0.12 to 0.55 kWh/1000 gallons corresponding to 0.032 and 0.145 kWh/m^3 (Elliott et al. 2003). Typically, 90% of the energy consumption in the ozone disinfection process is attributed to ozone generation while the remaining 10% is attributed to distribution and cooling. Based on the above information, we can compare the energy required for driving the flow (equivalent to the energy loss due to friction calculated in our simulations through equation 9) to the energy required for ozone generation for the three models studied (NW, HW and QW). This comparison is made in Table 6.4 below. This table also compares the energy required to drive the flow plus energy required for ozone generation to the total energy consumption for a plant (0.37 kWh/m^3).

Table 6.4 explores two scenarios. In scenario I, it is assumed that the energy consumed in the ozone disinfection process in the NW model is 0.032 kWh/m^3, with 90% of this energy (or

0.0288 kWh/m^3) consumed by ozone generation. In scenario II, it is assumed that the energy consumed in the ozone disinfection process in the NW model is 0.145 kWh/m^3, with 90% of this energy (or 0.1305 kWh/m^3) consumed by ozone generation. Furthermore, as can be seen by analyzing columns 3, 4 and 5 of Table 6.4, hydraulic efficiency (or baffling performance) is taken inversely proportional to energy required for ozone generation; the interested reader is directed to EPA guidance manuals (1991, 2003), Lee et al. (2011) and Phares et al. (2009) for more information about this. For example a 47.7% percent increase in hydraulic efficiency in model HW (0.700) with respect to model NW (0.334), translates to a 47.7% drop in energy required for ozone generation (i.e. under scenario I, the energy requirement for ozone generation in the HW model goes down to 0.0137 kWh/m^3 from 0.0288 kWh/m^3 in the NW model).

Three important conclusions can be obtained from analysis of Table 6.4. First, comparing columns 2, 4 and 5, it can be seen that the significance of energy consumption for driving the flow relative to the energy required for ozone generation becomes greater as more baffles are added to the contactor (*viz.* in going from the NW model to the QW model) in order to increase baffling performance. The second key conclusion can be obtained by analyzing columns 3, 4, 5, 8 and 9. It is seen that the energy saving afforded by increasing the hydraulic efficiency (thus requiring less ozone generation) offsets the energy increase required for driving the flow through a more hydraulically efficient contactor (characterized by more baffles). For the hydraulically efficient QW contactor model studied here, the energy required for driving the flow plus the energy required for ozone generation serves to increase total energy consumption by as much as 16%. In contrast, for the NW contactor characterized by poor hydraulic efficiency, the energy required for driving the flow plus the energy required for ozone generation serves to increase total energy consumption by a greater amount (as much as 36%), thereby demonstrating the

benefit of the QW contactor despite its greater friction energy loss. Overall, it is seen that energy considerations associated with contactor hydraulic efficiency (i.e. energy loss due to friction and energy required for ozone generation) are important for determining the operational costs of a plant.

6.1.4 Summary and Conclusions

RANS-predicted cumulative residence time distribution (RTD) of a passive tracer (released at the inlet as a pulse) in baffled ozone contactors was shown to be in excellent agreement with experimental data and large eddy simulation (LES), despite the under-resolution of the RANS methodology compared with better resolved methodologies such as LES. The RANS performance was shown to be much better than previously reported by Kim et al. (2010b).

A comparison of the baffling performance and energy loss of three ozone contactor configurations was made based on RANS results. A trade-off between baffling performance and energy loss due to friction was identified for the first time, as previous works have focused on baffling performance only. Specifically, it was found that increasing the number of baffles or chambers would increase baffling performance but also energy loss due to friction. Furthermore, a detailed comparison was made between the energy required for driving the flow (equivalent to the energy loss due to friction calculated in our simulations) and the energy required for ozone generation (inversely proportional to baffling performance) for the three models studied (NW, HW and QW). Several important conclusions were reached from this analysis. First, it seen that the significance of energy consumption for driving the flow relative to the energy required for ozone generation becomes greater as more baffles are added to the contactor. Second, it is seen that the overall energy saving afforded by increasing the hydraulic efficiency (thus requiring less ozone generation) offsets the energy increase required for driving the flow through a more

hydraulically efficient contactor (characterized by more baffles). Overall, it is seen that energy considerations associated with contactor hydraulic efficiency (i.e. energy loss due to friction and energy required for ozone generation) should be considered when determining the operational costs of a water treatment plant.

6.2 Hydraulics Study of a Waste Stabilization Pond in Bolivia

6.2.1 Introduction

Wastewater stabilization ponds (WSPs) are a low cost and maintenance wastewater treatment system commonly used in areas where land is available and affordable, especially in developing countries (Mara 2004). Hydraulic performance of WSP is closely related to the level of pathogens removal, suspended solids removal, BOD (biochemical oxygen demand) removal and overall water quality performance through the WSP. Thus, improving the hydraulic performance of WSP is a primary goal of pond engineers and designers. CFD models have been successfully applied to system analysis and optimization of the hydraulics of WSPs (Wood et al. 1995; Wood et al. 1998; Peterson et al. 2000; Salter et al. 2000; Shilton 2000; Vega et al. 2003; Karteris et al. 2005; Sweeney et al. 2005; Verbyla et al. 2013). However, the predictions of CFD models on full-scale pond systems may be inaccurate due to lack of consideration of the physical conditions in the field, such as the sludge layer, transient flow rate changes, wind velocities, and temperature (Shilton et al. 2008). Sludge layer has been considered in recent studies based on CFD analysis of WSPs (Murphy 2012; Alvarado et al. 2012). Murphy (2012) investigated the impacts of sludge volume and distribution on hydraulic performance of a WSP in Australia using a 2-dimensional CFD model. Alvarado et al. (2012) studied the relationship between the flow pattern over time and the sludge accumulation in a large WSP in Ecuador using a 3-dimensional CFD model. The studies conducted by Murphy (2012) and Alvarado et al. (2012) imply that the

way the sludge layer affects hydraulic performance of a WSP depends on how sludge accumulates and distributes over time. For example, the way that sludge affects hydraulic performance in a WSP where sludge is mostly deposited near the edges (e.g. Murphy 2012) would be different from that in a WSP where sludge accumulates mainly near the inlet of the WSP (e.g. Alvarado et al. 2012). Thus, in order to further understand the relationship between sludge accumulation and distribution over time and hydraulic performance of a WSP, more studies should be conducted on WSPs with various sludge accumulation patterns. The WSP studied in this chapter has a unique sludge accumulation pattern that differs from the two WSPs mentioned earlier (Murphy 2012; Alvarado et al. 2012). In the current WSP, sludge deposits and forms a hill not far from the inlet.

In the present study, flow and tracer transport simulations are conducted on a WSP in Bolivia using a three-dimensional RANS model. This RANS model is validated via comparison with the experimental field data (Lizima 2012). This study also uses RANS simulation to predict the hydraulic performance of the WSP under a future sludge volume, which is estimated using a sludge accumulation prediction method. Numerical tracer studies on the pond with measured and future sludge layer geometries are conducted to analyze the impact of sludge changes over time on the hydraulic performance of the WSP.

6.2.2 Sludge Accumulation Prediction Method

An empirical method (Oakley 2005) is utilized to predict the accumulated sludge volume. This method utilizes the average flow into the WSP and the suspended solids concentration of the influent water to predict the volume of sludge via

$$V_L = 0.00156 \cdot Q_{av} \cdot SS \tag{6.1}$$

where V_L is the volume of sludge produced each year, m^3/year, Q_{av} is average flow, m^3/day, SS is suspended solids in the influent, mg/L.

To account for the future suspended solids concentration in the influent, an increased population calculated by the Malthus exponential model was utilized (Brauer and Castillo-Ch âavez 2011). The population growth rate used in the model was calculated based on the previous data. The pond influent water parameter (i.e. suspended solids mass loading per person) was kept at the average value of data collected from 2006 to 2012.

The predictions from the sludge volume prediction method (Oakley 2005) agree well with the measured data in 2012, shown in Table 6.5. The sludge volume for 2016 is predicted via this method. Using the predicted sludge volume for 2016, two different sludge layer geometries are generated based on different assumptions: 1) the first assumption is that the increment of sludge volume from 2012 to 2016 will mostly accumulate on top of the existing sludge. The height of sludge in this scenario is assumed to increase uniformly by the same percentage everywhere; 2) the second assumption is that the incoming sludge would deposit primarily in the flat area of the pond. The sludge increment is assumed to accumulate evenly everywhere throughout the pond except in the area where existing sludge measured in 2012 accumulated. The sludge profiles for 2016 based on the two assumptions are illustrated in Figure 6.10. Note that the assumed sludge layer geometries represent two extreme situations, where the actual sludge layer geometry should be an intermediate between these two distribution conditions. In addition to the two previously described sludge volume models, two other representations were considered: the sludge geometry measured by Lizima (2012) and a no-sludge case where the bottom of the WSP is flat. The scenarios considered are listed in Table 6.6.

6.2.3 Mesh and Numerical Tool

The sludge layer profile measured by Lizima (2012) is shown in Figure 6.11a. Based on the sludge layer profile, the computational domain or layout for scenario #2 is determined as shown in Figure 6.11b. The computational mesh shown in Figure 6.11b is refined near the walls and inlet/outlet. The total number of cells for the mesh is 620496. The meshes for the other scenarios summarized in Table 6.6 contained a similar number of cells.

Fixed flow rate boundary condition is used for the inflow at the inlet. That is, the volumetric flow rate at inlet is fixed as 66 m^3/day, which is an average flow rate during the period when physical tracer measurements of Lizima (2012) were conducted. This flow rate corresponds to a theoretical residence time of 27.65 days. Zero pressure boundary condition is imposed at the outlet. No-slip conditions are imposed at walls and sludge surface. Water surface is treated as a no-penetration, zero-shear, rigid lid allowing full slip. Thus, the corresponding surface boundary conditions are $\partial\langle u_1\rangle/\partial x_3 = \partial\langle u_2\rangle/\partial x_3 = \langle u_3\rangle = 0$ where $x_3\,(z)$ is the surface-normal direction and $\langle u_1\rangle$, $\langle u_3\rangle$ and $\langle u_2\rangle$ are the streamwise, surface-normal and spanwise velocities respectively (see coordinate system in Figure 6.11).

Once the steady state RANS solution of the flow is computed, the scalar advection-diffusion transport equation for the passive tracer in (3.22) is solved using the steady flow velocity. The numerical tracer study is conducted by initially releasing tracer with concentration $\langle C\rangle = 1$ at the inlet over a 1020-second or 17-min period which is around 0.04% of the theoretical residence time. At the outlet and at the walls, the normal gradients of $\langle C\rangle$ are set to zero indicating zero diffusive flux across these boundaries.

6.2.4 Results and Discussion

The CFD model under scenario #2 is validated via comparison with tracer concentration versus time from field measurements of Lizima (2012). As observed in Figure 6.12, the RTD curve predicted by CFD matches well with experimental data in terms of the location of primary peak and the following decaying tail. The primary peak of tracer concentration measured in the physical test occurs at around 1.09 days after the initial tracer release while that in the CFD simulation is 1.21 days. The relative error is approximately 11%. Furthermore the portion of the tail of the curve predicted by CFD is in excellent agreement with the physical measurement between the 6^{th} and 12^{th} day.

In WSPs, hydraulic performance is determined by the mean residence time (MRT). For the type of WSP considered here, the longer the MRT is, the better the hydraulic performance is. There are two primary factors that affect MRT: short-circuiting and theoretical residence time (Peterson 2000). The following discussion will analyze the impact of sludge layer geometries on hydraulic performance of WSP in terms of short-circuiting and theoretical residence time.

In this section, results from flow and tracer transport simulations are presented for the four scenarios listed in Table 6.6. Recall that scenario #1 corresponds to the WSP in 2006 when no sludge existed in the WSP. Scenario #2 corresponds to the WSP in 2012 for which the geometry of the sludge layer was represented following the field measurements of Lizima (2012). Scenarios #3 and #4 correspond to the projected sludge layer profiles in the WSP in 2016.

Figure 6.13 shows water flow speed contours on *x-y* (horizontal) planes at depths of 0.69m and 0.10 m from the water surface. Note that the 0.69 m depth corresponds to the depth of the inlet and outlet for the four scenarios. At 0.69 m depth (Figures 6.13a-d), a high speed jet flow can be found emanating from the inlet in all four scenarios, as expected. However, the

sludge in scenarios #2, 3, and 4 blocks the jet flow and forces it to change path. Although the jet flows in these scenarios are impeded, the jet flows can still travel for a certain distance at a relative high speed compared to the jet flow in scenario #1 for which no sludge layer is present. The high speed jet flow in all scenarios establishes a highway from inlet to outlet giving rise to short-circuiting. This short-circuiting flow can transport particles, such as dye tracer and pathogens, much faster than the flow in other parts of the pond.

Similar high speed jet flows can be found in all four scenarios at 0.1 m depth (Figures 6.13e-h). Comparing Figure 6.13e and f, it can be observed that the jet flow in scenario #2 (Figure 6.13f) is more intense than that in scenario #1 (Figure 6.13e). At 0.10 m depth, the accumulated sludge in scenario #2 serves to enhance the jet relative to the no-sludge case (scenario #1). This occurs because the sludge in scenario #2 is not tall enough to force the flow to go around it; instead, the flow goes over the sludge where the cross-sectional area is approximately 30% of that of the origin cross-section without sludge. Thus, the flow is accelerated when it passes over the sludge consistent with Bernoulli's principle. Figure 6.13g shows that in scenario #3, the flow is not able to go over the sludge and has to go around the sludge. The reason for this is that the sludge in scenario #3 reaches over 90% of the total depth of the pond at its peak location. In this case, the sludge blocks the flow similar to a baffle. Differences in the impact of the sludge in scenarios #2 and #3 can be clearly seen in the comparison of streamlines (Figure 6.14b and c).

Figures 6.13h, f show that the jet path in scenario #4 is similar to that in scenario #2. Recall that the sludge layer in scenario #4 has the same sludge mountain as that in scenario #2 but an increased sludge height for the rest area. The difference between Figures 6.13f and h is that in the latter, the jet is more damped after passing the sludge. This indicates that the flow

short-circuiting in scenario #4 is weaker than that in scenario #2. As seen from the streamlines in Figures 6.14b and d, the flow in scenario #2 forms a large recirculation zone past the sludge unlike in scenario #4. In scenario #4, as the jet moves past the sludge, it spreads out over a wide region and consequently its speed is reduced dramatically. This gives rise to weaker short-circuiting in scenario #4 compared to scenario #2. Overall analysis of Figures 6.13 and 6.14 indicates that short-circuiting is most intense in scenario #2.

Figure 6.15 shows snapshots of tracer concentration on the *x*-*y* (horizontal) plane at 0.69m depth at 0.5, 2.0, and 4.0 days after initial tracer release. Recall that the tracer is initially released with concentration $\langle C \rangle = 1$ at the inlet for a 17-min period. At 0.5 day after initial release, the concentrated tracer patch is broken up by the sludge obstruction. At 2.0 days after initial release, the tracer in scenario #2 has already reached the outlet, unlike in the other scenarios. This is consistent with Figures 6.13 and 6.14 showing stronger short-circuiting in scenario #2 compared to the other scenarios. Finally note that the highly concentrated tracer patches observed 0.5 day after initial tracer release become diluted over time due to diffusion.

Figure 6.16a compares RTDs predicted by the simulations of the different scenarios. A primary peak can be found in all four curves. The time at which the primary peak occurs is mainly determined by the intensity of short-circuiting. Scenario #2 possesses the strongest short-circuiting as concluded earlier, followed by scenarios #1, 4 and 3, respectively. To further investigate the hydraulic performance of the WSP, cumulative residence time distributions (shown in Figure 6.16b) are generated based on the data in Figure 6.16a.

The short-circuiting indices (S) for the four scenarios are estimated from Figure 6.16b and are listed in Table 6.7. The short-circuiting index *S* was defined in Chapter 3 (see Eqn. 3.30) and is inversely proportional to the strength of short circuiting. As expected from previous

analysis, the value of *S* is smallest for scenario #2. Values of *S* for scenarios #3 and #4 are 0.384 and 0.209 respectively. Recall that scenarios #3 and #4 are two assumed extreme projections of sludge accumulation for 2016. Thus, the actual short-circuiting index for 2016 should be somewhere between 0.209 and 0.384 depending on the actual sludge distribution. Furthermore, the value of *S* is higher in scenarios 3 and 4 than in scenarios 1 and 2. The reason for this is that as the sludge builds up in the pond, the sludge begins to induce a baffling effect thereby reducing the strength of short-circuiting (as observed earlier in terms of fluid speed contours and streamlines) ultimately serving to improve the hydraulic performance of the pond. Although an increase in sludge may seem beneficial, such an increase eventually reduces the water volume of the pond sufficiently to decrease the theoretical residence time, as shown in Table 6.7. For example, although the short-circuiting index in scenario #4 is higher than that in scenario #1 (suggesting that the former has better hydraulic performance) the theoretical residence time is lower in scenario #4 than that in scenario #1 due to the decrease in water volume. A lower theoretical residence time in scenario #4 suggests that suspended solids in the WSP would have less time to settle to the floor before being carried out of the pond by the flow.

Overall, these findings have confirmed that sludge distribution and volume have a significant impact on hydraulic performance as noted in a previous study (Murphy 2012).

6.2.5 Conclusions

RTD predicted by the present CFD model matches well with the data measured in field by Lizima (2012), demonstrating that CFD can be a useful and efficient tool for the evaluation of the hydraulic performance of a WSP.

CFD studies based on future predictions of sludge accumulation revealed that an increase of sludge volume can initially decrease the hydraulic performance of a WSP. As the sludge

accumulates further, it can actually begin to serve as a baffle thereby improving hydraulic performance. However, eventually the sludge accumulation reduces the volume of the pond serving to lower mean residence time which is undesirable.

This study has found that sludge distribution is critical for determining hydraulic performance of a WSP. However, sludge distribution change over time is still not well understood. Better understanding of sludge accumulation could be obtained using a more advanced CFD model, such as a liquid-solid two phase flow model. An alternative approach would be the continued used of single-phase CFD as was the case here aided by physical measurements of sludge distribution in ponds with typical (standard) configurations. It is recommended that pond builders measure sludge accumulation over time in standard pond configurations. Based on these measured sludge distributions, CFD can be used to evaluate the hydraulic performances of these typical ponds over time. This information could be tabulated and provided to pond managers to better determine the current and future hydraulic performance of the pond they are running or would like to build.

6.3 Chapter Summary

In this chapter, the computational framework developed in this dissertation has been successfully applied to studies of the baffling performance and energy loss of three baffled ozone contactor configurations and the hydraulic performance of a wastewater stabilization pond. Summaries of the main conclusions derived from these applications were provided in sub-sections 6.1.4 and 6.2.5. These successful applications serve as examples of how the present framework can be used to provide important and novel analysis of water and wastewater treatment systems.

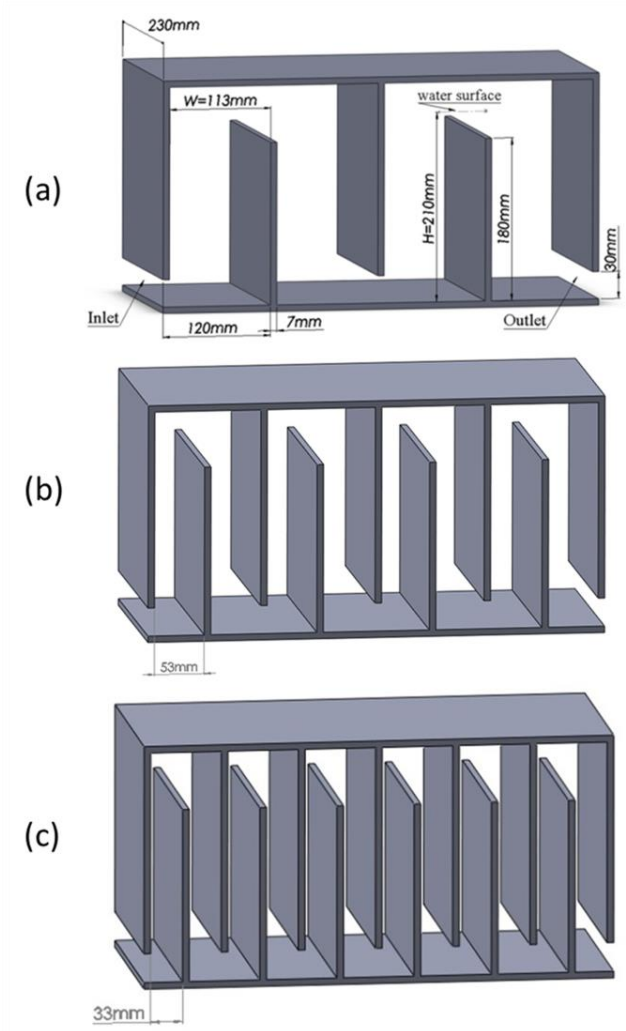

Figure 6.1: Layout of the three model ozone contactors investigated in this study with (a) normal chamber width (NW) (b) half chamber width (HW) (c) quarter chamber width (QW).

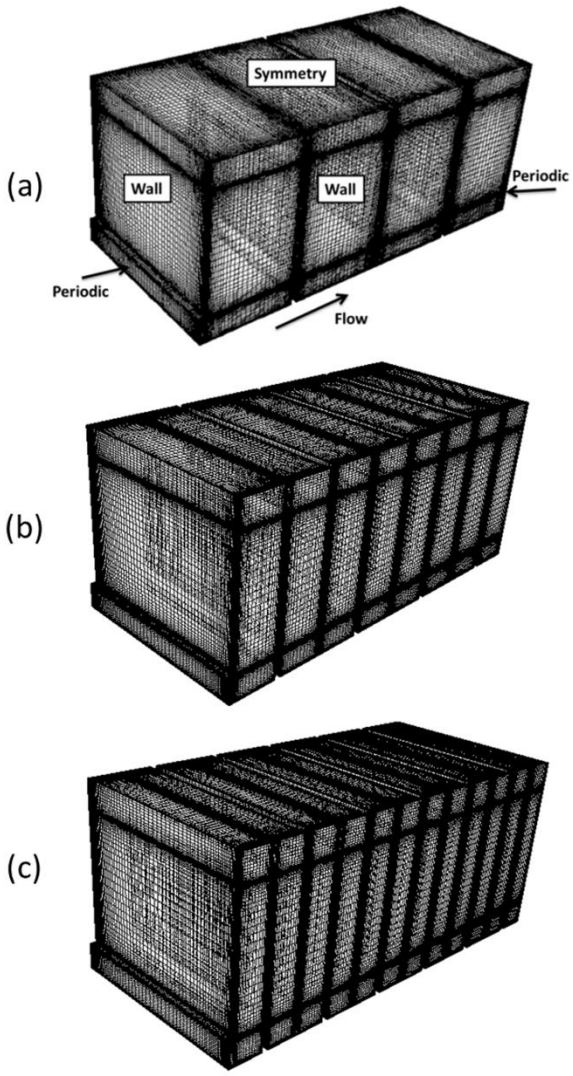

Figure 6.2: Grids employed in RANS of contactors with (a) normal chamber width (NW) (b) half chamber width (HW) (c) quarter chamber width (QW).

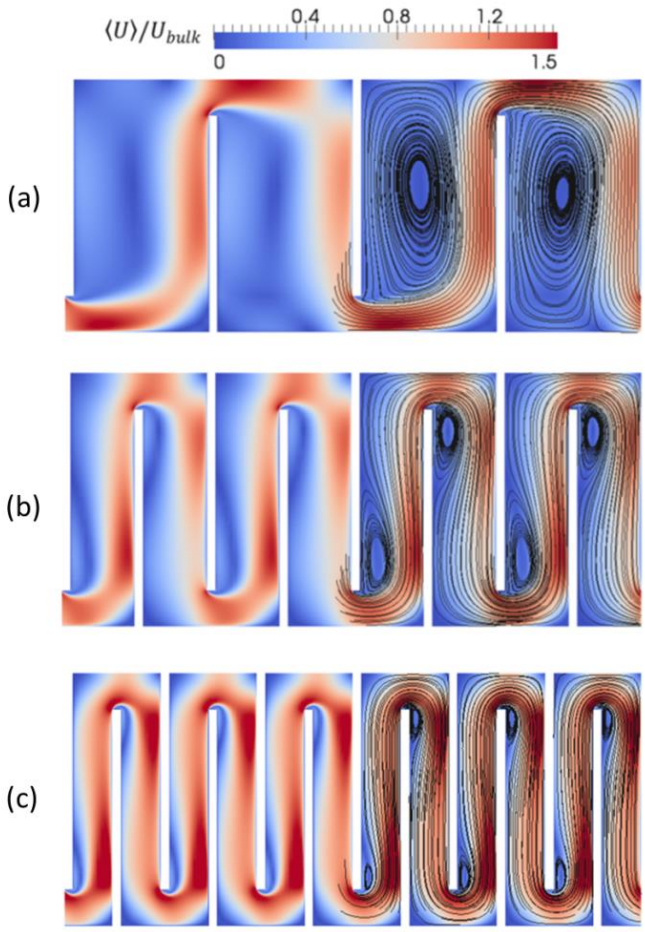

Figure 6.3: Absolute velocity superimposed with corresponding streamlines (in last two chambers) in RANS for (a) NW model, (b) HW model and (c) QW model. Velocity and streamlines are shown on the *x*-*y* plane at mid span ($z = L/2$).

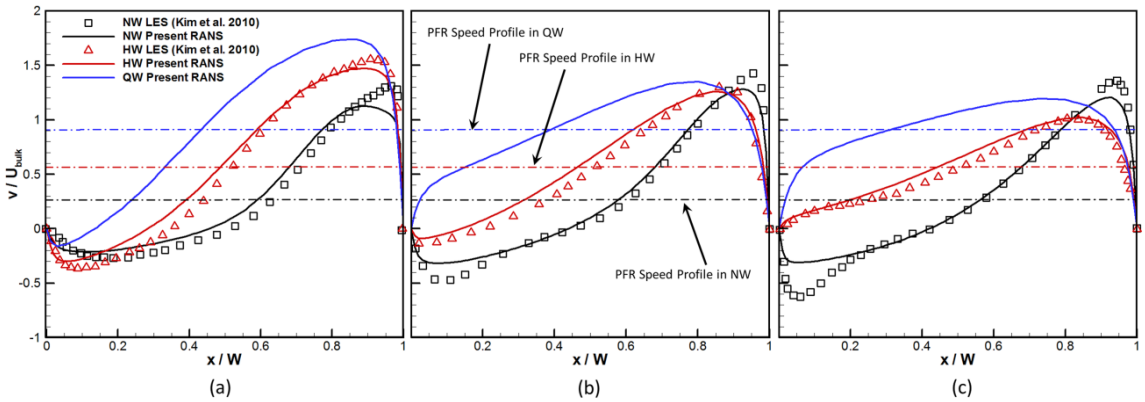

Figure 6.4: *y*-velocity profiles across the chamber width (W) along x at different depths: (a) $y/H = 0.27$; (b) $y/H = 0.50$; (c) $y/H = 0.72$.

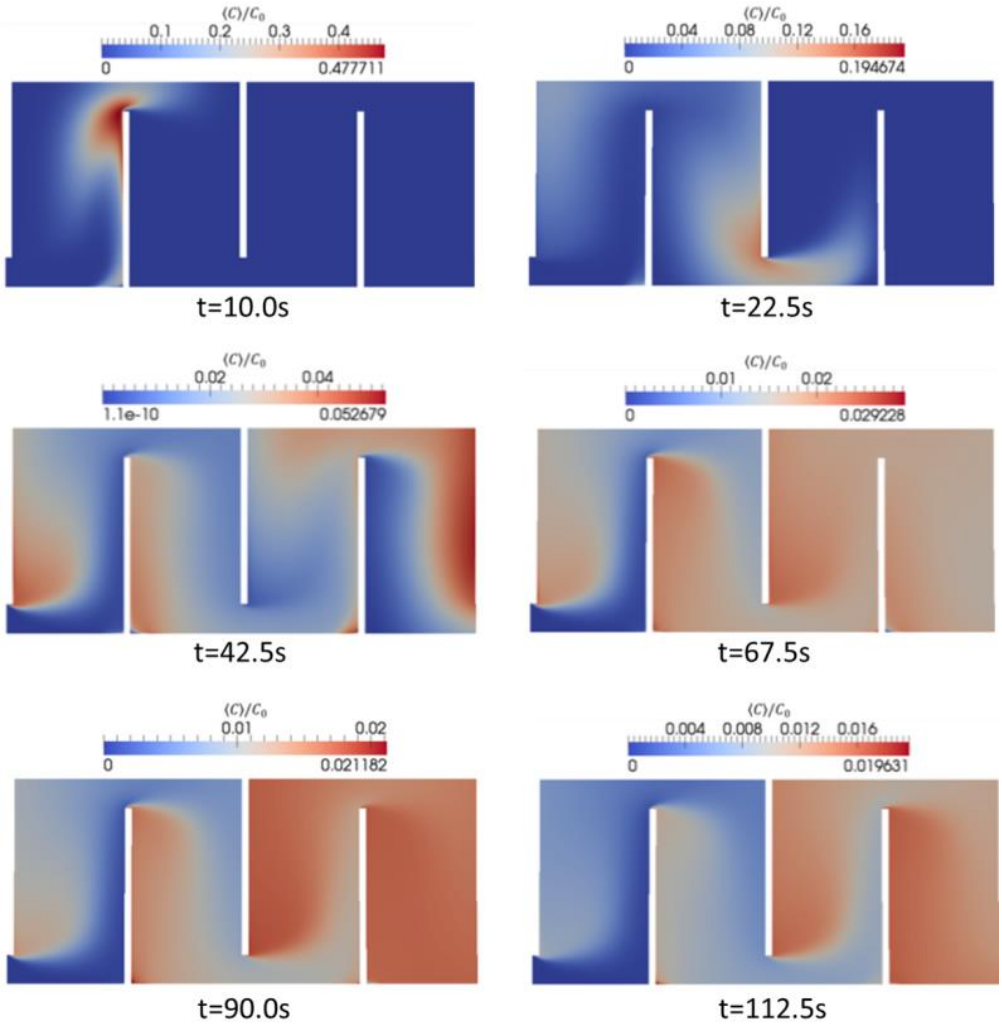

Figure 6.5: Normalized tracer concentration (tracer concentration/initial tracer concentration) snapshots at t = 10.0, 22.5, 42.5, 67.5, 90.0 and 112.5 s in RANS of NW model. Concentration is shown on the x-y plane at mid span ($z = L/2$).

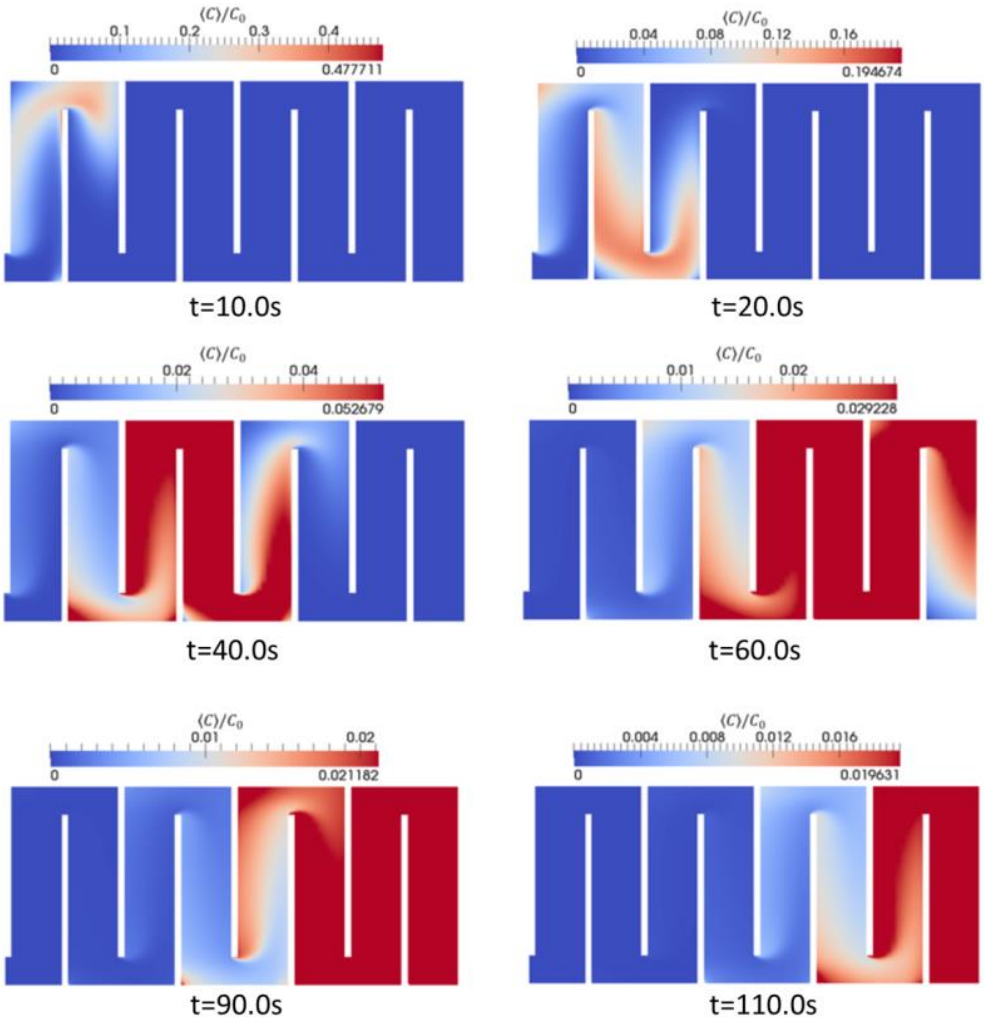

Figure 6.6: Tracer concentration snapshots at t = 10.0, 20.0, 40.0, 70.0, 90.0 and 110.0 s in RANS of HW model. Concentration is shown on the x-y plane at mid span ($z = L/2$).

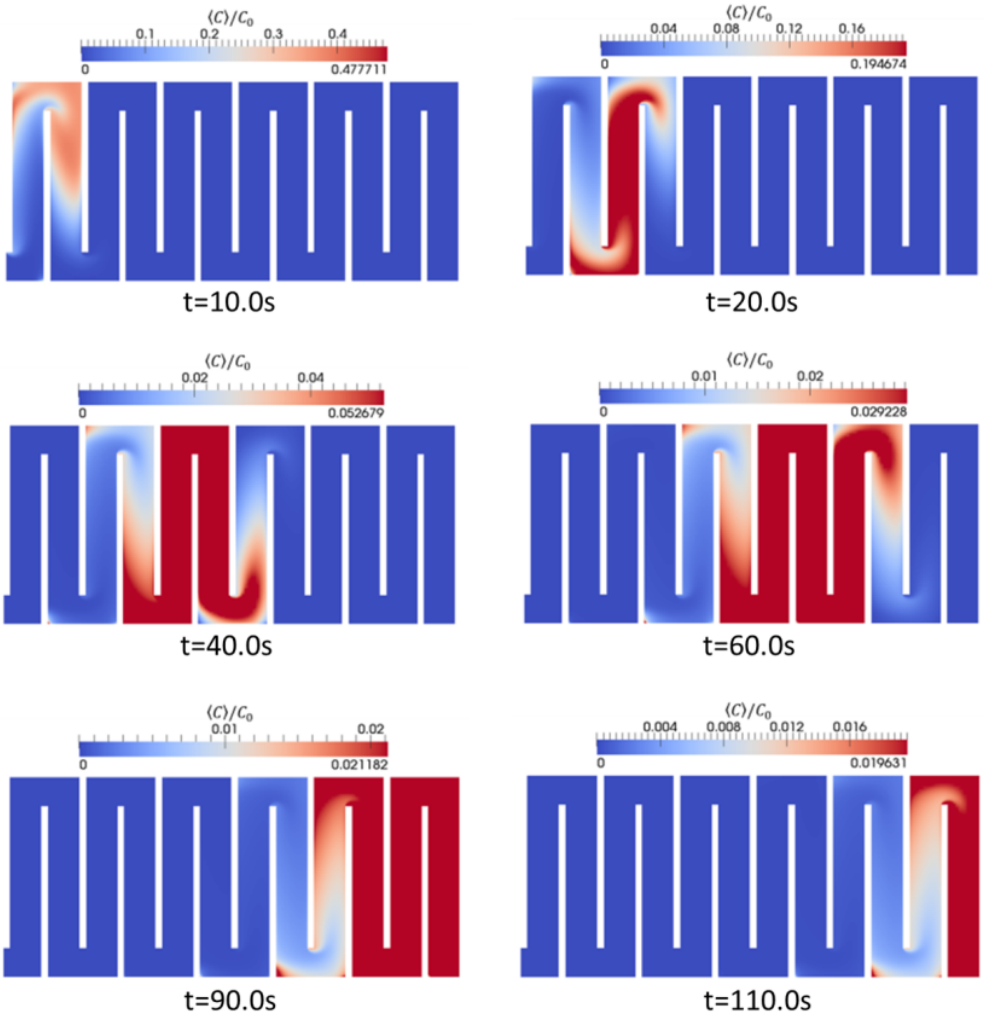

Figure 6.7: Tracer concentration snapshots at t = 10.0, 20.0, 40.0, 70.0, 90.0 and 110.0 s in RANS of QW model. Concentration is shown on the x-y plane at mid span ($z = L/2$).

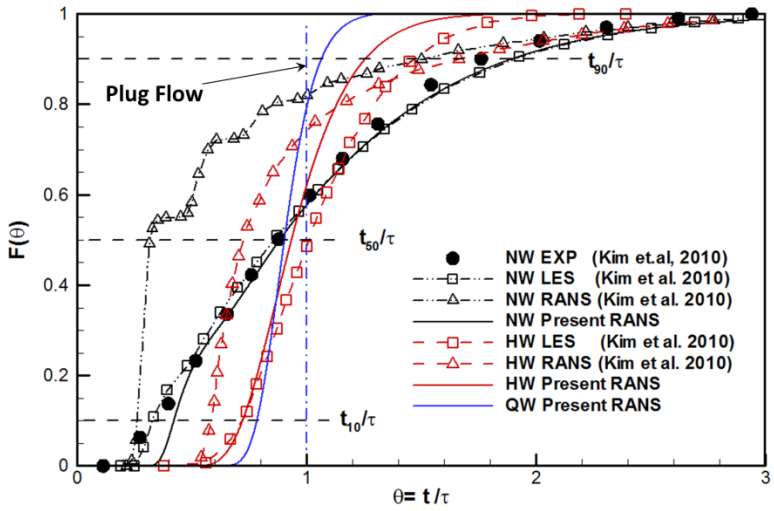

Figure 6.8: Comparison of cumulative residence time distributions.

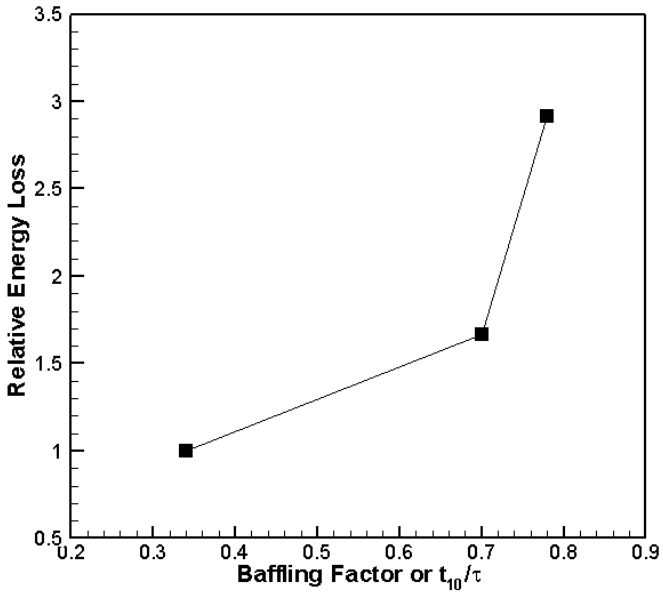

Figure 6.9: Relationship between relative energy loss due to friction and baffling factor.

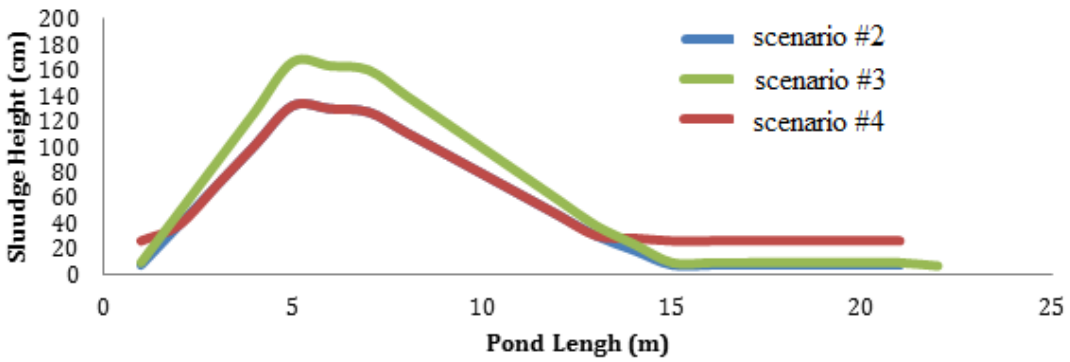

Figure 6.10: Two-dimensional perspective of the sludge profiles studied.

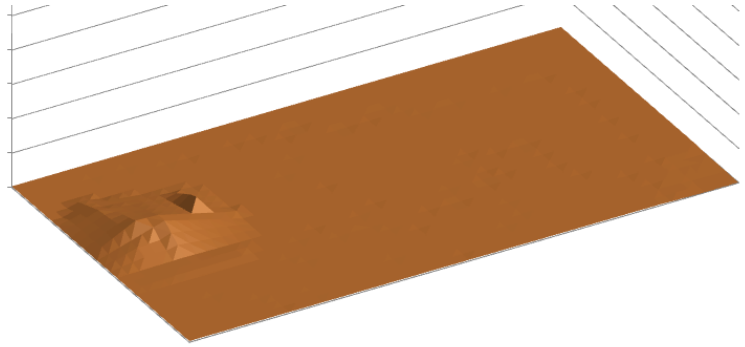

(a)

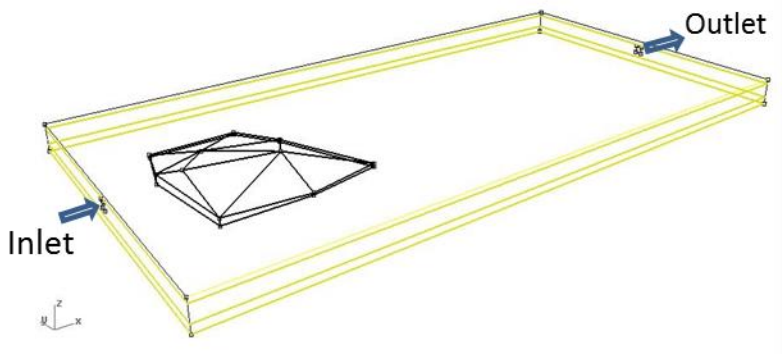

(b)

Figure 6.11: (a) Sludge layer profile in 2012, (b) layout, and (c) computational mesh of the pond in Bolivia.

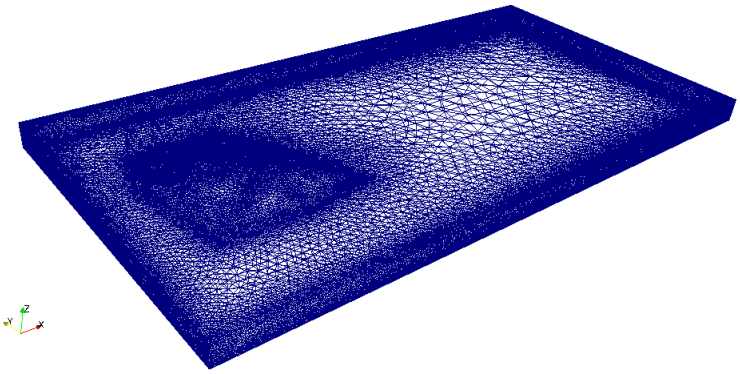

(c)

Figure 6.11 (Continued)

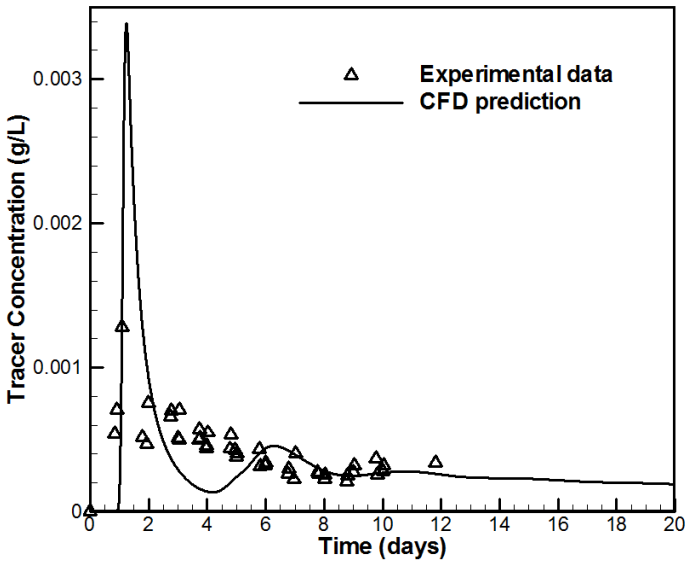

Figure 6.12: Comparison of tracer concentration versus time from experiment and CFD simulation.

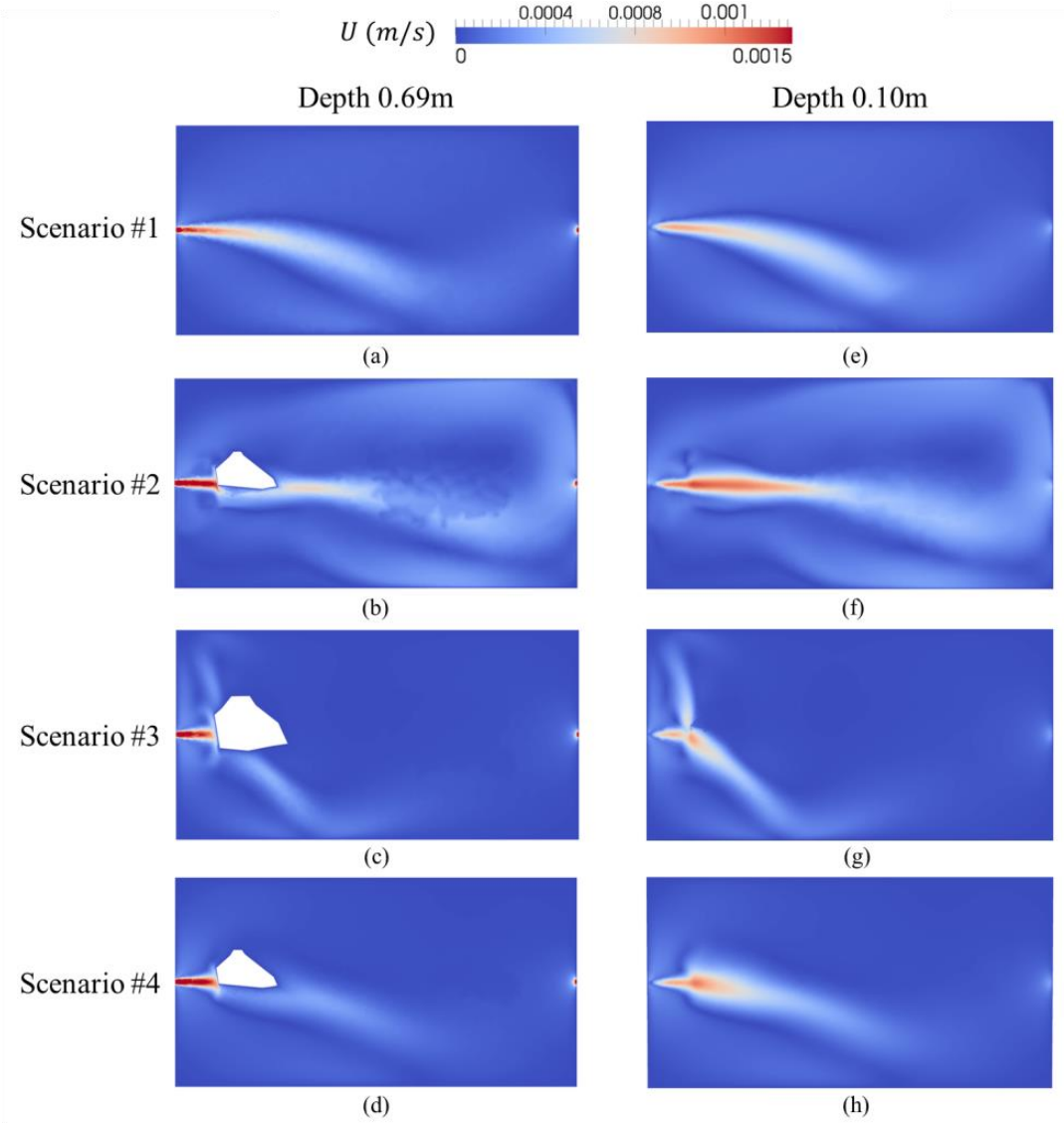

Figure 6.13: Water flow speed contours on *x-y* (horizontal) planes at depth = 0.69m (corresponding to the depth of the inlet) and depth = 0.10m from water surface. In (a)-(d), the sludge is color-coded white.

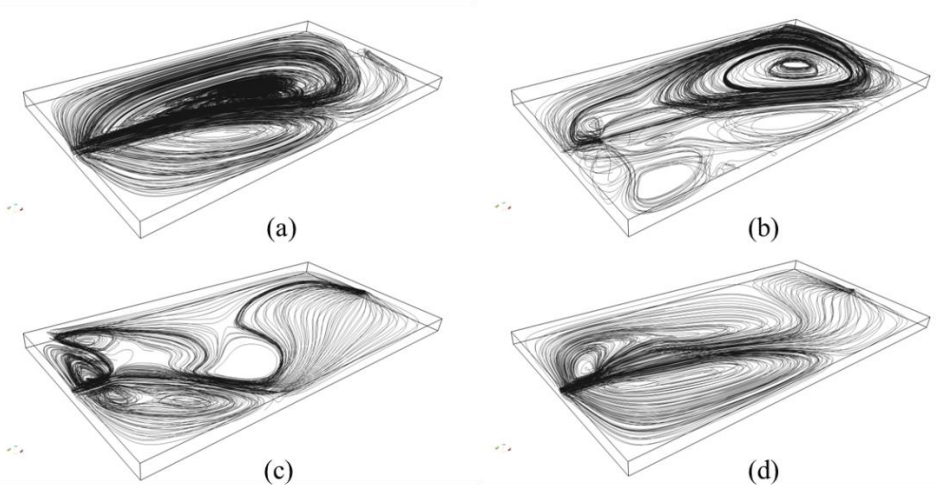

Figure 6.14: Streamlines for different scenarios (a) scenario #1; (b) scenario #2; (c) scenario #3; (d) scenario #4.

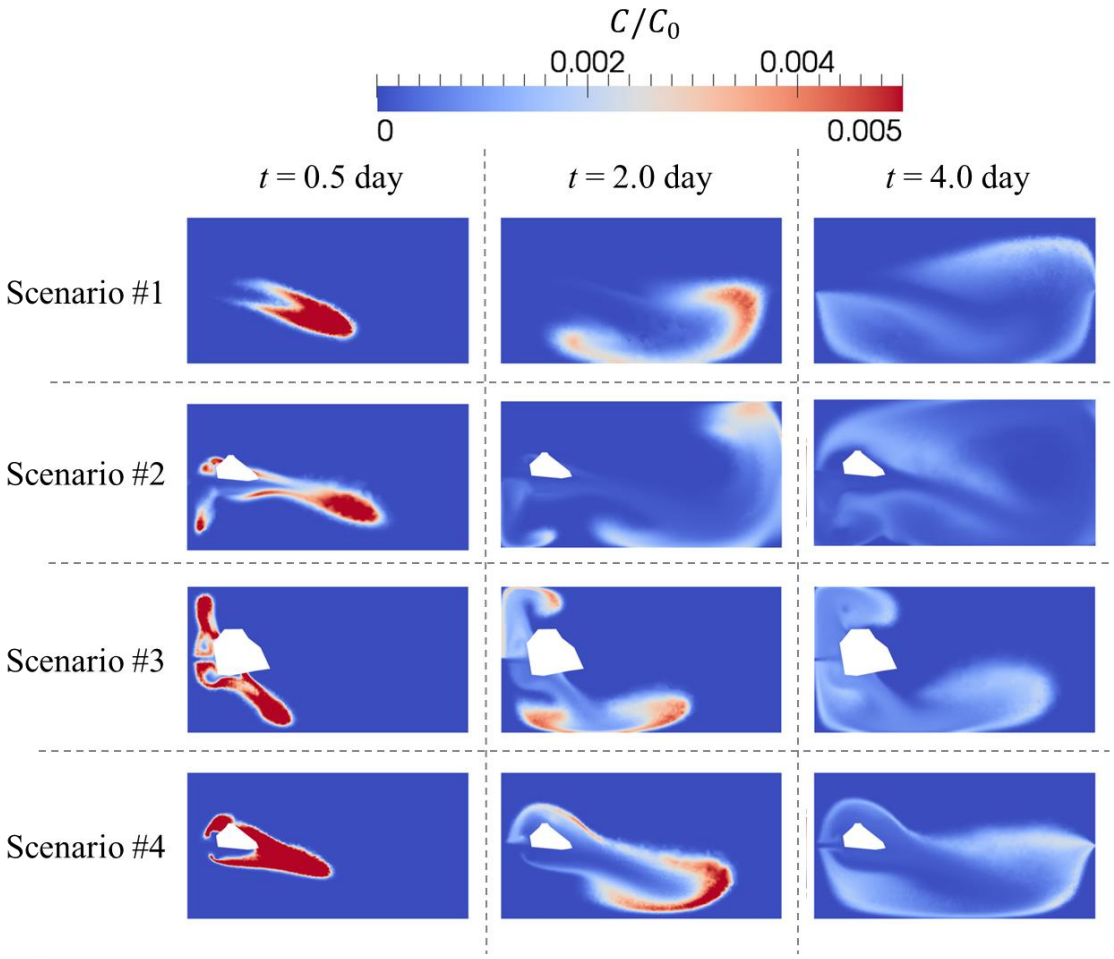

Figure 6.15: Snapshots of normalized tracer transport on the *x-y* (horizontal) plane at 0.69m depth at different times (t = 0.5, 2.0, and 4.0 days).

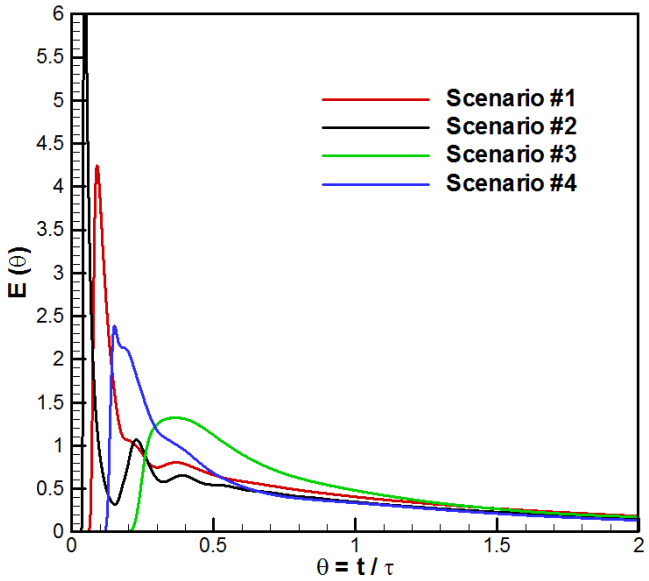

(a)

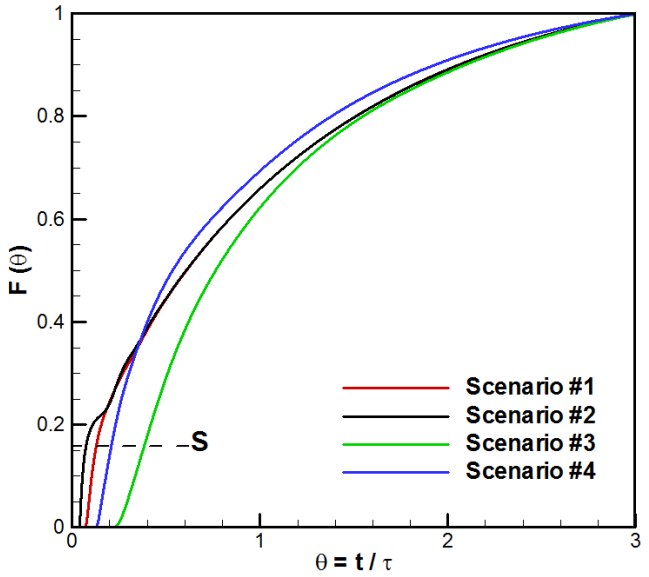

(b)

Figure 6.16: Comparison of (a) RTDs and (b) cumulative RTDs predicted by simulations.

Table 6.1: Relative error with respect to experimental results (Kim et al. 2010a) for NW model.

	t_{10}/τ	Error	t_{50}/τ	Error	t_{90}/τ	Error
EXP (Kim et al. 2010a)	0.334	-	0.875	-	1.74	-
LES (Kim et al. 2010b)	0.300	10.2%	0.856	2.2%	1.900	9.2%
RANS (Kim et al. 2010b)	0.220	34.1%	0.317	63.8%	1.505	13.5%
Present RANS	0.421	26.0%	0.880	0.6%	1.930	10.9%

Table 6.2: Relative error with respect to LES results (Kim et al. 2010b) for HW model.

	t_{10}/τ	Error	t_{50}/τ	Error	t_{90}/τ	Error
LES (Kim et al. 2010b)	0.700	-	1.010	-	1.468	-
RANS (Kim et al. 2010b)	0.580	17.1%	0.725	28.2%	1.660	13.1%
Present RANS	0.720	2.9%	0.934	7.5%	1.255	14.5%

Table 6.3: Baffle classification and energy loss estimation.

	Baffling Factor or θ_{10}	Classification (U.S. EPA based on θ_{10})	Relative Energy Loss
NW	0.334	Poor	1.0
HW	0.700	Superior	1.7
QW	0.780	Superior	2.9

Table 6.4: Comparison of energy consumption by driving flow and ozone generation. Total energy consumption for a plant is taken as 1.4kWh/1000 gallons or 0.37kWh/m^3.

Model	Energy for driving flow / kWh/m^3	Hydraulic efficiency	Energy for ozone generation / kWh/m^3		Sum of energy for driving flow and ozone generation / kWh/m^3			
			Scenario I	Scenario II	Scenario I	Percentage of total energy consumption rate	Scenario II	Percentage of total energy consumption rate
NW	1.20E-03	0.334	0.0288	0.1305	3.00E-02	8.1%	1.32E-01	35.6%
HW	2.00E-03	0.700	0.0137	0.0623	1.57E-02	4.3%	6.43E-02	17.4%
QW	3.50E-03	0.780	0.0123	0.0559	1.58E-02	4.3%	5.94E-02	16.0%

Table 6.5: Comparison of predicted sludge volume and measured data in 2012.

Year	Measured data (units: m^3)	The Oakley (2005) sludge volume prediction method (units: m^3)
2012	154	164
2016	N/A	326

Table 6.6: Summary of scenarios considered in this study.

Scenario	Corresponding year	Sludge volume / m^3	Sludge geometry
#1	2006	0	N/A
#2	2012	154	Measured
#3	2016	326	Based on assumption 1
#4	2016	326	Based on assumption 2

Table 6.7: Comparison of short-circuiting indices.

Scenario	S	Theoretical residence time θ	Mean residence time (based on integrating over 2.5θ)
#1	0.129	29.98	22.93
#2	0.074	27.65	21.89
#3	0.384	25.04	24.86
#4	0.209	25.04	20.36

CHAPTER 7: CONCLUSIONS AND FUTURE WORKS

Modeling approaches have been employed to predict pathogen removal in disinfection tanks for decades. The capability of predicting hydraulic and disinfection efficiencies of ozone disinfection contactors is essential for evaluating existing contactors and improving future designs. The U.S. EPA regulations of disinfection by-products (e.g. $10\,\mu g.L^{-1}$ for bromate since 2001) have made modeling even more important for the management of ozone disinfection process.

Early models have been based on mass balance while ignoring flow behavior, such as the axial dispersion reactor (ADR) model (Chen 1998; Kim et al. 2002; Kim et al. 2007) and the back flow cell model (BFCM) (Nguyen-Tien et al. 1985). These models have been successfully applied to contactors with a simple geometry but have usually failed for contactors with complex geometries. In addition, these models usually have empirical inputs, which would increase the uncertainty of predictions.

Compartmental models or systematic networks have been developed to provide a flow solution for the simulation of tracer transport or reaction process (Gresch et al. 2009; Mandel et al. 2012). These models are essentially a combination of the completely mixed flow reactor (CMFR) and the plug flow reactor (PFR). However, compartmental models have relative low spatial resolution of the flow, thus potentially leading to lower accuracy. Additionally, compartmental models are unable to respond to varying flow conditions, thereby rendering them not practical for prediction. For example, a change in flow rate could potentially affect the size of

dead zone regions or strength of short-circuiting. However, the compartmental model would not be able to detect this.

At the end of the 1990s, researchers started to develop computational frameworks based on CFD (Cockx et al. 1999; Falconer and Ismail 1997; Hannoun et al. 1998; Wang and Falconer 1998). A CFD-based framework for ozonation process is divided into two parts: (1) flow simulation and (2) reaction process modeling. In the first part, one main question is whether the flow in the ozone contactor should be modeled in a single phase or in multiple phases. In reality, gas phase exists in the water flow, thus, a multi-phase flow simulation would be more accurate than a single-phase flow, but this would come with higher computational cost. If the gas phase in the disinfection process can be neglected, the simulation could be simpler and consequently the computational cost could be reduced. Bolaños et al. (2008) pointed out that the single-phase Navier-Stokes equations could be applied to simulate ozonation processes if the gas phase portion is small. As is the case here, a majority of the studies have treated the flow in ozone contactors as a single-phase flow (Huang et al. 2004; Hofman et al. 2007a; Wols et al. 2008a; Kim et al. 2010a; Amini et al. 2011; Zhang et al. 2013a, b) with only a few using multi-phase flow (Cockx et al. 1999; Ta and Hague 2004; Bartrand et al. 2009; Talvy et al. 2011). Another question in the flow simulation is: which solution methodology is suitable to simulate the flow? RANS simulation has been the more popular methodology since the onset of CFD-based framework for ozonation. Recently, Kim et al. (2010a) pointed out that RANS may yield poor performance in terms of tracer transport predictions, such as t_{10}. As a result, LES was proposed as a more accurate alternative to RANS. However, this dissertation has revisited the numerical and experimental studies by Kim et al. (2010b) and found that the poor performance of RANS may be due to the inappropriate use of the turbulence model (see Chapter 4). For a fine grid

resolving wall viscous boundary layers, RANS with a low-Reynolds number turbulence model such as the Lauder-Sharma k-ε model was demonstrated to be more accurate than RANS with the standard k-ε model (Zhang et al. 2013a and Chapter 4) for predicting hydraulic performance. On coarse grids, the standard k-ε model was shown to lead to accurate prediction of hydraulic performance. The difference between the Lauder-Sharma k-ε model and the standard k-ε model is that the former integrates the turbulence model equations all the way to the wall, which is required if resolving wall viscous boundary layers. The standard k-ε model is not equipped to do this and thus leads to poor results when used with wall-resolving grids. Overall, RANS performs on par with LES in simulating flow and tracer transport in baffled contactors because the eddies responsible for determining hydraulic performance are quasi-steady thus well-represented by RANS. In flows disinfection systems such as a column contactor, flow features such as spatial transition to turbulence are not well-represented by RANS and thus RANS is not able to perform on par with LES in predicting hydraulic performance.

Based on the previously described encouraging results, a modeling framework for the ozonation process was developed by combining RANS with kinetics-based reaction modeling for the first time. This computational framework was applied to the full-scale ozone contactor operated by the City of Tampa Water Department (Zhang et al. 2014 and Chapter 5). Flow fields, residence time distribution, ozone concentration distribution, and contact time (CT) distribution within the contactor were predicted via the newly developed computational framework. The predictions of ozone concentrations at sample points were shown to agree well with physical experimental data measured in the contactor. Although bromate concentrations at sample points were underestimated, they are on the same order as the physical data. Potential reasons for this were the neglect of radical pathway for bromate formation and the assumption that the

turbulence-chemistry interaction is characterized by slow chemistry rather than finite-rate chemistry. Another potential reason for underestimation of bromate formation was the lack of information about the competition between hypobromous acid (HOB_r) and bromate ($B_rO_3^-$) for available hypobromite (B_rO^-). Thus the amount of B_rO^- available for $B_rO_3^-$ formation is uncertain. Finally, the predicted CT values at the contactor outlet demonstrated that the disinfection performance of the ozone contactor is sufficient to meet regulation requirements. Furthermore, the impact of seasonal flow rate change on disinfection performance was found to be significant and deserves attention during the management and operation of a water treatment plant.

As noted above, a limitation of the current framework is that the turbulence-chemistry interaction is modeled as slow chemistry, excluding the possibility of finite-rate chemistry. Future research should be performed in order to develop models allowing for finite-rate reactions in water disinfection systems.

The modeling framework developed in this dissertation was successfully applied to study the hydraulic efficiency and energy loss in baffled ozone contactor configurations and the hydraulic performance of a wastewater stabilization pond with sludge. In the case of baffled contactors it was shown for the first time that increasing baffling efficiency by increasing the number of baffles leads to significant energy loss due to friction. However, this energy loss is off-set by energy savings resulting from the increased baffling efficiency and associated lower ozone demand.

In the case of the wastewater stabilization pond, CFD showed that both sludge volume and sludge distribution can impact the pond's hydraulic performance. Sludge can either deteriorate or improve hydraulic performance of wastewater stabilization ponds depending on

the distribution pattern of the sludge. Thus it is recommended that pond builders/designers should study sludge accumulation in their ponds in order to accurately predict future hydraulic performance of the ponds via CFD and thus provide a better guide for pond managers. This approach could be made practical if studies are made for standardized pond configurations. CFD may be extended to study a number of issues of importance to water and wastewater disinfection. In future research, the following topics are recommended:

- Increase disinfectant utilization efficiency by changing reactor configurations and rearranging diffusers. Estimate the operational cost for different scenarios and find the minimum cost.
- Studies on the energy costs/savings incurred by disinfection approaches. Disinfection is an energy-consuming technology. For example, ultraviolet (UV) disinfection has a high consumption of electricity for UV lighting; ozone disinfection has a high level of electricity use for ozone generation.
- Applications to emerging disinfection technologies: disinfection by pulsed arc electrohydraulic discharge (Ching et al. 2001), ultrasound disinfection (Hoyer 2002) and combined oxidants disinfection, such as UV and chlorine (Lotierzo et al. 2003) and ultrasound and chlorine (Plummer et al. 2002).

REFERENCES

[1] Alvarado, A., Sanchez, E., Durazno, G., Vesvikar, M., and Nopens, I. (2012). CFD analysis of sludge accumulation and hydraulic performance of a waste stabilization pond. Water Sci. Technol. 66(11), 2370-7.

[2] Amini, R., Taghipour R., and Mirgolbabaei H. (2011). Numerical assessment of hydrodynamic characteristics in chlorine contact tank. International Journal for Numerical Methods in Fluids, 67(7), 885-898.

[3] Audenaert, W. T. M., Callewaert, M., Nopens, I., Cromphout, J., Vanhoucke, R., Dumoulin, A., Dejans, P., and Van Hulle, S.W.H. (2010). Full-Scale Modeling of an Ozone Reactor for Drinking Water Treatment. Chem. Eng. J., 157(2–3), 551–557.

[4] Baldyga, J., and Bourne, J. R. (1989). Simplification of micromixing calculations, Chem. Eng. J., 42, 83.

[5] Bartrand, T. A. (2006) High resolution experimental studies and numerical analysis of fine bubble ozone disinfection contactors (Doctoral dissertation). Available from ProQuest Dissertations & Theses database. (UMI No. 3239812).

[6] Bartrand, T. A., Farouk, B., and Haas, N. C. (2009). Countercurrent gas/liquid flow and mixing: Implications for water disinfection. International Journal of Multiphase Flow 35(2), 171-184.

[7] Berglund, M., Fureby, C., Sabel'nikov, V., and Tegner, J. (2008). On the Influence of Finite Rate Chemistry in LES of Self-Ignition in Hot Confined Supersonic Airflow, European Space Agency Special Report ESA SP-659.

[8] Bolaños, E. Q., Ocampo, J. T., and Rodríguez, L. C. (2008). Applicability of computational fluid dynamics to simulate ozonation processes. Ingeniería y Desarrollo, 24, 97-116.

[9] Bolton, J. R. (2000), Calculation of Ultraviolet Fluence Rate Distributions in an Annular Reactor: Significance of Refraction and Reflection, Water Research, 34(13), 3315-3324.

[10] Brauer, F., and Castillo-Châvez, C. (2011). Mathematical models in population biology and epidemiology. Springer.

[11] Canada Ministry of Health and Long-Term Care (2008). Procedure for Disinfection of Drinking Water in Ontario. Ministry of Health and Long-Term Care. Avaliable at, http://www.ontla.on.ca/library/repository/mon/23005/292233.pdf.

[12] Carlson, K., Bellamy, W., and Ducoste, J. (2001). Implementation of the Integrated Disinfection Design Framework, American Water Works Association.

[13] Chen, C. M. (1998). Modeling drinking water disinfection in ozone bubble-diffuser contactors (Doctoral dissertation). Available from ProQuest Dissertations & Theses database. (UMI No. 9914465).

[14] Chen, J., Deng, B., and Kim, C. N. (2011). Computational fluid dynamics (CFD) modeling of UV disinfection in a closed-conduit reactor. Chemical Engineering Science, 66(21): 4983-4990.

[15] Ching, W. K., Colussi, A. J., Sun, H. J., Nealson, K. H., and Hoffman, M. R. (2001). Escherichia coli Disinfection by Electrohydraulic Discharges. Environmental Science and Technology, 35, 4139-4144.

[16] Chiu, K., Lyn, D. A., Savoye, P., and Blatchley, E. R. (1999). Integrated UV disinfection model based on particle tracking. Journal of Environmental Engineering, 125 (1), 7–16.

[17] Cockx, A., Line, A., Roustan, M., Do-Quang, Z., and Lazanova, V. (1997). Numerical simulation and physical modelling of the hydrodynamics in an air-lift internal loop reactor. Chemical Engineering Science, 52(21/22), 3787-3793.

[18] Cockx, A., Do-Quang, Z., Line, A., and Roustan, M. (1999). Use of computational fluid dynamics for simulating hydrodynamics and mass transfer in industrial ozonation towers. Chem. Eng. Sci., 54(21), 5085–5090.

[19] Colin, O., Ducros, F., Veynante, D., and Poinsot, T. (2000). A Thickened Flame Model for Large Eddy Simulations of Turbulent Premixed Combustion. Physics of Fluids, 12: 1282–1284.

[20] Correa, S. M. (1993). Turbulence-chemistry interactions in the intermediate regime of premixed combustion. Combustion and Flame, 93(1-2), 41-60.

[21] Craig, K., De Traversay, C., Bowen, B., Essemiani, K., Levecq, C., and Naylor, R. (2002). Hydraulic study and optimisation of water treatment processes using numerical simulation. Water Science and Technology: Water Supply, 2(5-6), 135-142.

[22] Crapulli, F., Santoro, D., Haas, C. N., Notarnicola, M., and Liberti, L. (2010). Modeling virus transport and inactivation in a fluoropolymer tube UV photoreactor using computational fluid dynamics. Chemical Engineering Journal, 161(1-2), 9-18.

[23] Cremer, M. A., and McMurtry, P. A. (1998). Model of turbulent mixing and reaction for H2-air combustion. AIAA Journal of Propulsion and Power, 14(3), 309-317.

[24] Crittenden, J., Trussell, R. R., Hand, D. W., Howe, K. J., and Tchobanoglous, G. (2005). Water treatment: principles and design, second edition, Hoboken, New Jersey: John Wiley and Sons, Inc.

[25] Darabiha, N., Giovangigili, V., Trouve, A., Candel, S. M. and Esposito, E. (1989). Coherent flame description of turbulent premixed ducted flames. Turbulent Reactive Flows, Springer-Verlag, New York.

[26] David, R., and Villermaux, J. (1975). Micromixing effects on complex reactions in a CSTR, Chem. Eng. Sci., 30, 1309.

[27] Deckwer, W. D., Burckhart, R., and Zoll, G. (1974). Mixing and mass transfer in tall bubbles columns. Chemical Engineering Science, 29, 2177-2188.

[28] Do-Quang, Z., and Laine, J. M. (1997). Advanced design of ozonation contactor for drinking water treatment: Use of computational Fluid dynamics modelling for reactor performance evaluation. Proceedings of the annual conference of the American water works association (AWWA) (p. 531) vol. D. Atlanta, June 15-19.

[29] Do-Quang, Z., Cockx, A., Line, A., and Roustan, M. (1999). Computational fluid dynamics applied to water and wastewater treatment facility modeling, Environ. Eng. Poll. 1, 137–147.

[30] Do-Quang, Z., Roustan, M., and Duguet, J.-P. (2000). Mathematical Modeling of Theoretical Cryptosporidium Inactivation in Full-Scale Ozonation Reactors. Ozone Sci. and Eng., 22(1), 99–111.

[31] Do-Quang, Z., A. Cockx, Laine, J. M., and Routstan, M. (2001). Applying CFD modelling in order to enhance water treatment reactors efficiency: Example of the ozonation process. Water Science and Technology: Water Supply, 1(4), 125–130.

[32] Ducoste, J., Liu, D., and Linden, K., (2005). Alternative approaches to modeling fluence distribution and microbial inactivation in ultraviolet reactors: lagrangian versus eulerian. Journal of Environmental Engineering, 131 (10), 1393–1403.

[33] Dutta, A., and Tarbell, J. M. (1989). Closure models for turbulent reacting flows. AIChE Journal, 35, 2013–2027.

[34] Elyasi, S., and Taghipour F. (2006). Simulation of UV photoreactor for water disinfection in Eulerian framework. Chemical Engineering Science, 61(14), 4741-4749.

[35] Evans, H., Bauer, M., Goodman, N., Hague, J., and Ta, T. (2003). The Role of Ozone in Improving Drinking Water Quality in London and Oxford. Ozone: Science and Engineering, 25(5), 409-416.

[36] Fabian, I. (1995). Mechanistic aspects of ozone decomposition in aqueous solution. Progress in Nuclear Energy, 29(8), 167-174.

[37] Falconer, R. A., and Ismail, A. I. B. M. (1997). Numerical Modelling of Tracer Transport in a Contact Tank, Environ. Int., 23(6), 763–773.

[38] Ferziger, J. H. (1987). Simulation of incompressible turbulent flows, Journal of Computational Physics, 69, 1-48

[39] Fluent user's guide version 6.3 (2006) Fluent Inc, Lebanon, N.H., ‹https:// www.sharcnet.ca/Software/Fluent6/html/ug/node1.htm›

[40] Fogler, H. S. (1999). Elements of Chemical Reaction Engineering (3rd edition). New York: Prentice Hall.

[41] Fox, R. O., and Villermaux J. (1990). Micromixing effects in the ClO_2^- + I^- reaction: Multiple-scale perturbation analysis and numerical simulation of the unsteady-state IEM model. Chemical Engineering Science, 45, 2857–2876.

[42] Fox, R. O. (1991). Micromixing effects in the Nicolis-Puhl reaction: Numerical bifurcation and stability analysis of the IEM model. Chemical Engineering Science, 46, 1829–1847.

[43] Fox, R. O., Erjaee, G., and Zou, Q. (1994). Bifurcation and stability analysis of micromixing effects in the chlorite-iodide reaction. Chemical Engineering Science, 49, 3465–3484.

[44] Fox, R. O. (1998). On the relationship between Lagrangian micromixing models and computational fluid dynamics. Chemical Engineering and Processing, 37, 521–535.

[45] Fox, R. O. (2003). Computational Models for Turbulent Reacting Flows. Cambridge University Press, New York.

[46] Froment, G. F., and Bischoff, K. B. (1979). Chemical reactor analysis and design, John Wiley and Sons, New York.

[47] Fureby, C. (2008). Toward the Use of Large Eddy Simulation in Engineering, Progress in Aerospace Sciences, 44(6), 381–396.

[48] Geering, F. (1991). Experiences With a New Plant for the Treatment of Lake Zurich Water. Ozone Sci. and Eng., 13(1), 41-62.

[49] Georgiadis, N. J., Rizzetta, D. P., and Fureby, C. (2009). Large-Eddy Simulation: current capabilities, recommended practices, and future research. 47th Aerospace Science Meeting, Orlando, Florida, January 5-8, 2009.

[50] Germano, M., Piomelli, U., Moin, P., and Cabot, W. H. (1991) A Dynamic Subgrid-Scale Eddy Viscosity Model, Physics of Fluids A, 3(7), 1760-1765.

[51] Goncalves, R. F., Taveira, E. J. A., Cassini, S. T. A., and de Oliveira, F. F. (2002). Recycled sludge thickening and digestion pond from physicochemical upgrading process of facultative pond effluent. International special group conference; 5th, Waste stabilization in ponds: pond technology for the new millennium, Auckland, New Zealand.

[52] Greene, D. J. (2002). Numerical Simulation of Chlorine Disinfection Processes in Non-Ideal Reactors (Doctoral dissertation). Available from ProQuest Dissertations & Theses database. (UMI No. 3058887).

[53] Greene, D. J., Haas, C. N., and Farouk, B. (2002). Numerical simulation of chlorine disinfection processes, Water Supply, 2(3), 167–173.

[54] Greene, D. J., Farouk, B., and Haas, C. N. (2004). CFD design approach: For chlorine disinfection processes. Journal / American Water Works Association, 96(8), 138-150+114.

[55] Greene, D. J., Haas, C. N., and Farouk, B. (2006). Computational fluid dynamics analysis of the effects of reactor configuration on disinfection efficiency. Water Environment Research, 78(9), 909-919.

[56] Gresch, M., Brugger, R., Meyer, A., and Gujer, W. (2009). compartmental models for continuous flow reactors derived from CFD simulations. Environ. Sci. Technol., 43(7), 2381–2387.

[57] Gualtieri, C. (2006). Numerical simulation of flow and tracer transport in a disinfection contact tank. 3rd Biennial meeting of the International Environmental Modelling and Software Society, Burlington, Vermont, USA. July 9-13, 2006.

[58] Gualtieri, C. (2007). Analysis of the effect of baffles number on a contact tank efficiency with multiphysics 3.3. Proc., COMSOL User Conference 2007, COMSOL AB, Napoli, Italy.

[59] Gurol, M. D., and Singer, P. C. (1982). Kinetics of ozone decomposition: a dynamic approach. Environ. Sci. Technol, 16 (7), 377–383.

[60] Gyurek, L. L., and Finch, G. (1998). Modeling water treatment chemical disinfection kinetics. Journal of Environmental Engineering, 124(9), 783-793.

[61] Gyurek, L. L. (1999). Ozone inactivation kinetics of Cryptosporidium in phosphate buffer. Journal of Environmental Engineering ASCE, 125(10), 913-924.

[62] Haag, W. R., and Hoigne, J. (1983). Ozonation of bromide-containing waters: kinetics of formation of hypobromous acid and bromate. Environ. Sci. Technol., 17(5), 261–267.

[63] Haas, C. N., and Karra, S. B. (1984a). Kinetics of Microbial Inactivation by Chlorine .1. Review of Results in Demand-Free Systems. Water Research, 18(11), 1443-1449.

[64] Haas, C. N. and Karra, S. B. (1984b). Kinetics of Microbial Inactivation by Chlorine .2. Kinetics in the Presence of Chlorine Demand. Water Research, 18(11), 1451-1454.

[65] Hanjalic, K., and Launder, B. E. (1972). A Reynolds stress model of turbulence and its application to thin shear layer flows, J. Fluid Mechanics, 52, 609-638.

[66] Hannoun, I. A., Boulos, P. F., and John, L. E. (1998). Using hydraulic modeling to optimize contact time. Journal AWWA, 90(8), 77-87.

[67] Hannoun, I. A., Bowman, K., and LaMoreaux, D. (2003). Computational Fluid Dynamics: Optimizing Water Quality in Clearwells, Tanks, and Distribution Storage Reservoirs. World Water and Environmental Resources Congress, Philadelphia, PA, United states.

[68] Heeb, T. G., and Brodkey, R. S. (1990). Turbulent mixing with multiple second-order chemical reactions. AIChE Journal, 36, 1457–1470.

[69] Henry, D. J., and Freeman, E. M. (1995). Finite element analysis and T-10 optimization of ozone contactors. Ozone: Sci. and Eng., 17(6), 587–606.

[70] Hijnen, W. A., Beerendonk, E. F., and Medema G. J. (2006). Inactivation credit of UV radiation for viruses, bacteria and protozoan (oo)cysts in water: A review. Water Research, 40(1), 3-22.

[71] Hill, C. G. (1977). An Introduction to Chemical Engineering Kinetics and Reactor Design. New York: John Wiley and Sons.

[72] Hoff, J. C. (1986). Inactivation of Microbial Agents by Chemical Disinfectants. Cincinnati, OH, Environmental Protection Agency (EPA/600/S2-86/067).

[73] Hofman, J., Wind, D., Wols, B., and Uijttewaal, W. (2007a). The use of CFD Modeling to Determine the Influence of Residence Time Distribution on the Disinfection of Drinking Water in Ozone Contactors. In Proceedings of the COMSOL Users Conference, Grenoble.

[74] Hofman, J., Shao, L., Wols, B., Uijttewaal, W., IJpelaar, G., Beerendonk, E., and van Dijk, H. (2007b). Design of UV reactors by CFD: model development and experi-mental validation. In Proceedings of the COMSOL Users Conference, Grenoble.

[75] Hoyer, O. (2002). Advanced Technologies in the New 30 MGD Surface Water Treatment Plant for the City and Region of Bonn, Germany. Proceedings from the American Water Works Association Annual Conference, New Orleans, Louisiana, June 16-20.

[76] Huang, T., Brouckaert, C. J., Docrat, M., and Pryor, M. (2002). A computational fluid dynamics and experimental study of an ozone contactor. Water Sci. Tech., 46(9), 87-93.

[77] Huang, T., Brouckaert, C. J., Pryor, M., and Buckley, C. A. (2004). Application of computational fluid dynamics modeling to an ozone contactor. Water SA, 30(1), 51–56.

[78] Janex, M. L., Savoye, P., Do-Quang, Z., Blatchley, E., and La ĥ é, J. M. (1998). Impact of water quality and reactor hydrodynamics on wastewater disinfection by UV, use of CFD modeling for performance optimization. Proceedings of the 1998 19th Biennial Conference of the International Association on Water Quality. Part 5 (of 10), June, 1998, Vancouver, Can, Elsevier Ltd.

[79] Jasak, H. A. (1996). Error analysis and estimation in the Finite Volume method with applications to fluid flows (Doctoral dissertation). Available at, http://powerlab.fsb.hr/ped/kturbo/OpenFOAM/docs/HrvojeJasakPhD.pdf.

[80] Johansson, S. H., Davidson, L., and Olsson, E. (1993), Numerical simulation of vortex shedding past triangular cylinders at high Reynolds number using a k-ε turbulence model. Int. J. Numer. Meth. Fluids, 16: 859–878.

[81] Josset, S., J. Taranto, Keller, N., Keller, V., and Lett, M. (2010). Photocatalytic Treatment of Bioaerosols: Impact of the Reactor Design. Environmental Science and Technology 44(7): 2605-2611.

[82] Juranek, D. D. (1995). Cryptosporidiosis: sources of infection and guidelines for prevention. Clinical Infectious Diseases, 21(1):57-61.

[83] Kamimura, M., Furukawa S., and Hirotsuji, J. (2002). Development of a simulator for ozone/UV reactor based on CFD analysis. Water Science and Technology, 46(11-12), 13–19.

[84] Karteris, A., Papadopoulos, A., and Balafoutas, G. (2005). Modeling the temperature pattern of a covered anaerobic pond with computational fluid dynamics. Water Air Soil Pollut., 162, 107-125.

[85] Kerstein, A. R. (1988). Linear eddy model of turbulent scalar transport and mixing. Combust. Sci. and Tech., 60, 391-421.

[86] Kerstein, A. R. (1990). Linear eddy model of turbulent transport. Part 3. Mixing and differential molecular diffusion in jets. Journal of Fluid Mechanics, 216, 411-435.

[87] Kerstein, A. R. (1992). Linear eddy model of turbulent transport. Part 7. Finite-rate chemistry and multi-stream mixing. Journal of Fluid Mechanics, 240, 289-313.

[88] Kim, J., Moin, P., and Moser, R. (1987). Turbulence statistics in fully developed channel flow at low Reynolds number. Journal of Fluid Mechanics, 177, 133-166.

[89] Kim, J. H., Tomiak, R. B., and Marines, B. J. (2002). Inactivation of cryptosporidium oocysts in a pilot-scale ozone bubble-diffuser contactor. I: Model Development. Journal of Environmental Engineering, 128(6), 514-521.

[90] Kim, J. H., Tomiak, R. B., Rennecker, J. L., Marinas, B. J., Miltner, R. J., and Owens, J. H. (2002). Inactivation of Cryptosporidium in a pilot-scale ozone bubble-diffuser contactor. Part II: Model verification and application. J. Environ. Eng. 128 (6), 522–532.

[91] Kim, J. H. (2005). A computer-based design of new ozone contactor-treating paldang dam reservoir water. Technical Report. Georgia Institute of Technology.

[92] Kim, J. H., Elovitz, M. S., Gunten, U. V., Shukairy, H. M., and Marinas, B. J. (2007). Modeling Cryptosporidium parvum oocyst inactivation and bromate in a flow-through ozone contactor treating natural water, Water Research, 41, 467–475.

[93] Kim, D. I., Hasan, S., Tang, G., Mariñas, B. J., Coulliard, L., Shijkairy, H., and Kim, J. H. (2007). Simultaneous simulation of pathogen inactivation and bromated formation in full-scale ozone contactors by computer software. Journal of AWWA, 99(8), 77-91.

[94] Kim, D., Kim, J. H., and Stoesser, T. (2009). LES and RANS modeling of Flow in an Ozone Contactor- Mean and Instantaneous Turbulent Flow Characteristics. 33rd IAHR Congress.

[95] Kim, D., Kim, D. I., Kim, J. H., and Stoesser, T. (2010a). Large Eddy Simulation of flow and tracer transport in multi-chamber ozone contactors. Journal of Environmental Engineering, 136, 22-31.

[96] Kim, D., Elovitz, M., Roberts, J. W. P., and Kim, J. H. (2010b). Using 3D LIF to investigate and improve performance of a multi-chamber ozone contactor. J AWWA 102(10), 61-70.

[97] Kim, D., Stoesser, T., and Kim, J. H. (2013a). Modeling aspects of flow and solute transport simulations in water disinfection tanks, Applied Mathematical Modelling, 37(16-17), 8039-8050.

[98] Kim, D., Stoesser, T. and Kim, J. H. (2013b). The effect of baffle spacing on hydrodynamics and solute transport in serpentine contact tanks. Journal of Hydraulic Research, 51(5), 558-568.

[99] Kolhapure, N. H., and Fox, R. O. (1999). CFD analysis of micromixing effects on polymerization in tubular low density polyethylene reactors, Chem. Eng. Sci., 54, 3233–3242.

[100] Launder, B. E., and Sharma, B. I. (1974). Application of the energy-dissipation model of turbulence to the calculation of flow near a spinning disc. Letters in Heat and Mass Transfer 1, 131-138.

[101] Launder, B. E., Reece, G. J. and Rodi, W. (1975). Progress in the development of a Reynolds-stress turbulence closure. J. Fluid Mechanics, 68(3), 537-566.

[102] Launder, B. E. (1978). Heat and mass transport. Turbulence, Chap. 6, P. Bradshaw, ed., Springer, Berlin.

[103] Lee, S., Shin, E., Kim, S. H., and Park, H. (2011). Dead Zone Analysis for Estimating Hydraulic Efficiency in Rectangular Disinfection Chlorine Contactors. Environmental Engineering Science, 28(1), 25-33.

[104] Lev, O., and Regli, S. (1992). Evaluation of Ozone Disinfection Systems-Characteristic Concentration-C. Journal of Environmental Engineering-ASCE, 118(4), 477-494.

[105] Levenspiel, O. (1998). Chemical Reaction Engineering (3rd edition). New York: John Wiley and Sons.

[106] Li, H., and Gyurek, L. L. (2001). Effect of temperature of ozone inactivation of Cryptosporidium in oxidant demand-free phosphate buffer. Journal of Environmental Engineering, 5, 456-467.

[107] Li, C., Deng, B., and Kim, C. N. (2010). A numerical prediction on the reduction of microorganisms with UV disinfection. Journal of Mechanical Science and Technology, 24(7), 1465-1473.

[108] Li, J., Zhang, J., Miao, J., Ma, J., and Dong, W. (2006). Application of computational fluid dynamics (CFD) to ozone contactor optimization. Water Science and Technology: Water Supply, 6(4), 9-16.

[109] Libby, P. A., and Williams, F. A. (1980). Fundamental aspects, Turbulent Reacting Flows: Topics in Applied Physics, 44, 1-43.

[110] Liew, S. K., Bray, K. M. C., and Moss, J. B. (1984). A stretched laminar flamelet model of turbulent nonpremixed combustion, Combust. Flame, 56, 199-213.

[111] Liu, D., Ducoste, J.J., Jin, S., and Linden K. (2004). Evaluation of Alternative Fluence Rate Distribution Models, J. Water Supply Res. Technol. AQUA, 53(6), 391–408.

[112] Lizima, L. A. (2012). Hydraulic Evaluation of a Community Managed Wastewater Stabilization Pond System in Bolivia (Master thesis). Available from ProQuest Dissertations & Theses database. (UMI No. 1530853).

[113] Lotierzo, M., Feliers, C., Faure, N., Le Grand, L., Saby, S., and Cervantes, P. (2003). Synergistic effects of sequential treatment by UV irradiation and chemical disinfectant for drinking water disinfection. Paper presented at the International Ultraviolet Light Association Conference in Vienna, Austria, July.

[114] Lyn, D. A., Chiu, K., and Blatchley, E. R. (1999). Numerical modeling of flow and disinfection in UV disinfection channels. J. Environ. Eng., 125(1), 17–26.

[115] Mandel, P. (2010). Modeling Ozonation Processes for Disinfection By-Product Control in Potable Water Treatment, From Laboratory to Industrial Units. Ph.D. thesis, University of Rennes 1, France. Available at, http,//tel.archives-ouvertes.fr/docs/00/56/47/67/PDF/Modeling_Ozonation_Processes_MANDEL.pdf.

[116] Mandel, P., Marie, M., Lemoine, C., Roche, P., and Wolbert, D. (2012). How Bromate and Ozone Concentrations Can be Modeled at Full-Scale Based on Lab-Scale Experiments – A Case Study, Ozone: Science and Engineering, 34(4), 280-292.

[117] Mara, D. D. (2004). Domestic wastewater treatment in developing countries, Earthscan Publications, London. Available at, http://www.pseau.org/outils/ouvrages/earthscan_ltd_domestic_wastewater_treatment_in_developing_countries_2003.pdf

[118] Mariñas, B. J., Liang, S., And Aieta, M. (1993). Modeling hydrodynamics and ozone residual distribution in a pilot-scale ozone bubble-diffuser contactor. Journal AWWA, March, 90-99.

[119] Mehta, R. V., and Tarbell, J. M. (1983). Four environment models of mixing and chemical reaction, AIChE J., 29(2), 320-329.

[120] Melissa, L., and Tafilaku, A. (2010). Chlorine Contact Optimization Utilizing CFD Modeling. 2010 Annual Conference Technical Papers - NC AWWA-WEA.

[121] Miao, J., Li, J., Zhang, J. S., Zhao, Q. L., and Ma, J. (2006). Application of Computational Fluid Dynamics to Optimization of Ozone Contactor. China Water and Wastewater, 22(10), 46-49.

[122] Mizuno, T., Park, N. S., Tsuno, H., and Hidaka, T. (2005). Evaluating effective volume and hydrodynamic behavior in a full-scale ozone contactor with computational fluid dynamics simulation. Water Supply, 4(5-6), 277–288.

[123] Murphy, C. (2012). Quantifying the Impact of Sludge Accumulation on the Hydraulic Performance of Waste Stabilization Ponds (Master thesis). Available at, http://www.sese.uwa.edu.au/__data/assets/pdf_file/0009/2158866/Murphy_THESIS_2012.pdf.

[124] Murrer, J., Gunstead, J., and Lo, S. (1995). The development of an ozone contact tank simulation model. Ozone: Sci. and Eng., 17(6), 607–617.

[125] Nelson, K., Cisneros, B., Tchobanoglous, G., and Darby, J. (2004). Sludge accumulation, characteristics, and pathogen inactivation in four primary waste stabilization ponds in central Mexico. Water Res., 38(1), 111-127.

[126] Nguyen-Tien, K., Patwari, A. N., Schumpe, A., and Deckwer, W. D. (1985). Gas-liquid mass transfer in fluidized particle beds. AICHE Journal, 31, 194-201.

[127] Oakley, S. (2005). Lagunas de Estabilización en Honduras: Manual de Diseño, Construcción, Operación y Mantenimiento, Monitoreo y Sostenibilidad. United States Agency for International Development-Honduras (USAID-Honduras), Red Regional de Agua y Saneamiento para Centro América (RRAS-CA), Fondo Hondureño de Inversión Social (FHIS), Tegucigalpa, Honduras.

[128] Okino, M., and Mavrovouniotis, M. (1999). Simplification of chemical reaction systems by time-scale analysis, Chemical Engineering Communications, 176(1), 115-131.

[129] OpenFOAM User Guide version 1.7.1 (2010) OpenCFD Ltd. ‹http://www.openfoam.com /docs/user/›

[130] Owens, J. H., Miltner, R. J., Rice, E. W., Johnson, C. H., Dahling, D. R., Schaefer III, F. W., and Shukairy, H. M. (1994). Pilot-Scale Ozone Inactivation of Cryptosporidium and Giardia. Conference proceedings, Water Quality Technology Conference, Part II, San Francisco, CA.

[131] Papadopoulos, A., Papadopoulos, F., Parisopoulos, G., and Karteris, A. (2003). Sludge accumulation pattern in an anaerobic pond under Mediterranean climatic conditions. Water Res., 37(3), 634-644.

[132] Patel, V., Rodi, W., and Scheuerer, G. (1985). Turbulence models for near-wall and low Reynolds number flows: A review. AIAA Journal, 23, 1308–1319.

[133] Peña, M. R., Mara, D. D., and Sanchez, A., (2000). Dispersion studies in anaerobic ponds: implications for design and operation. Water Sci. Technol., 42, 273-282.

[134] Peplinski, D. K., and Ducoste, J. J. (2002). Modeling of Disinfection Contactor Hydraulics Under Uncertainty. J. Environ. Eng. ASCE, 128(11), 1056–1067.

[135] Peplinski, D. K., and J. J. Ducoste (2004). Lessons for applying computational fluid dynamics modeling to disinfection clearwells. World Water and Environmental Resources Congress 2001, May 2001, Orlando, FL, United states, American Society of Civil Engineers.

[136] Peters, N. (1984). Laminar diffusion flamelet models in non-premixed turbulent combustion. Progress in Energy and Combustion Science, 10, 319–339.

[137] Peters, N. (2000). Turbulent Combustion. Cambridge Monographs on Mechanics. Cambridge: Cambridge University Press.

[138] Peterson, E. L., Harris, J. A., and Wadhwa, L. C. (2000). CFD modelling pond dynamic processes. Aquacult. Eng., 23, 61-93.

[139] Phares, D. E., D. M. Rokjer, Crossley, I. A., and Franko, J. J. (2009). Modeling and validating the effective hydraulic detention time for a 10 mgd ozone contactor at the lake Washington surface water treatment plant, Melbourne, Florida. Ozone: Science and Engineering, 31(3), 262-276.

[140] Piomelli, U., and Balaras, E. (2002). Wall-layer models for large-eddy simulations. Annu. Rev. Fluid Mech., 34, 349–374.

[141] Pitsch, H., Desjardins, O., Balarac, G., and Ihme, M. (2008). Large Eddy Simulation of Turbulent Reacting Flow, Progress in Aerospace Sciences, 44(6), 466–478.

[142] Plummer, J., Long, S., Wong, K., and Mahar, E. (2002). Inactivation of E. coli and MS2 coliphage with Ultrasound and Chlorine. Paper presented at the 2002 Annual American Water Works Association Conference, New Orleans.

[143] Pope, S. B. (2000). Turbulent Flows. Cambridge University Press.

[144] Ranade, V. V., and Bourne, J. R. (1991). Fluid mechanics and blending in agitated tanks, Chem. Eng. Sci., 46, 1883-1893.

[145] Ranade, V. V. (1993). Interaction of macro and micromixing in agitated reactors, in "Advances in Transport Processes", (Eds. R.A. Mashelkar and A.S. Mujumdar), Vol. 9, Elsevier, New York.

[146] Ranade, V. V. (2002). Computational flow modeling for chemical reactor engineering. San Diego, California: Academic Press.

[147] Rauen, W. B., Lin, B., Falconer, R. A., and Teixeira, E. C. (2008). CFD and experimental model studies for water disinfection tanks with low Reynolds number flows. Chemical Engineering Journal, 137(3), 550-560.

[148] Reddy, S. (2003). Computer simulation: Reducing cost of chlorine in wastewater plant. Chemical Engineering World, 38(4), 66-67.

[149] Rice, R. G. (1996). Ozone Reference Guide: an Overview of Ozone Fundamentals and Municipal and Industrial Ozone Applications. EPRI, Community Environmental Center, St. Louis, MO. Report CR-106435.

[150] Ritchie, B. W., and Togby, A. H. (1979). A three environment micromixing model for chemical reactors with arbitrary separate feed streams, Chem. Eng. J., 17, 173.

[151] Roustan, M., Chatellier, P., Lefervre, F., Audic, J. M., and Burvingt, F. (1993). Separation of the two functions-aeration and mixing in oxidation ditches: application to the denitrification by activated sludge. Environ. Technol., 14, 841–849

[152] Sagaut, P., and Deck, S. (2009). Large eddy simulation for aerodynamics: status and perspectives. Phil Trans R Soc. A, 367, 2849-2860.

[153] Shenoy, U. V., and H. L. Toor (1990). Unifying indicator and instantaneous reaction methods of measuring micromixing. AIChE Journal, 36, 227–232.

[154] Shilton, A., (2000). Potential application of computational fluid dynamics to pond design. Water Sci. Technol., 42, 327-334.

[155] Shilton, A., Kreegher, S., and Grigg, N. (2008). Comparison of computation fluid dynamics simulation against tracer data from a scale model and full-sized waste stabilization pond. J. Environ. Eng., 134, 845-850.

[156] Siddiqui, M., Amy, G., Ozekin, K., and Westerhoff, P. (1998). Modeling Dissolved Ozone and Bromate Ion Formation in Ozone Contactors. Water, Air and Soil Pollution, 108(1–2), 1–32.

[157] Smagorinsky, J. (1963). General circulation experiments with the primitive equations. Monthly Weather Rev., 93, 99−164.

[158] Smeets, P. W. M. H., van der Helm, A. W. C., Dullemont, Y. J., Rietveld, L. C., van Dijk, J. C., and Medema, G. J. (2006). Inactivation of Escherichia coli by Ozone under Bench-Scale Plug Flow and Full-Scale Hydraulic Conditions. Water Res., 40(17), 3239–3248.

[159] Solomon, C., Casey, P., Mackne, C., and Lake, A. (1998). Chlorine Disinfection. The National Small Flows Clearinghouse. Technical Overview.

[160] Song, R., Minear, R., Westerhoff, P., and Amy, G. (1996). Bromate formation and control during water ozonation. Environmental Technology, 17(8), 861-868.

[161] Sozzi, D. A., and Taghipour, F. (2006). UV reactor performance modeling by Eulerian and Lagrangian methods. Environmental Science and Technology, 40(5), 1609-1615.

[162] Spalart, P. R., Jou, W.-H., Stretlets, M., and Allmaras, S. R. (1997). Comments on the Feasibility of LES for Wings and on the Hybrid RANS/LES Approach, Advances in DNS/LES, Proceedings of the First AFOSR International Conference on DNS/LES.

[163] Stamou, A. I. (2002). Verification and Application of a Mathematical Model for the Assessment of the Effect of Guiding Walls on the Hydraulic Efficiency of Chlorination Tanks. Journal of Hydroinformatics, 4(4), 245–254.

[164] Stamou, A. I. (2008). Improving the hydraulic efficiency of water process tanks using CFD models. Chemical Engineering and Processing: Process Intensification, 47(8), 1179-1189.

[165] Strelets, M. (2001), Detached Eddy Simulation of Massively Separated Flows, AIAA, 2001-0879.

[166] Stropky, D., Pouqatch, K., Nowak, P., Salcudean, M., Pagorla, P., Gartshore, I., and Yuan, J. W. (2007). RTD (residence time distribution) predictions in large mechanically aerated lagoons. Water Science and Technology, 55(11), 29–36.

[167] Sweeney, D. G., Nixon, J. B., Cromar, N. J., and Fallowfield, H. J. (2005). Profiling and modelling of thermal changes in a large waste stabilization pond. Water Sci. Technol., 51, 163-172.

[168] Ta, C. T., and Hague J. (2004). A two-phase computational fluid dynamics model for ozone tank design and troubleshooting in water treatment. Ozone: Science and Engineering, 26(4), 403-411.

[169] Taghipour, F., and Sozzi, A. (2005). Modeling and design of ultraviolet reactors for disinfection by-product precursor removal. Desalination, 176(1-3), 71-80.

[170] Talvy, S., Debaste, F., Martinelli, L., Chauveheid, E., and Haut, B. (2011). Development of a tool, using CFD, for the assessment of the disinfection process by ozonation in industrial scale drinking water treatment plants. Chemical Engineering Science, 66(14), 3185-3194.

[171] Tang, G., Adu-Sarkodie, K., Kim, D., Kim, J. H., Teefy, S., Shukairy, H. M., and Marinas, B. J. (2005). Modeling Cryptosporidium parvum oocyst inactivation and bromate formation in a full-scale ozone contactor. Environmental Science and Technology, 39(23), 9343-9350.

[172] Tejada-Martinez, A. E., and Jansen, K. E. (2005). On the interaction between dynamic model dissipation and numerical dissipation due to streamline upwind / Petrov-Galerkin stabilization, Computer Methods in Applied Mechanics and Engineering, 194, 1225-1248.

[173] Tennekes, H., and Lumley, J. L. (1972). A first course in turbulence, Cambridge, MA: MIT Press.

[174] Thyn, J., Ha, J. J., Strasak, P., and Zitny, R. (1998). RTD prediction, modeling and measurement of gas flow in reactor. Nukleonika 43(1), 95–114.

[175] Tsai, K., and Fox, R. O. (1995). Modeling multiple reactive scalar mixing with the generalized IEM model. Physics of Fluids, 7, 2820–2830.

[176] U.S. EPA (1991). Guidance manual for compliance with the filtration and disinfection requirements for public water systems using surface water, U.S. EPA, Washington, D.C.

[177] U.S. EPA (2001). Toxicological Review of Bromate. EPA/635/R-01/002. U.S. EPA, Washington, DC.

[178] U.S. EPA (2003). Disinfection profiling and benchmarking guidance manual, Appendix A. Rep. No. EPA 816-R-03-004, U.S. EPA, Washington, D.C.

[179] Vega, G. P., Pena, M. R., Ramirez, C., and Mara, D. D., (2003). Application of CFD modelling to study the hydrodynamics of various anaerobic pond configurations. Water Sci. Technol., 48, 163-171.

[180] Verbyla, M. E., Oakley, S. M., Lizima, L. A., Zhang, J., Iriarte, M., Tejada-Martinez, A. E., and Mihelcic, J. R. (2013). Taenia eggs in waste stabilization pond systems with poor hydraulics: Concern for human cysticercosis? Water Science and Technology, 68(12), 2698-2703.

[181] Villermaux, J., and Falk, L. (1994). A generalized mixing model for initial contacting of reactive fluids. Chemical Engineering Science, 49, 5127–5140.

[182] von Gunten, U., and Hoigné, J. (1994). Bromate formation during ozonation of bromide-containing waters: Interaction of ozone and hydroxyl radical reactions. Environmental Science and Technology, 28, 1234-1242.

[183] von Gunten, U., and Pinkernell, U. (2000). Ozonation of bromide-containing drinking waters: a delicate balance between disinfection and bromate formation. Water Science and Technology, 41, 53-59.

[184] Wang, H., and Falconer, R. A. (1998a). Numerical modeling of flow in chlorine disinfection tanks. Journal of Hydraulic Engineering, 124, 918-931.

[185] Wang, H., and Falconer, R. A. (1998b). Simulating disinfection processes in chlorine contact tanks using various turbulence models and high-order accurate difference schemes. Water Research, 32(5), 1529–1543.

[186] Westerhoff, P., Song, R., Amy, G., and Minear, R. (1998). Numerical Kinetic Models for Bromide Oxidation to Bromine and Bromate. Water Res., 32(5), 1687–1699.

[187] Whiting, C. (1999). Stabilized Finite Element Methods for Fluid Dynamics Using a Hierarchical Basis (Doctoral dissertation). Available from ProQuest Dissertations & Theses database. (UMI No. 9958535).

[188] Wilcox, D. C. (1994). Turbulence Modeling for CFD. La Canada, CA:DCW Industries.

[189] Wols, B. A., Hofman, J. A. M. H., Uijttewaal, W. S. J., Rietveld, L. C., Stelling, G. S., and van Dijk, J. C. (2008a). A particle tracking technique to estimate disinfection efficacy in drinking water treatment plants. In: 6th International Conference on CFD in the Oil and Gas, Metallurgical and Process Industries, Trondheim.

[190] Wols, B. A., Uijttewaal, W. S., Rietvelda, L. C., Stellinga, G. S., van Dijka, J. C. and Hofman, J. A. M. H. (2008b). Residence time distributions in ozone contactors. Ozone: Science and Engineering: The Journal of the International Ozone Association, 30(1), 49-57.

[191] Wols, B. A., Hofman, J. A. M. H., Uijttewaal, W. S. J., Rietveld, L. C., and van Dijk, J. C. (2010a). Evaluation of different disinfection calculation methods using CFD. Environmental Modelling and Software, 25, 573–582.

[192] Wols, B. A., Shao, L., Uijttewaal, W. S. J., Hofmana, J. A. M. H., Rietveld, L. C., and van Dijk, J. C. (2010b). Evaluation of experimental techniques to validate numerical computations of the hydraulics inside a UV bench-scale reactor. Chemical Engineering Science, 65(15), 4491-4502.

[193] Wols, B. A., Uijttewaal, W. S. J., Hofmana, J. A. M. H., Rietveld, L. C., and van Dijk, J. C. (2010c). The weaknesses of a k-ε model compared to a large-eddy simulation for the prediction of UV dose distributions and disinfection. Chemical Engineering Journal, 162(2), 528-536.

[194] Wols, B. A., Hofman, J. A. M. H., Beerendonk, E. F., Uijttewaal, W. S. J., and van Dijk, J.C. (2011). A systematic approach for the design of UV reactors using computational fluid dynamics. AIChE Journal, 57(1), 193-207.

[195] Wols, B. A., Hofman-Caris, C. H. M., Harmsen, D. J. H., Beerendonk, E. F., van Dijk, J.C. Chan, P., and Blatchley, E. R. (2012). Comparison of CFD, Biodosimetry and Lagrangian Actinometry to Assess UV Reactor Performance. Ozone: Science and Engineering, 34(2), 81-91.

[196] Wood, M. G., Greenfield, P. F., Howes, T., Johns, M. R., and Keller, J. (1995). Computational fluid dynamic modeling of waste-water ponds to improve design. Water Sci. Technol., 31, 111-118.

[197] Wood, M. G., Howes, T., Keller, J., and Johns, M. R. (1998). Two dimensional computational fluid dynamic models for waste stabilization ponds. Water Res., 32, 958-963.

[198] Yu, B., Deng, B., and Kim, C. N. (2008). Performance evaluation of P-1 model in a photocatalytic reactor. Chemical Engineering Science, 63 (22), 5552–5558.

[199] Zhang, J., Tejada-Mart ńez, A. E., and Zhang, Q. (2013a). RANS Simulation of the Flow and Tracer Transport in a Multi-Chambered Ozone Contactor. Journal of Environmental Engineering, 139(3), 450-454.

[200] Zhang, J., Tejada-Mart ńez, A. E., and Zhang, Q. (2013b). Hydraulic Efficiency in RANS of the Flow in Multi-Chambered Ozone Contactors, Journal of Hydraulic Engineering, 139(11), 1150-1157.

[201] Zhang, J., Tejada-Mart ńez, A. E., Zhang, Q., and Lei H. (2014). Evaluating Hydraulic and Disinfection Efficiencies of a Full-Scale Ozone Contactor using a RANS-based Modeling Framework. Water Research. 52:155-167.

[202] Zhang, J. P. (2006). An integrated design approach for improving drinking water ozone disinfection treatment based on computational fluid dynamics (Doctoral dissertation). Available from ProQuest Dissertations & Theses database. (UMI No. NR36453).

[203] Zhang, J. P., Huck, M., Anderson, B. W., and Stubley, D. G. (2007). A computational fluid dynamics based integrated disinfection design approach for improvement of full-scale ozone contactor performance. Ozone: Science and Engineering: The Journal of the International Ozone Association, 29(6), 451-460.

[204] Zhang, J. P., Huck, M., Anderson, W. B., and Stubley, G. D. (2008). Application of a multiphase CFD modelling approach to improve ozone residual monitoring and tracer testing strategies for full-scale drinking water ozone disinfection processes. Journal of Water Supply: Research and Technology – AQUA, 57(2), 79-92.

[205] Zhang, L., Pan, Q., and Rempel, G. L. (2007). Residence time distribution in a multistage agitated contactor with Newtonian fluids: CFD prediction and experimental validation. Industrial and Engineering Chemistry Research, 46 (11), 3538–3546.

[206] Zhao, X., Alpert, S. M., and Ducoste, J. J. (2009). Assessing the impact of upstream hydraulics on the dose distribution of ultraviolet reactors using fluorescence microspheres and computational fluid dynamics. Environmental Engineering Science, 26(5), 947-959.

APPENDICES

Appendix A: List of Symbols

u_i	Velocity in i-th direction
x_i	Position in i-th direction
t	Time
ρ	Fluid density
p	Pressure
ν	The kinematic viscosity
f_i	Body force (the force per unit of mass) in the ith direction
Re	The Reynolds number
U	Characteristic velocity of the flow
L	Characteristic length scale of the flow
C	The tracer concentration
D	The molecular diffusivity for the scalar
C_i	The species concentration
D_i	The molecular diffusivity for the scalar
S_i	The external volumetric source term
k_d	The ozone decay constant
C_l	The concentration of dissolved ozone
NOM	Natural Organic Carbon
k_{NOM}	The reaction rate constant for the reaction between dissolved ozone and *NOM*
[NOM]	The concentration of *NOM*
k_B	The bromate formation rate constant
C_B	The concentration of bromate

S_{C_l}	The external volumetric source term for dissolved ozone
$S_{[NOM]}$	The external volumetric source term for *NOM*
S_{C_B}	The external volumetric source term for bromate
S_{C_T}	The external volumetric source term for passive tracer
CT	Concentration-contact time
N_m	The concentration of microorganism m
S_{N_m}	The external volumetric source term for microorganism m
G	Incident radiation
r	The radial distance from the lamp
I_{max}	The light intensity
r_s	Radius at lamp surface
a	The absorption coefficient
UVT	Ultraviolet radiation transmission
σ_s	The scattering coefficient
C_1	The linear-anisotropic phase function coefficient
z	The axial distance
l_i	The distance from the current location to the point source number n_i
I_0	The UV lamp output (energy rate per unit length)
D_{UV}	Represents the UV dose
D_{min}	The shift in dose distribution
λ	Distribution factor
N_0	The initial concentration of the microorganism *m*
$k_{\mu,m}$	The inactivation rate constant for the microorganism *m*

$k_{UV,m}$	The intrinsic rate constant of the microorganism *m*
T	Temperature
$\langle\ \rangle$	The Reynolds-averaging operation
$\langle S_{C_i} \rangle$	The Reynolds-averaged chemical source term
$\langle C_l \rangle$	Mean of the concentration of dissolved ozone
C_l'	Fluctuation of the concentration of dissolved ozone
$\langle [NOM] \rangle$	Mean of the concentration of fast reacting *NOM*
$[NOM]'$	Fluctuation of the concentration of fast reacting *NOM*
Ω	The entire flow domain
$G(r, x_i)$	A filter function
$u_i''(x_i, t)$	The sub-grid or residual velocity
$\bar{u}_i$	The filtered velocity
$\bar{p}$	The filtered pressure
$\bar{S}_{ij}$	The filtered strain-rate tensor
τ_{ij}	Sub-grid-scale (SGS) stress
ν_t	The SGS eddy viscosity
Δx	The local mesh spacings in the x_1 direction
Δy	The local mesh spacings in the x_2 direction
Δz	The local mesh spacings in the x_3 direction
C_s	Smagorinsky coefficient
$\langle u_i \rangle$	Mean component of velocity
u_i'	Fluctuating or turbulent component of velocity
$\langle p \rangle$	Reynolds-averaged or mean pressure

$-\langle u_i' u_j' \rangle$	Reynolds stress tensor
k	The turbulent kinetic energy
ε	The turbulent kinetic energy dissipation rate
$\langle C \rangle$	The Reynolds-averaged or mean tracer concentration
C'	Concentration fluctuation
S_{CT}	The turbulent Schmidt number
$\bar{C}$	Filtered tracer concentration
D_t'	The SGS diffusivity
τ	Theoretical mean residence time
V	Volume of contactor
Q	Flow rate
θ	Normalized time
$E(\theta)$	Normalized tracer concentration or residence time distribution (RTD) function
C_{init}	Initial tracer concentration
$T_{release}$	The total time over which the tracer is released
$F(\theta)$	Cumulative residence time distribution function
MDI	The Morrill dispersion index
t_{10}	The time it takes for 10% of the tracer to exit the contactor
t_{16}	The time it takes for 16% of the tracer to exit the contactor
t_{50}	The time it takes for 50% of the tracer to exit the contactor
t_{90}	The time it takes for 90% of the tracer to exit the contactor
S	Short-circuiting index
k	Second-order rate constant

[ ]	Means concentration of species
k_1	Rate constant for reaction between bromide and ozone
k_2	Rate constant for reaction between bromide and ozone
k_3	Rate constant for reaction between hypobromite and ozone
k_4	Rate constant for bromite formation
$k_{[TOC]}$	Rate constant for bromate formation
k_i^{eff}	Effective reaction rate constant for chemical species *i*
$k_L a$	Overall mass transfer constant
$p_{B_rO^-}$	The percentage of B_rO^- for bromate formation
J	The Jacobian matrix
τ_α	Chemical time scale
μ_α	The eigenvalue of the Jacobian matrix
t_K	Kolmogorov time scale
h_R	Hydraulic diameter
A_c	The cross-section area at inlet
y_1^+	The distance between the first grid point and the bottom or baffle wall in plus units
τ_w	The wall shear stress
d	The distance of the first grid point off the wall
V_1	The time averaged flow speed at the first grid point off the wall
T_{peak}	The time at which the peak RTD occurs
T_1	The time it takes for the amount of tracer at the outlet to reach 1% of the amount of tracer injected at the inlet

H	Water surface height
θ_{10}	Normalized t_{10} (equal to t_{10}/τ)
θ_{50}	Normalized t_{50} (equal to t_{50}/τ)
θ_{90}	Normalized t_{90} (equal to t_{90}/τ)
V_L	Volume of sludge produced each year
Q_{av}	Average flow
SS	Suspended solids in the influent
τ_{ij}^{SGS}	The LES subgrid-scale stress
δ	The channel half-width
u_τ	The wall shear velocity
τ_{ij}^{v}	The viscous stress
$\nu_{non-dim}$	Non-dimensional viscosity
Re_τ	Wall shear Reynolds number
u^+	The dimensionless velocity
f_1^n	The force at time step *n*
U_{bulk}	The target bulk velocity at the inlet/outlet
U_{bulk}^n	The computed bulk velocity at the inlet/outlet at time step *n*
α	Relaxation parameter
ΔP	The pressure drop across the entire streamwise (x_1) length of the contactor
ΔL	The entire streamwise length (x_1) of the contactor
p_{loss}	Energy loss per unit volume

Appendix B: Verification and Validation of OpenFOAM

Turbulent channel flow is a canonical problem which has been studied extensively to understand the mechanics of wall-bounded turbulent flows. This flow is a common choice to test and validate OpenFOAM for incompressible flow.

A typical channel flow problem has the geometry shown in Figure B.1. The channel is bounded by no-slip walls normal to the *y*-axis. Periodic boundary conditions are set in the streamwise (*x*) and spanwise (*z*) representative of a channel of infinite lengths in those directions.

B.1 Governing Equations

The following N-S equations in non-dimensional form are solved in LES and DNS. In DNS, the LES subgrid-scale stress, τ_{ij}^{SGS}, introduced earlier is set to zero.

$$\frac{\partial u_i}{\partial t} + \frac{\partial u_i u_j}{\partial x_j} = \frac{1}{Re}\frac{\partial \tau_{ij}^{v}}{\partial x_j} + \frac{\partial \tau_{ij}^{SGS}}{\partial x_j} + f_i \tag{B.1}$$

here all variables are non-dimensionalized by the channel half-width δ, and the wall shear velocity u_τ,

$$u_\tau = \sqrt{\frac{\tau_w}{\rho}} \tag{B.2}$$

where τ_w is shear stress at wall, ρ is fluid density, u_i is velocity in i-th direction, t is time, τ_{ij}^{v} is the viscous stress, f_i is body force in i-th direction. Re is the Reynolds number, defined as:

$$Re = \frac{u\delta}{\nu} \tag{B.3}$$

where ν is kinematic viscosity, u is bulk velocity, and $\delta = 1$ in this case.

For further use, define wall shear Reynolds number as:

$$Re_\tau = \frac{u_\tau \delta}{\nu} \tag{B.4}$$

Define non-dimensional viscosity as:

$$\nu_{non-dim} = \frac{1}{Re} \tag{B.5}$$

Averaging in time and over x_1 and x_2, and letting $u_i = \langle u_i \rangle + u_i'$ leads to

$$0 = -\frac{\partial}{\partial x_2}\langle u_1' u_2' \rangle + \frac{1}{Re}\frac{\partial \langle \tau_{12}^{\nu} \rangle}{\partial x_2} + \frac{\partial \langle \tau_{12}^{SGS} \rangle}{\partial x_2} + f_1 \tag{B.6}$$

as the x_1-momentum equation.

From equation (B.6), the following relationship between $\frac{\partial \langle u_1 \rangle}{\partial x_2}$ and Re_τ can be derived:

$$\left(\frac{\partial \langle u_1 \rangle}{\partial x_2}\right)\Big|_{x_2=-1} = \frac{{Re_\tau}^2}{Re} \tag{B.7}$$

And the relationship between f_1, Re_τ, and Re can be derived:

$$f_1 = \frac{{Re_\tau}^2}{Re^2} \tag{B.8}$$

Furthermore, the sum of Reynolds stress and shear stress can be probed to be a linear function of x_3:

$$-\langle u_1' u_2' \rangle + \frac{1}{Re}\langle \frac{\partial \langle u_1 \rangle}{\partial x_2} \rangle = -\tau_w x_2 \tag{B.9}$$

where Reynolds stress $\langle u_1' u_3' \rangle$ define as:

$$\langle u_1' u_2' \rangle = \langle u_1 \, u_2 \rangle - \langle u_1 \rangle \langle u_2 \rangle \tag{B.10}$$

Equation (B.7) and (B.9) will be used as validation criteria.

B.2 Problem Description

A DNS simulation was conducted for turbulent channel flow. For DNS of turbulent flow, the mesh is refined near wall because of the need of solving the small scales of turbulence flow

near wall. A near wall refined mesh is also used for LES, while the mesh for bulk flow could be coarser due to the use of SGS model. Dynamic Smagorinsky model is used for LES in this case.

In this case, Reynolds number and wall stress Reynolds number are: $Re = 2800$, $Re_\tau = 180$. Then the following properties can be calculated:

$$f_1 = \tau_w = \frac{{Re_\tau}^2}{Re^2} = 4.133 \times 10^{-3}$$

$$\nu_{non-dim} = \frac{1}{Re} = \frac{1}{2800} = 3.57 \times 10^{-4}$$

The size of the domain is: $4\pi \times 2 \times \frac{4}{3}\pi$ ($x \times y \times z$ or $x_1 \times x_2 \times x_3$). The meshes for DNS and LES consist 893,952 grid points (96×96×97 in *x*-*y*-*z* directions) and 66,560 grid points (32×32×65 in *x*-*y*-*z* directions) respectively, shown in Figure B.2.

B.3 Results and Discussion

The profile of the mean velocity non-dimensionalized by the wall shear velocity for DNS is shown in Figure B.3. The dashed line represents the law of the wall and the log law. Within the sub-layer, $y^+ < 5$, the computational results agree the linear law of the wall well:

$$u^+ = y^+ \tag{B.11}$$

where y^+ is dimensionless wall distance, calculated as

$$y^+ = \frac{u_\tau y}{\nu} \tag{B.12}$$

u^+ is the dimensionless velocity, calculated as

$$u^+ = \frac{u}{u_\tau} \tag{B.13}$$

And for the Logarithmic region, the computational results also follow the log law well:

$$u^+ = \frac{1}{0.4}\ln y^+ + 5.5 \tag{B.14}$$

Turbulence intensities normalized by the wall-shear velocity for DNS and LES are shown in Figure B.4 and Figure B.5. The symmetry of the profiles about the channel centerline indicates the adequacy of the sample taken for the average.

The total stress, $-\langle u_1' u_2' \rangle + \frac{1}{Re} \langle \frac{\partial \langle u_1 \rangle}{\partial x_2} \rangle$, and the Reynolds stress, $-\langle u_1' u_2' \rangle$, along y axis are shown in Figure B.6. For total stress, both DNS and LES result have an excellent agreement with the theoretical solution, which is a straight line. And, both DNS and LES results agree well with Kim's DNS in the Reynolds stress, $-\langle u_1' u_2' \rangle$.

B.4 Conclusion

In this section, two approaches, DNS and LES, in OpenFOAM are applied to simulation of laminar and turbulent channel flow. The results agree well with theoretical results, demonstrating OpenFOAM is a reliable tool for simulating incompressible flow.

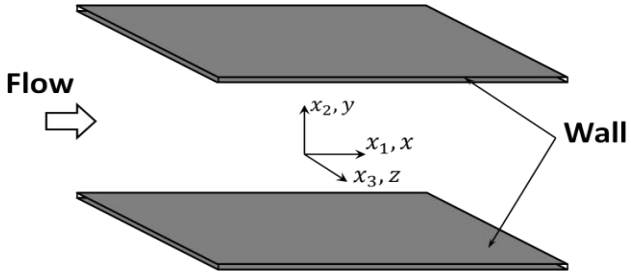

Figure B.1: Sketch of channel flow.

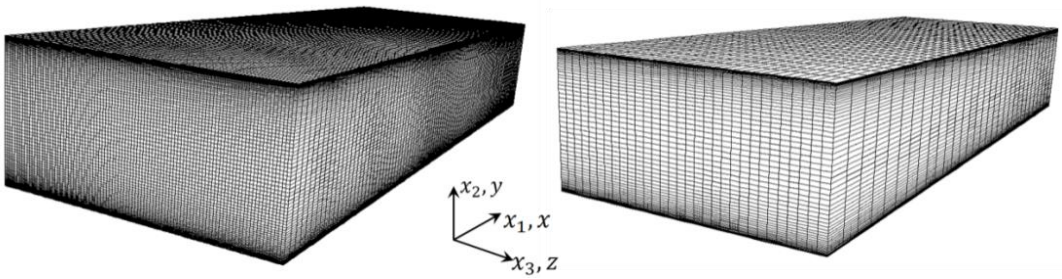

Figure B.2: Meshes for DNS (left) and LES (right).

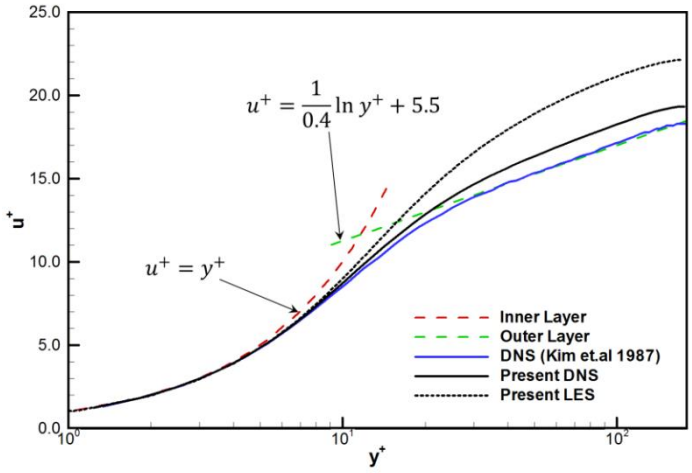

Figure B.3: Mean velocity profile.

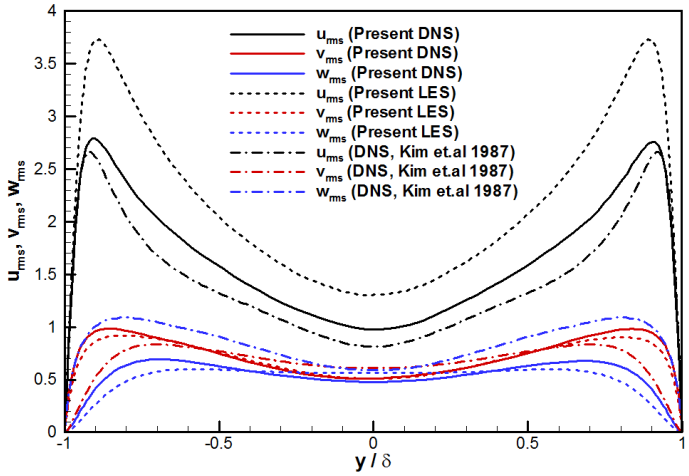

(a)

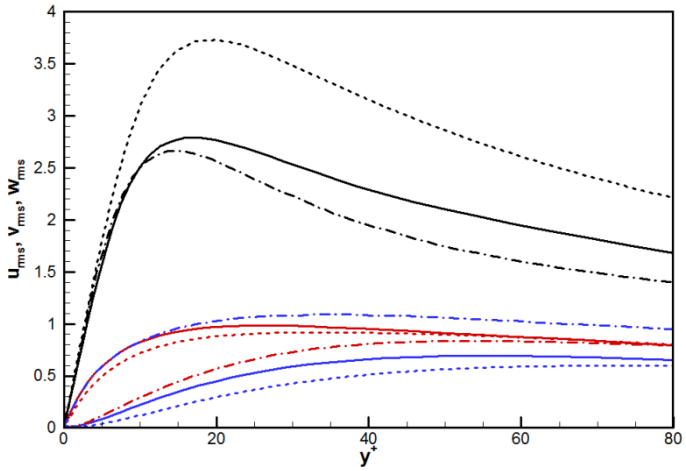

(b)

Figure B.4: Root-mean-square velocity fluctuations normalized by the wall velocity (a) in global coordinates; (b) in wall coordinates.

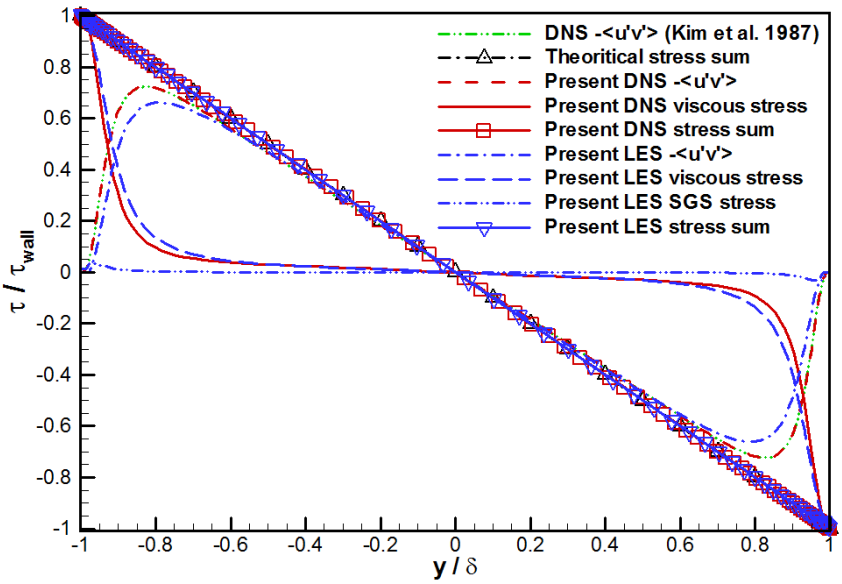

Figure B.5: Sum of Time-spatial averaged viscous stress and Reynolds stress distribution along z axis.

Appendix C: Inlet Turbulence Intensity

Fluid flow simulations often require an estimate of the turbulence intensity at the inflow boundary. For highly turbulent conditions, the turbulence intensity at the inlet is typically in the range 5 to 10% of the Reynolds-averaged velocity (see Fluent User's Guide 2006). As shown by Huang et al. (2004), RANS predictions of tracer residence time distribution (RTD) density in baffled contactors may be strongly dependent on the prescribed turbulence intensity at the contactor inlet. In their computations, a 10% inlet turbulence intensity led to an over prediction of the peak of the RTD density function while an extremely high 50% inlet turbulence intensity was needed to obtain good agreement with experimental data.

A way to avoid dependence of results on the inlet turbulence intensity is to prescribe the inlet and outlet of the contactor as periodic. In this case a streamwise pressure gradient in the form of a body force is added to the Navier-Stokes equations in order to ensure a targeted bulk velocity at the periodic inlet/outlet:

$$\frac{\partial\langle u_i\rangle}{\partial t}+\langle u_j\rangle\frac{\partial\langle u_i\rangle}{\partial x_j}=-\frac{1}{\rho}\frac{\partial\langle p\rangle}{\partial x_i}+\nu\frac{\partial^2\langle u_i\rangle}{\partial x_j^2}-\frac{1}{\rho}\frac{\partial\langle u_i'u_j'\rangle}{\partial x_j}+f_i \qquad \text{(C.1)}$$

where, for example, components of vector f_i may be taken as (f_1, 0, 0) denoting a body force or pressure gradient driving the flow say in the x_1 (streamwise) direction. Component f_1 is adjusted dynamically to keep the bulk velocity at the periodic inlet/outlet constant. Note that this approach may also be applied for LES. Because of the periodic boundary condition, pressure at the inlet is equal to the pressure at the outlet. Thus, it is not possible to impose say a driving streamwise pressure gradient through boundary conditions. Instead, the streamwise pressure gradient may be imposed through the body force component f_1 appearing in the right hand side of the x_1 momentum equation in (3.20) and which is felt by the entire domain. This body force is adjusted dynamically as

$$f_1^n = f_1^{n-1} + \alpha\,(U_{bulk} + U_{bulk}^{n-1} - 2U_{bulk}^n) \tag{C.2}$$

where f_1^n is the force at time step n, U_{bulk} is the target bulk velocity at the inlet/outlet and U_{bulk}^n is the computed bulk velocity at the inlet/outlet at time step n. Relaxation parameter α is taken to be 0.5 in this study. Note that when U_{bulk}^n reaches its target value, f_1 becomes constant. This approach of setting streamwise periodic boundary conditions and letting the streamwise pressure gradient be represented through a body force has been used in the past for channel flows (e.g. Whiting (1999) and Tejada-Martinez and Jansen et al. (2005)) and flows in baffled contactors (Kim et al. 2010a).

Streamwise body force f_1 drives the flow in that direction and thus, in a control volume setting in the mean, counteracts the wall drag shear stresses due to friction. This force is defined as $f_1 = \Delta P/(\rho \Delta L)$ where ΔP is the pressure drop across the entire streamwise (x_1) length of the contactor and ΔL is the entire streamwise length (x_1) of the contactor. Note that this definition has the same dimensional form as $(1/\rho)(\partial p/\partial x_1)$, which is the streamwise pressure gradient divided by density appearing in the streamwise momentum equation. Based on energy balance, it can be shown that for the present flow configuration, energy loss per unit volume, p_{loss} , is equal to pressure drop across the contactor (ΔP). This energy loss is due to friction associated with molecular viscosity and turbulent (eddy) viscosity. Given that $p_{loss} = \Delta P$ and using the definition $f_1 = \Delta P/(\rho \Delta L)$ given earlier leads to

$$p_{loss} = \rho f_1 \Delta L \tag{C.3}$$

This equation is useful as it gives the energy loss across the contactor in the simulations performed in section 6.2.

Appendix D: Copyright Permissions

Part of this dissertation is reprinted from the Author's previous publications listed below. The permissions for reusing these publications are shown in the following pages:

1. Zhang J., Tejada-Martinez, A. E., Zhang, Q., and Lei, H. (2014). Evaluating Hydraulic and Disinfection Efficiencies of a Full-Scale Ozone Contactor using a RANS-based Modeling Framework. Water Research, 52, 155-167.
2. Zhang J., Tejada-Martinez, A. E., and Zhang, Q. (2013). Hydraulic Efficiency in RANS of the Flow in Multi-Chambered Ozone Contactors. Journal of Hydraulic Engineering, 139(11), 1150-1157.
3. Zhang J., Tejada-Martinez, A. E., and Zhang, Q. (2013). RANS Simulation of the Flow and Tracer Transport in a Multi-chambered Ozone Contactor. Journal of Environmental Engineering, 139(3), 450-454.

RightsLink®

Home | Account Info | Help

Title: Reynolds-Averaged Navier-Stokes Simulation of the Flow and Tracer Transport in a Multichambered Ozone Contactor

Author: Zhang, J., Tejada-Martínez, A., and Zhang, Q.

Publication: Journal of Environmental Engineering

Publisher: American Society of Civil Engineers

Date: 03/01/2013

Logged in as:
Jie Zhang

LOGOUT

Permissions Request

As an ASCE author, you are permitted to reuse you own content for another ASCE or non-ASCE publication.

Please add the full credit line "With permission from ASCE" to your source citation. Please print this page for your records.

Type of use: Dissertation/Thesis

Portion: full article

Format: print and electronic

Use of this content will make up more than 25% of the new work: no

Author of this ASCE work or ASCE will publish the new work: yes

BACK | CLOSE WINDOW

RightsLink®

Home | Account Info | Help

Title: Hydraulic Efficiency in RANS of the Flow in Multichambered Contactors

Author: Zhang, J., Tejada-Martínez, A., and Zhang, Q.

Publication: Journal of Hydraulic Engineering

Publisher: American Society of Civil Engineers

Date: 11/01/2013

Logged in as:
Jie Zhang

LOGOUT

Permissions Request

As an ASCE author, you are permitted to reuse you own content for another ASCE or non-ASCE publication.

Please add the full credit line "With permission from ASCE" to your source citation. Please print this page for your records.

Type of use: Dissertation/Thesis

Portion: full article

Format: print and electronic

Use of this content will make up more than 25% of the new work: no

Author of this ASCE work or ASCE will publish the new work: yes

BACK | CLOSE WINDOW

ELSEVIER LICENSE
TERMS AND CONDITIONS

Feb 04, 2014

This is a License Agreement between Jie Zhang ("You") and Elsevier ("Elsevier") provided by Copyright Clearance Center ("CCC"). The license consists of your order details, the terms and conditions provided by Elsevier, and the payment terms and conditions.

All payments must be made in full to CCC. For payment instructions, please see information listed at the bottom of this form.

Supplier	Elsevier Limited The Boulevard,Langford Lane Kidlington,Oxford,OX5 1GB,UK
Registered Company Number	1982084
Customer name	Jie Zhang
Customer address	4202 E. Fowler Ave. Tampa, FL 33620
License number	3321990749317
License date	Feb 04, 2014
Licensed content publisher	Elsevier
Licensed content publication	Water Research
Licensed content title	Evaluating hydraulic and disinfection efficiencies of a full-scale ozone contactor using a RANS-based modeling framework
Licensed content author	Jie Zhang,Andrés E. Tejada-Martínez,Qiong Zhang,Hongxia Lei
Licensed content date	1 April 2014
Licensed content volume number	52
Licensed content issue number	
Number of pages	13
Start Page	155
End Page	167
Type of Use	reuse in a thesis/dissertation
Portion	full article
Format	both print and electronic
Are you the author of this Elsevier article?	Yes
Will you be translating?	No
Title of your	Numerical Simulation of Flow in Ozonation Process

thesis/dissertation	
Expected completion date	Mar 2014
Estimated size (number of pages)	230
Elsevier VAT number	GB 494 6272 12
Permissions price	0.00 USD
VAT/Local Sales Tax	0.00 USD / 0.00 GBP
Total	0.00 USD
Terms and Conditions	

INTRODUCTION

1. The publisher for this copyrighted material is Elsevier. Byclicking "accept" in connection with completing this licensingtransaction, you agree that the following terms and conditions apply to thistransaction (along with the Billing and Payment terms and conditionsestablished by Copyright Clearance Center, Inc. ("CCC"), at the timethat you opened your Rightslink account and that are available at any time at http://myaccount.copyright.com).

GENERAL TERMS

2. Elsevier hereby grants you permission to reproduce the aforementionedmaterial subject to the terms and conditions indicated.

3. Acknowledgement: If any part of the material to be used (for example,figures) has appeared in our publication with credit or acknowledgement toanother source, permission must also be sought from that source. If suchpermission is not obtained then that material may not be included in yourpublication/copies. Suitable acknowledgement to the source must be made, eitheras a footnote or in a reference list at the end of your publication, asfollows:

"Reprinted from Publication title, Vol /edition number, Author(s), Title ofarticle / title of chapter, Pages No., Copyright (Year), with permission fromElsevier [OR APPLICABLE SOCIETY COPYRIGHT OWNER]." Also Lancet special credit -"Reprinted from The Lancet, Vol. number, Author(s), Title of article, PagesNo., Copyright (Year), with permission from Elsevier."

4. Reproduction of this material is confined to the purpose and/or media forwhich permission is hereby given.

5. Altering/Modifying Material: Not Permitted. However figures andillustrations may be altered/adapted minimally to serve your work. Any otherabbreviations, additions, deletions and/or any other alterations shall be madeonly with prior written authorization of Elsevier Ltd. (Please contact Elsevierat permissions@elsevier.com)

6. If the permission fee for the requested use of our material is waived inthis instance, please be advised that your future requests for Elseviermaterials may attract a fee.

7. Reservation of Rights: Publisher reserves all rights not specificallygranted in the combination of (i) the license details provided by you andaccepted in the course of this licensing transaction, (ii) these

terms andconditions and (iii) CCC's Billing and Payment terms and conditions.

8. License Contingent Upon Payment: While you may exercise the rightslicensed immediately upon issuance of the license at the end of the licensingprocess for the transaction, provided that you have disclosed complete andaccurate details of your proposed use, no license is finally effective unlessand until full payment is received from you (either by publisher or by CCC) asprovided in CCC's Billing and Payment terms and conditions. If fullpayment is not received on a timely basis, then any license preliminarilygranted shall be deemed automatically revoked and shall be void as if nevergranted. Further, in the event that you breach any of these terms andconditions or any of CCC's Billing and Payment terms and conditions, thelicense is automatically revoked and shall be void as if never granted. Use of materials as described in a revoked license, as well as any use of thematerials beyond the scope of an unrevoked license, may constitute copyrightinfringement and publisher reserves the right to take any and all action toprotect its copyright in the materials.

9. Warranties: Publisher makes no representations or warranties with respectto the licensed material.

10. Indemnity: You hereby indemnify and agree to hold harmless publisher andCCC, and their respective officers, directors, employees and agents, from andagainst any and all claims arising out of your use of the licensed materialother than as specifically authorized pursuant to this license.

11. No Transfer of License: This license is personal to you and may not besublicensed, assigned, or transferred by you to any other person withoutpublisher's written permission.

12. No Amendment Except in Writing: This license may not be amended exceptin a writing signed by both parties (or, in the case of publisher, by CCC onpublisher's behalf).

13. Objection to Contrary Terms: Publisher hereby objects to any termscontained in any purchase order, acknowledgment, check endorsement or otherwriting prepared by you, which terms are inconsistent with these terms andconditions or CCC's Billing and Payment terms and conditions. These termsand conditions, together with CCC's Billing and Payment terms and conditions(which are incorporated herein), comprise the entire agreement between you andpublisher (and CCC) concerning this licensing transaction. In the eventof any conflict between your obligations established by these terms andconditions and those established by CCC's Billing and Payment terms andconditions, these terms and conditions shall control.

14. Revocation: Elsevier or Copyright Clearance Center may deny thepermissions described in this License at their sole discretion, for any reasonor no reason, with a full refund payable to you. Notice of such denialwill be made using the contact information provided by you. Failure toreceive such notice will not alter or invalidate the denial. In no eventwill Elsevier or Copyright Clearance Center be responsible or liable for anycosts, expenses or damage incurred by you as a result of a denial of yourpermission request, other than a refund of the amount(s) paid by you toElsevier and/or Copyright Clearance Center for denied permissions.

LIMITED LICENSE

The following terms and conditions apply only to specific license types:

15. **Translation**: This permission is granted fornon-exclusive world **English** rights only unless yourlicense was granted for translation rights. If you licensed translation rightsyou may only translate this content into the languages you requested. Aprofessional translator must perform all translations and reproduce the contentword for word preserving the integrity of the article. If this license is tore-use 1 or 2 figures then permission is granted for non-exclusive world rightsin all languages.

16. **Posting licensed content on any Website**: The followingterms and conditions apply as follows: Licensing material from an Elsevierjournal: All content posted to the web site must maintain the copyright informationline on the bottom of each image; A hyper-text must be included to the Homepageof the journal from which you are licensing at http://www.sciencedirect.com/science/journal/xxxxx orthe Elsevier homepage for books at http://www.elsevier.com; CentralStorage: This license does not include permission for a scanned version of thematerial to be stored in a central repository such as that provided byHeron/XanEdu.

Licensing material from an Elsevier book: A hyper-text link must be includedto the Elsevier homepage at http://www.elsevier.com . Allcontent posted to the web site must maintain the copyright information line onthe bottom of each image.

Posting licensed content on Electronic reserve: In addition to the above the following clausesare applicable: The web site must be password-protected and made available onlyto bona fide students registered on a relevant course. This permission isgranted for 1 year only. You may obtain a new license for future websiteposting.

For journal authors: the following clauses are applicable inaddition to the above: Permission granted is limited to the author acceptedmanuscript version* of your paper.

***Accepted Author Manuscript (AAM) Definition:** An accepted authormanuscript (AAM) is the author's version of the manuscript of an article thathas been accepted for publication and which may include any author-incorporatedchanges suggested through the processes of submission processing, peer review,and editor-author communications. AAMs do not include other publishervalue-added contributions such as copy-editing, formatting, technicalenhancements and (if relevant) pagination.

You are not allowed to download and post the published journal article (whetherPDF or HTML, proof or final version), nor may you scan the printed edition tocreate an electronic version. A hyper-text must be included to the Homepage ofthe journal from which you are licensing at http://www.sciencedirect.com/science/journal/xxxxx. As part of our normal production process, you will receive an e-mail noticewhen your article appears on Elsevier's online service ScienceDirect(www.sciencedirect.com). That e-mail will include the article's Digital ObjectIdentifier (DOI). This number provides the electronic link to the publishedarticle and should be included in the posting of your personal version. We askthat you wait until you receive this e-mail and have the DOI to do any posting.

Posting to a repository: Authorsmay post their AAM immediately to their employer's institutional repository forinternal use only and may make their manuscript publically available after thejournal-specific embargo period has ended.

Please also refer to Elsevier'sArticle Posting Policy for further information.

18. **For book authors** the following clauses are applicable in addition tothe above: Authors are permitted to place a briefsummary of their work online only.. You are notallowed to download and post the published electronic version of your chapter,nor may you scan the printed edition to create an electronic version. Posting to a repository: Authors arepermitted to post a summary of their chapter only in their institution'srepository.

20. **Thesis/Dissertation**: If your license is for use in athesis/dissertation your thesis may be submitted to your institution in eitherprint or electronic form. Should your thesis be published commercially, pleasereapply for permission. These requirements include permission for the Libraryand Archives of Canada to supply single copies, on demand, of the completethesis and include permission for UMI to supply single copies, on demand, ofthe complete thesis. Should your thesis be published commercially, pleasereapply for permission.

Elsevier Open Access Terms andConditions

Elsevier publishes Open Access articles in both its Open Access journals andvia its Open Access articles option in subscription journals.

Authors publishing in an Open Access journal or who choose to make theirarticle Open Access in an Elsevier subscription journal select one of thefollowing Creative Commons user licenses, which define how a reader may reusetheir work: Creative Commons Attribution License (CC BY), Creative CommonsAttribution – Non Commercial - ShareAlike (CC BY NCSA) and Creative Commons Attribution – Non Commercial – No Derivatives (CC BYNC ND)

Terms & Conditions applicable toall Elsevier Open Access articles:

Any reuse of the article must not represent the author as endorsing theadaptation of the article nor should the article be modified in such a way asto damage the author's honour or reputation.

The author(s) must be appropriately credited.

If any part of the material to be used (for example, figures) has appearedin our publication with credit or acknowledgement to another source it is theresponsibility of the user to ensure their reuse complies with the terms andconditions determined by the rights holder.

Additional Terms & Conditionsapplicable to each Creative Commons user license:

CC BY: You may distribute andcopy the article, create extracts, abstracts, and other revised versions,adaptations or derivative works of or from an article (such as a translation),to include in a collective work (such as an anthology), to text or data minethe article, including for commercial purposes without permission from Elsevier

CC BY NC SA: For non-commercialpurposes you may distribute and copy the article, create extracts, abstractsand other revised versions, adaptations or derivative works of or from anarticle

(such as a translation), to include in a collective work (such as ananthology), to text and data mine the article and license new adaptations or creationsunder identical terms without permission from Elsevier

CC BY NC ND: For non-commercialpurposes you may distribute and copy the article and include it in a collectivework (such as an anthology), provided you do not alter or modify the article,without permission from Elsevier

Any commercial reuse of Open Access articles published with a CC BY NC SA or CC BY NC NDlicense requires permission from Elsevier and will be subject to a fee.

Commercial reuse includes:

- Promotional purposes (advertising or marketing)
- Commercial exploitation (e.g. a product forsale or loan)
- Systematic distribution (for a fee or free ofcharge)

Please refer to Elsevier'sOpen Access Policy for further information.

21. **Other Conditions**:

v1.7

If you would like to pay for this license now, please remit this license along with your payment made payable to "COPYRIGHT CLEARANCE CENTER" otherwise you will be invoiced within 48 hours of the license date. Payment should be in the form of a check or money order referencing your account number and this invoice number RLNK501217940. Once you receive your invoice for this order, you may pay your invoice by credit card. Please follow instructions provided at that time.

Make Payment To:
Copyright Clearance Center
Dept 001
P.O. Box 843006
Boston, MA 02284-3006

For suggestions or comments regarding this order, contact RightsLink Customer Support: customercare@copyright.com or +1-877-622-5543 (toll free in the US) or +1-978-646-2777.

Gratis licenses (referencing $0 in the Total field) are free. Please retain this printable license for your reference. No payment is required.